UNIVERSIDADE FEDERAL DE UBERLÂNDIA

INSTITUTO DE QUÍMICA

Programa de Pós-Graduação em Química

RAQUEL GOMES DA ROCHA

3D-printed electrochemical sensors: From the influence of printing parameters to the improvement of conductive filaments

Uberlândia – MG

2024

UNIVERSIDADE FEDERAL DE UBERLÂNDIA

INSTITUTO DE QUÍMICA

Programa de Pós-Graduação em Química - Doutorado

3D-printed electrochemical sensors: From the influence of printing parameters to the improvement of conductive filaments

Tese de doutorado apresentada ao Programa de Pós-Graduação do Instituto de Química da Universidade Federal de Uberlândia, como requisito para obtenção do título de Doutora em Química.

Aluna: Me Raquel Gomes da Rocha

Orientador: Prof. Dr. Eduardo Mathias Richter

Coorientador: Prof. Dr. Rodrigo Alejandro Abarza Muñoz

Área de concentração: Química Analítica

Junho, 2024

Ficha Catalográfica Online do Sistema de Bibliotecas da UFU
com dados informados pelo(a) próprio(a) autor(a).

R672 Rocha, Raquel Gomes da, 1993-
2024 3D-printed electrochemical sensors: From the influence of printing parameters to the improvement of conductive filaments [recurso eletrônico] / Raquel Gomes da Rocha. - 2024.

Orientador: Eduardo Mathias Richter.
Coorientador: Rodrigo Alejandro Abarza Muñoz.
Tese (Doutorado) - Universidade Federal de Uberlândia, Pós-graduação em Química.
Modo de acesso: Internet.
Disponível em: http://doi.org/10.14393/ufu.te.2024.407
Inclui bibliografia.

1. Química. I. Richter, Eduardo Mathias,1965-, (Orient.). II. Muñoz, Rodrigo Alejandro Abarza,1980-, (Coorient.). III. Universidade Federal de Uberlândia. Pós-graduação em Química. IV. Título.

CDU: 54

Bibliotecários responsáveis pela estrutura de acordo com o AACR2:

Gizele Cristine Nunes do Couto - CRB6/2091
Nelson Marcos Ferreira - CRB6/3074

UNIVERSIDADE FEDERAL DE UBERLÂNDIA
Coordenação do Programa de Pós-Graduação em Química
Av. João Naves de Ávila, 2121, Bloco 5I - Bairro Santa Mônica, Uberlândia-MG, CEP 38400-902
Telefone: (34) 3239-4385 - www.cpgquimica.iq.ufu.br - cpgquimica@ufu.br

ATA

Programa de Pós-Graduação em:	Química				
Defesa de:	Tese de Doutorado Acadêmico, 159, PPGQUI				
Data:	Vinte e um de junho de dois mil e vinte e quatro	Hora de início:	14:00h	Hora de encerramento:	18:42h
Matrícula do Discente:	11913QMI012				
Nome do Discente:	Raquel Gomes Rocha				
Título do Trabalho:	“3D-PRINTED ELECTROCHEMICAL SENSORS: FROM THE INFLUENCE OF PRINTING PARAMETERS TO THE IMPROVEMENT OF CONDUCTIVE FILAMENTS”				
Área de concentração:	Química				
Linha de pesquisa:	Eletroquímica Aplicada				
Projeto de Pesquisa de vinculação:	“Desenvolvimento de filamentos condutores a base de grafeno para produção de sensores empregando a tecnologia de impressão 3D”				
ODS 9	Indústria, inovação e infraestrutura: construir infraestrutura resiliente, promover a industrialização inclusiva e sustentável, e fomentar a inovação.				

Reuniu-se, no auditório da Pós-graduação, bloco 5I, a Banca Examinadora, designada pelo Colegiado do Programa de Pós-graduação em Química, assim composta: Professores Doutores: **André Luiz dos Santos** e **Sidnei Gonçalves da Silva,** da Universidade Federal de Uberlândia; **Orlando Fatibello Filho,** da Universidade Federal de São Carlos; **Clésia Cristina Nascentes**, da Universidade Federal de Minas Gerais; e **Eduardo Mathias Richter**, orientador(a) do(a) candidato(a).

Iniciando os trabalhos o presidente da mesa, **Dr. Eduardo Mathias Richter**, apresentou a Comissão Examinadora e o(a) candidato(a), agradeceu a presença do público, e concedeu ao(à) Discente a palavra para a exposição do seu trabalho. A duração da apresentação do(a) Discente e o tempo de arguição e resposta foram conforme as normas do Programa.

A seguir o senhor(a) presidente concedeu a palavra, pela ordem sucessivamente, aos(às) examinadores(as), que passaram a arguir o(a) candidato(a). Ultimada a arguição, que se desenvolveu dentro dos termos regimentais, a Banca, em sessão secreta, atribuiu o resultado final, considerando o(a) candidato(a):

Aprovada.

Esta defesa faz parte dos requisitos necessários à obtenção do título de Doutor.

O competente diploma será expedido após cumprimento dos demais requisitos, conforme as normas do Programa, a legislação pertinente e a regulamentação interna da UFU.

Documento assinado eletronicamente por **Eduardo Mathias Richter**, **Professor(a) do Magistério Superior**, em 27/06/2024, às 14:44, conforme horário oficial de Brasília, com fundamento no art. 6º, § 1º, do Decreto nº 8.539, de 8 de outubro de 2015.

Documento assinado eletronicamente por **Andre Luiz dos Santos**, **Professor(a) do Magistério Superior**, em 27/06/2024, às 14:47, conforme horário oficial de Brasília, com fundamento no art. 6º, § 1º, do Decreto nº 8.539, de 8 de outubro de 2015.

Documento assinado eletronicamente por **Orlando Fatibello Filho**, **Usuário Externo**, em 27/06/2024, às 14:54, conforme horário oficial de Brasília, com fundamento no art. 6º, § 1º, do Decreto nº 8.539, de 8 de outubro de 2015.

Documento assinado eletronicamente por **Sidnei Gonçalves da Silva**, **Professor(a) do Magistério Superior**, em 27/06/2024, às 15:04, conforme horário oficial de Brasília, com fundamento no art. 6º, § 1º, do Decreto nº 8.539, de 8 de outubro de 2015.

Documento assinado eletronicamente por **Clesia Cristina Nascentes**, **Usuário Externo**, em 27/06/2024, às 17:58, conforme horário oficial de Brasília, com fundamento no art. 6º, § 1º, do Decreto nº 8.539, de 8 de outubro de 2015.

A autenticidade deste documento pode ser conferida no site https://www.sei.ufu.br/sei/controlador_externo.php?acao=documento_conferir&id_orgao_acesso_externo=0, informando o código verificador **5497051** e o código CRC **36AFE336**.

Referência: Processo nº 23117.025034/2024-81 SEI nº 5497051

Agradecimentos

Começo meus agradecimentos com lágrimas nos olhos só de lembrar o que foi essa jornada do doutorado. Vivi a ansiedade da pandemia, o medo do amanhã, afinal, não sabíamos como seria uma doença nova, e após tudo isso, tive a luta diária de viver uma doença desconhecida. Todas as minhas versões conhecidas, deixaram de existir e passei a viver um dia por vez. E que dias intensos, vivi minhas maiores dores e medo, mas não deixei de tentar, respirar e agradecer pela vida e a oportunidade de ter tido um bom acompanhamento médico.

Mas nada disso seria possível se eu não tivesse encontrado pessoas que me fizeram mais fortes (e são tantas pessoas) e me levantaram quando a tristeza resolvia aparecer. Além disso, Deus me deu toda sabedoria para que pudesse enfrentar os desafios que a vida me colocava, em meio a sala de cirurgia, UTI e muitas internações, existia o sorriso no rosto, sabedoria e força para lutar. Gostaria de agradecer aos meus pais, Agilson e Vina, que além de serem meus maiores exemplos de perseverança e determinação, estiveram ao meu lado e não mediram esforços para que eu pudesse realizar meus sonhos. Um agradecimento especial a minha mãe que chorou a minha dor e enfrentou vários dias do hospital comigo. Nós vencemos, minha mamãe e eu devo muito a você, meu exemplo, minha paixão. Não poderia também de deixar um agradecimento cheio de amor ao meu velho, meu parceiro de compras, meu teimoso, meu pai...ele me ensina todos os dias, que desistir não é uma opção e com garra, nós conseguimos chegar em qualquer lugar.

No meio do meu doutorado, Deus me presenteou com meu marido Yuri e vivemos dias intensos, desde as noites mal dormidas pelo cansaço do doutorado até pelos dias que enfrentamos no hospital. Foi o ano mais intenso das nossas vidas, e você parou o tempo e esteve ao meu lado, cuidando e se esforçando para ser o meu suporte naquele momento. Amor, só nós sabemos a luta que vivemos e que bom que você esteve do meu lado e vencemos. Agradecer também a família do meu marido que também estiveram mandando boas energias.

E no meio de tudo isso, veio meu sobrinho Joaquim, tão pequeno, mas com tanta força e tanta luz... seu sorriso, seu carinho me fizeram não desistir e a vontade de viver mais momentos com vocês, me deu tanta força para continuar. Ainda bem que você veio, meu pequeno para ser luz e alegria no meio da tempestade.

Gostaria de agradecer também ao meu pet, meu filho, nenê da mamãe, meu cachorro, meu Chico... ele foi tão importante para mim, sempre amou essa mamãe dele e

sentia tanta saudade quando eu ficava dias e mais dias no hospital. Seu amor incondicional, sua lealdade, seu carinho foram calor pro meu coração e todo mundo sabe o tanto que a mamãe não seria nada sem esse cachorro dentuço. Agradecer também a minha amiga Vilma que além de me presentear com meu filho pet, me apoia incondicionalmente e tem estado do meu lado, principalmente nessa etapa final da tese.

E a vida de pós graduação me trouxe tantas pessoas, e me deu de presente meus melhores amigos, Thiago e Jéssica, eu sempre repito para todos: *"todos deveriam ter uma Jéssica e um Thiago na vida"*. Eles foram amigos fiéis que não me deixaram cair, me deram o suporte para continuar e não desistir da pós-graduação e sempre, em todos os momentos, estiveram do meu lado. Thiago, sempre com o humor para arrancar sorrisos e todo seu cuidado e a Jéssica, com toda sua calma, cuidado e carinho. Não sei nem como agradecer, essa escrita da tese saiu com todo apoio e cuidado de vocês. Valeu cada momento, desde os nossos cafés, nossas viagens e todos os dias de laboratório.

Não poderia também deixar de agradecer aos Professores Eduardo e Rodrigo. Eles me ensinaram que ninguém cresce sozinho, que ciência se faz com parceria. Além disso, pensa em orientadores que foram cuidadosos e tiveram sempre empatia com todos os problemas que vivi, muito obrigada por tudo! Eles cuidam da Família Nupe, sim, somos mais que um grupo de pesquisa, somos uma família científica e uma vez Nupiano sempre Nupiano. E não poderia deixar de agradecer a todos os Nupianos que eu conheci. Gostaria de agradecer a velha guarda Nupiana (Brenda, Diego, Michelle, Weberson, Jhonys, Luiz André, Melo, David, André, Mariana, Alice, Silvia, Sarah, Afonso, Jian) que sempre tiveram muitos cafés, muito sorrisos e muita ciência para partilhar... e aos novos Nupianos que me acolheram (Mayane, Gil casca de bala, JP, Maria, Ana, Marina, Amanda, Lucas, Tiago, Anastacio, Nélio, Isa) e me deram todo suporte. Obrigada minha família Nupiana.

Agradecer aos meus familiares, tio(a)s, primo(a)s que sempre mandaram boas energias, oraram e sempre estiveram do meu lado. Vocês são incríveis. Agradecer ao meu tio Antônio *"in memorian",* que sempre será meu exemplo de honestidade, bondade e cuidado. Gostaria de agradecer também aos meus amigos do Mercado Fantástico. Com eles, conheci tanta história bonita, tantas pessoas boas e tanta gente que rezou e esteve por mim, especialmente a turma do RH e meus compradores. Vocês sempre estarão em meu coração. Agradeço também pela equipe médica, principalmente a Dri, Cris e a Marina pelo cuidado tanto comigo quanto com meus familiares.

Agradecer a tantos outros amigos que estiveram sempre presentes, me mandando mensagens positivas. Sempre serei grata por todo apoio.

Também gostaria de deixar meu agradecimento ao Prof. Bonacin e aos seus alunos Priscila e Rafael que me auxiliaram e contribuíram em todos os trabalhos da tese. Aos Professores e todos os funcionários do IQ-UFU que contribuíram para minha formação, desde a graduação e até o final do doutorado. Aos órgãos de fomento, CNPq, Capes e Fapemig pelo financiamento de pesquisa.

Aos membros da banca de qualificação e defesa pela colaboração com o trabalho.

Como sempre digo e repito:

"Ainda bem que existem os meus e que bom que tenho eles. Eu sou cheia de amor!"

RESUMO

A impressão tridimensional (3D) é uma técnica de fabricação por manufatura aditiva que possibilita a obtenção de uma grande variedade de estruturas com geometrias variadas e com grande versatilidade. A possibilidade de se obter objetos complexos com relativo baixo custo utilizando uma ampla gama de materiais proporcionou grande atratividade da impressão 3D em áreas como a eletroanálise. Esta tecnologia vem possibilitando a obtenção de aparatos analíticos completos, tais como células e dispositivos eletroquímicos, além de sensores a partir do uso de filamentos não-condutivos e condutivos (compósitos). Neste contexto, o objetivo neste trabalho foi explorar filamentos condutivos comerciais à base de grafeno e ácido polilático (G/PLA) como material base para a obtenção de sensores para a detecção de glicose e H_2O_2. A detecção de glicose foi realizada a partir da incorporação do $Ni(OH)_2$ no filamento para impressão, atribuindo propriedades eletrocatalíticas ao sensor obtido. O novo material obtido foi caracterizado por técnicas de microscopia e espectroscopia, além de técnicas eletroquímicas. Posteriormente, o sensor produzido a partir deste filamento foi empregado na detecção não enzimática de glicose, apresentando um limite de detecção de 2,4 μmol L^{-1}, proporcionando a rápida (160 injeções h^{-1}), precisa (RSD < 5%) e seletiva detecção do analito na presença de potenciais interferentes como ácido ascórbico, ureia e ácido úrico. Para a detecção de H_2O_2, a exposição das impurezas de ferro presentes no filamento (G/PLA) foi realizada a partir de um tratamento químico com dimetilformamida por 30 minutos. Os íons Fe^{3+} da superfície foram então explorados para a eletrodeposição de azul da Prússia empregando a técnica de voltametria cíclica (200 ciclos) na presença de $K_3[Fe(CN)_6]$, KCl e HCl. O eletrodo modificado foi então empregado na detecção amperométrica de H_2O_2 utilizando-se um sistema de análise por injeção em batelada (BIA). Um limite de detecção de 0,56 μmol L^{-1} foi obtido, além de valores de recuperação adequados (94 a 101%) para H_2O_2 em amostras reais de leite. Por fim, considerando a importância dos parâmetros de impressão no desempenho final de sensores obtidos por impressão 3D, alguns parâmetros como a orientação da impressão, espessura de camada, número de perímetros e velocidade de impressão foram avaliados em sensores obtidos a partir de filamentos contendo *carbon black* e ácido polilático (CB/PLA). Para avaliar o efeito destes parâmetros, caracterizações por técnicas eletroquímicas (voltametria cíclica e impedância eletroquímica) foram realizadas usando uma solução de $[Ru(NH_3)_6]^{2+/3+}$ 10 mmol L^{-1} como sonda redox. Os resultados mostraram que eletrodos impressos na orientação vertical, com menor espessura de camada (0,05 mm) e velocidade de impressão de perímetro (30 mm s^{-1}) usando dois perímetros forneceram o melhor desempenho eletroquímico. Além disso, observou-se que a partir dos parâmetros selecionados há uma maior disponibilidade e distribuição de sítios condutores, mostrando que os parâmetros de impressão são recursos importantes para permitir a fabricação de plataformas eletroquímicas melhoradas via impressão 3D.

Palavras-chave: glicose; peróxido de hidrogênio; sensores eletroquímicos impressos em 3D; hidróxido de níquel; azul da Prússia; parâmetros de impressão.

ABSTRACT

Three-dimensional (3D) printing is an additive manufacturing technique, which makes it possible to obtain a great variety of structures with varied geometries and great versatility. The possibility of obtaining complex objects at a relatively low cost using a wide range of materials provided great attractiveness to 3D printing in areas such as electroanalysis. This technology makes it possible to obtain complete analytical apparatus, such as electrochemical cells and devices, as well as sensors from the use of non-conductive and conductive (composites) filaments. In this context, the objective in this work was to explore commercial conductive filaments based on graphene and polylactic acid (G/PLA) as a base material for obtaining improved sensors for the detection of glucose and H_2O_2. Glucose detection was performed by incorporating $Ni(OH)_2$ into the printing filament, attributing electrocatalytic properties to the obtained sensor. The new material was characterized by microscopic and spectroscopic techniques, in addition to electrochemical techniques. Subsequently, the sensor produced from this filament was used for the non-enzymatic glucose detection, showing a detection limit of 2.4 μmol L^{-1}, providing fast (160 injections h^{-1}), precise (RSD < 5%) and selective detection of the analyte in the presence of potential interferents such as ascorbic acid, urea and uric acid. For the detection of H_2O_2, the exposure of iron impurities present in the filament (G/PLA) was performed with a chemical treatment with dimethylformamide for 30 minutes. The Fe^{3+} ions on the electrode surface were then exploited for the electrodeposition of Prussian blue, which was performed using the cyclic voltammetry technique (200 cycles) in the presence of $K_3[Fe(CN)_6]$, KCl and HCl. The modified electrode was then used in the amperometric detection of H_2O_2 using a batch injection analysis (BIA) system. A detection limit of 0.56 μmol L^{-1} was obtained, in addition to adequate recovery values (94 to 101%) for H_2O_2 in milk samples. Finally, considering the importance of printing parameters in the final performance of sensors obtained by 3D printing, some parameters such as printing orientation, layer thickness, perimeter number and printing speed were evaluated in sensors obtained from filaments containing carbon black and polylactic acid (CB/PLA). To evaluate the effects of these parameters, characterizations by electrochemical techniques were performed using a solution of 10 mmol L^{-1} $[Ru(NH_3)_6]^{2+/3+}$ as redox probe. Results showed that the electrodes printed in vertical orientation, with lower layer thickness (0.05 mm) and print speed (30 mm s^{-1}) using two perimeter numbers provided the best electrochemical performance. In addition, it was observed that from the selected parameters, there was a greater availability and distribution of conducting sites, showing that the printing parameters are important resources to allow the fabrication of improved electrochemical platforms.

Keywords: glucose; hydrogen peroxide; 3D printed electrochemical sensors; nickel hydroxide; Prussian blue; printing parameters.

List of Figures

List of Tables

ABBREVIATIONS AND SYMBOLS

.stl: file format native to the stereolithography CAD software created by 3D Systems.

3D: Three-dimensional

ABS: Acrylonitrile Butadiene Styrene

AM: Aditive Manufacturing

ASTM: American Society for Additive Manufacturing for Testing and Materials

BG: Berlim Green

BIA: Batch Injection Analysis

BIA-AMP: Batch injection analysis with amperometric detection

BJT: Material Binder Jetting

C/ABS: Carbon-loaded ABS electrodes

CAD: Computer-Aided Design

CB: Carbon Black

CB/Gpt/rPLA: Carbon black, graphite and recycled PLA electrodes

CB/rPLA: Carbon black recycled PLA electrodes

CDLP: Continuous Digital Light Processing

CLIP: Continuous Liquid Interface Production

CNT: Carbon Nanotube

CNT/PLA: Carbon nanotube and PLA electrodes

CV: Cyclic Voltammetry

DED: Directed Energy Deposition

DIW: Direct Ink Laser-Assisted Writing

DLP: Digital Light Processing

DMF: Dimethylformamide

DMLM: Direct Metal Laser Melting

DMLS: Direct Metal Laser Sintering

DPV: Differential pulse voltammetry

DPASV: Differential pulse anodic stripping voltammetry

EBM: Electron Beam Melting

EDX: Energy-Dispersive X-Ray Spectroscopy

EIS: Electrochemical Impedance Spectroscopy

FDM: Fused Deposition Modeling

G: Graphene

G-PLA: graphene and PLA composite

Gpt/PLA: graphite and PLA

Ipa: Anodic faradaic current

Ipc: cathodic faradaic current

ISO: International Organization for Standardization

LED: Light Emitting Diodes

LOD: Limit of Detection

LOQ: Limit of Quantification

MCR-ALS: Multivariate Curve Resolution with Alternating Least Squares

MEX: Material Extrusion

MJT: Material Jetting

Ni-G-PLA: nickel, graphene and PLA composite

PB: Prussian Blue

PBF: Powder Bed Fusion

PDMS: Polydimethylsiloxane

PET: Polyethylene Terephthalate

PLA: Polylactic Acid

PVA: Polyvinyl Acetate

PW: Prussian White

RSD: Relative Standard Deviation

SEM: Scanning Electron Microscopy

SHL: Sheet Lamination

SLA: Stereolithography

SLM: Selective Laser Melting

SLS: Selective Laser Sintering

SPE: Screen Printed Electrodes

STL: Stereolithography

SWV: Square wave voltammetry

SWASV: Square wave anodic stripping voltammetry

TGA: Thermogravimetric Analysis

UV: Ultraviolet

VPP: Vat Photopolymerization

XRF: X-ray Fluorescence analysis

***ΔE*p:** Peak Potential Separation

Table of Contents

1 GENERAL INTRODUCTION

In recent years, research groups have investigated the fabrication of analytical sensors for real-time analysis of the quality of environmental, food, forensic, and pharmaceutical samples. Electrochemical methods have several key properties that are important for on-site measurements, including minimal sample manipulation, high sensitivity, low cost, and easy miniaturization. These techniques are based on measurements of changes in electrical properties (potential, current, conductivity, charge transfer, etc.) at electrode/solution interfaces or between electrodes [1]. The detection of changes in these electrical properties have been widely used for the determination of the concentration of an increasing number of target species. Although the variety of electrochemical sensing systems has increased, for example, the successful commercialization of blood glucose sensors, there are still some challenges in producing portable electrochemical sensing systems [2]. Conventional electrochemical sensing systems comprise electrochemical cells, electrodes, and bulky electrochemical workstations that require specialized personnel. In addition, conventional working electrodes (glassy carbon, boron doped diamond, gold, platinum, etc.) are expensive and not suitable for on-site analysis because they usually require greater volume of samples/supporting electrolyte and moderately complex electrochemical cell setups. In recent years, many small size, reliability, and simple cost-effective electrochemical sensing systems suitable for on-site applications ("portable") have been developed by many research groups [3].

Screen-printed electrodes (SPEs) are an interesting alternative to produce portable electrochemical sensors or platforms to overcome the limitations of conventional electrochemical analysis systems. Generally, SPEs are manufactured using well-known industrial printers by depositing conductive inks on a flat solid substrate (ceramic, polymers, paper, etc) [4]. Although SPEs are a promising material to replace conventional electrodes, they still have low inter- electrode reproducibility (RSD $\geq$ 5%), requires high-cost industrial printers (not available in most laboratories) and, in some cases, poor electrochemical performance for some analytes, especially in strongly basic or acidic solutions and when organic solvents need to be used. In this sense, additive manufacturing, especially 3D-printing technology, is an interesting alternative to produce electrochemical sensing systems. This technology has been widely used to produce mass-

scale custom-made and cost-effective devices in many areas, including electrochemistry. [5,6]. In this field, 3D printers are employed to produce batteries [7,8], electrochemical cells [9], microfluidic devices [10,11], sensors [12,13] and capacitors [14,15]. In fact, in brief research bibliometric on the Web of Science database, using the keywords 3D-print* and sensors, showed a marked increase in research in this field in the last few years, as shown in **Figure 1**. The increase in published papers on the development of sensors using 3D printing is notable. This trend is driven by the versatility of the 3D printing technology, which enables easy construction, modification or repair various objects. This technology has captivated the imaginations of do-it-yourself (DIY) hackers, engineers, and scientists [16]. The DIY ethos promotes independence, creativity, and self-reliance in addressing tasks traditionally handled by professionals, and advancements in 3D printing have significantly empowered this approach. Furthermore, the widespread adoption of 3D printers has democratized the possibility of production in homes, workshops, and small businesses.

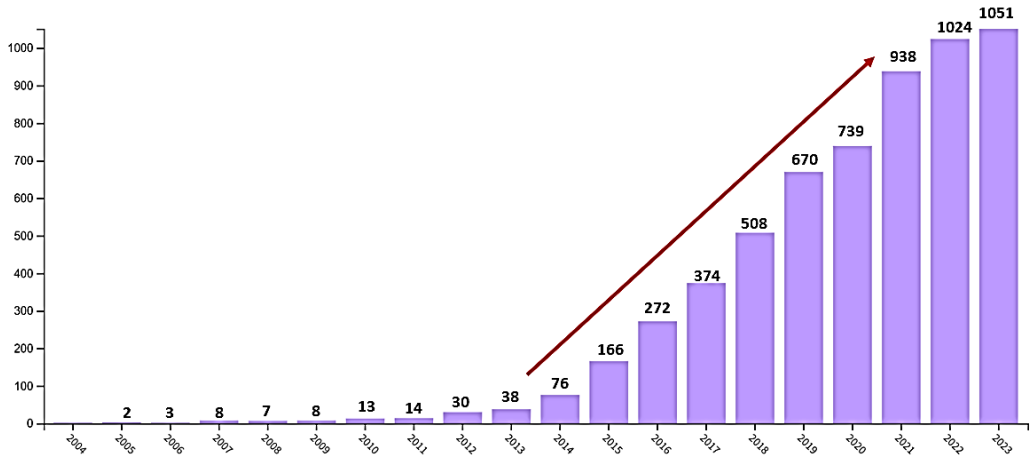

Figure 1. Number of publications on sensor development using 3D printing technology according to the Web of Science® database (keywords: 3D-print* and sensors).

Moreover, according to this research, 40% of the articles are related to areas of analytical and electrochemistry, which demonstrates the growth of interest in 3D printing technology in these areas. As can be seen in a recent review, some groups have been used the 3D printing technology to construct electrochemical devices and/or sensors to detect different analytes [17].

1.1 Additive Manufacturing

Additive Manufacturing (AM) consists in the process of rapid prototyping in which materials are used to build three-dimensional (3D) objects, in an opposite process to that observed in subtractive manufacturing [18,19]. Through the AM process, it is possible to construct objects with elaborate and complex geometries that are very difficult to obtain using traditional methods [20]. Among the existing AM processes (Selective Laser Sintering – SLS, Stereolithography – SLA, Selective Laser Melting – SLM, Fused Deposition Modeling - FDM, Binder Jetting, and Material Extrusion, among others), the best-known and low-cost AM method is FDM 3D printing, which has been widely explored in many areas, such as aerospace, food, medical, and electronics [21]. This technique enables the prototyping or production of desired objects from digital files, which makes it possible to produce a wide variety of structures with different geometries. Moreover, the 3D printing technology presents other benefits, including: *(i)* low-cost fabrication with a good print quality; *(ii)* fast prototyping that enables in-situ production; *(iii)* design freedom in which complex geometries can be produced; *(iv)* wide selection of printable materials; and *(v)* lower waste production compared with classical subtractive manufacturing methods [22,23].

The overall workflow for 3D printing, from conceptualization to the final printed object, is the same, even for different 3D printers. **Figure 2** presents a simplified procedure of 3D printing steps of a workflow.

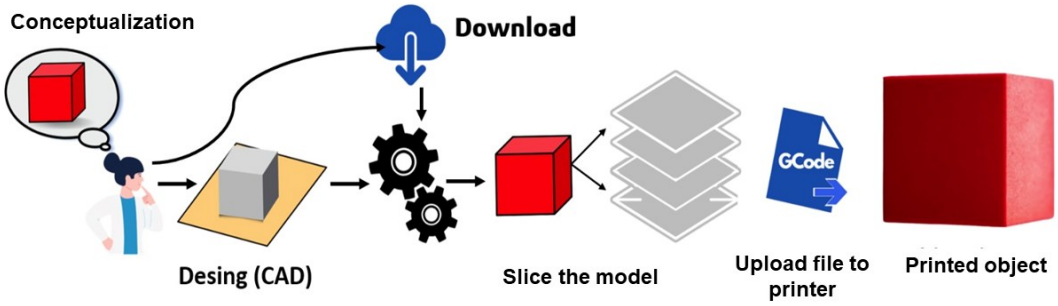

Figure 2. Steps of a 3D printing workflow to construct 3D-printed objects. Adapted from Tully and Meloni [24].

Initially, the object to be produced is conceptualized by three-dimensional (3D) models using digital information. In general, this data is produced in a computer-aided design (CAD) vector format [25]. After generating the three-dimensional model, the data

are converted to an appropriate format for the printer, usually with the *.stl* file format. This file presents the dimensions and the design of the desired object [26]. The most used softwares for this function described in the literature are *FreeCAD*, *SketchUp Suite*, *Onshape* and *Blender* [26,27]. Moreover, there are 3D model repositories such as Thingiverse® and others that contain a variety of 3D object models in *.stl* format.

After the object is created by CAD, it is sent to a slicer software, which is responsible for separating the *.stl* file into layers, converting a three-dimensional image into several two-dimensional images that, when placed on top of each other, form the final three-dimensional object [28]. In this step, the software separates the file into several layers and shows how the printing and deposition routes will be per layer (x-y-z direction of the 3D printer), estimates the amount of material needed to customize the object, and defines the printing parameters. Thus, this information is grouped into a file with the G-code extension to communicate with the 3D printer [29]. Finally, the file is sent to the printer that starts the manufacture of the object. The printing time can vary between minutes, hours, or even days, depending on the complexity and size of the printing object [27].

The strategies proposed for additive manufacturing had no practical applications in the industrial context, until 1981. After this year, Hideo Kodama proposed a rapid prototyping technique using a single laser beam and a photosensitive resin [30,31]. In 1984, Charles Hull invented and patented the stereolithography (STL) process in which liquid photopolymer resins are cured and solidified using a ultraviolet (UV) light in a layer by layer fashion [32]. In 1986, Hull founded the 3D System company, responsible for producing and selling printing machines. After Charles Hull's invention, several methods for 3D printing were invented and applied as patents. In the mid-1980s, Carl Deckard [33] developed the concept of the selective laser sintering (SLS) process (high-powered laser is used to sinter different powdered material, such as plastic, metal, or ceramic), and founded the Desktop Manufacturing Corporation, which was subsequently acquired by the 3D System company. In 1989, Scott and Lisa Crump [34] founded the company Stratasys and were responsible for the invention of fused deposition modeling (FDM), in which thermoplastic filaments are heated in a nozzle and extruded (deposited) on a printing table.

The high manufacturing cost (the cost of a 3D-printer was around one million dollars in the past) and the patents involved in printing methods made it difficult to

implement this methodology in several sectors in the 90s. However, with the expiration of the original FDM 3D printing patent in 2005, new open-source printers were developed (*RepRap Movement* and *Fab@home*) and a drastic cost reduction of 3D printers started. In addition, projects sharing for printer development has also started, making this technology more accessible to users [31,35].

As described in the literature [12], there are several processes for printed objects that use the layer by layer process and therefore depend on the material and machine technology used. In this sense, the International Organization for Standardization and the American Society for Additive Manufacturing for Testing and Materials (ISO/ASTM 52900:2021) developed a glossary with terms and standards that establish 3D printing techniques in seven categories: Vat photopolymerization (VPP), material jetting (MJT), material extrusion (MEX), material binder jetting (BJT), powder bed fusion (PBF), directed energy deposition (DED), and sheet lamination (SHL) [6,36].

1.2 3D-Printing Techniques

As highlighted, 3D printing technologies are classified into seven groups that differ in terms of the application process, part curing, and/or starting material. In the VPP technique, a photopolymerized liquid is stored in a vat, and through visible or UV light irradiation, this liquid is cured and/or hardened layer upon layer, providing the desired object. The light source initiates the polymerization reaction, which generates the formation of polymer chains or cross-links, thus forming a solid resin. In this physical-chemical process, the generation of the chain (solid resin) is irreversible and can no longer be changed to liquid form [37]. This technique can be classified according to the curing method that may employ lasers and is called stereolithography (SLA); digital projection, called digital light processing (DLP); diodes (LEDs) and oxygen known as continuous digital light processing (CDLP) and liquid production at the interface (CLIP) [27].

For example, in SLA printing technology, the platform of object construction, also called a bed, is immersed in a tank containing the light-curing liquid with its face facing downwards. As the laser is focused using a set of mirrors [27,38], the resin solidifies selectively, following the sliced image model (*.stl* file) provided to the printing software. After a layer is formed, the platform moves a distance estimated by G-code, which can vary from 12 to 150 µm depending on the characteristics of the printer used, and the

process is repeated until the part is completed, layer upon layer [27]. After printing, objects generally require additional processing under UV light to ensure optimal mechanical properties [39]. Some advantages, such as greater printing precision and resolution, are observed through this technique, which allows the printing of parts with more complex and detailed geometries with small layer heights (≈20 μm) [27]. Furthermore, SLA printers are typically smaller and quieter than other 3D printing technologies. However, the SLA printing process has some disadvantages, such as high cost of light-curing resins, difficulty in obtaining colored objects, as the color of the resin can often complicate the polymerization process, requires more time for printing (10-20 mm h^{-1}) when compared to other techniques, and most printing parts requiring the use of supports [27].

The MJT technique involves the selective deposition of droplets of photopolymerizing material deposited using UV lamps [36,40]. For this purpose, thanks without the presence of air are used to store the photopolymer resins, which are deposited as drops, forming very thin layers (~16 μm) on the build platform, after which UV light cures the material [40]. In general, the MJT technique is similar to VPP because both involve the use of photopolymerized liquids in the formation of parts; however, MJT presents some advantages, such as low waste due to the directed jet (droplets) that allows the entire material to be used. Furthermore, this technique has high precision and the ability to form colorful objects. However, the photopolymerizing liquids used in the MJT technique have weaker mechanical properties after the material has cured, making it difficult to use in functional prototypes. In addition, printers that use this technique are the most expensive compared with other 3D printing technologies [41].

The BJT method is a printing process in which an object is constructed by applying a binding agent to a layer of powdered material [42,43]. In this technology, a powdered material is spread on the printing platform through which compression roller passes. The movement of the print head causes droplets of binder to be applied, which binds the powder particles to produce the object layer by layer. After deposition, the platform is exposed to a fixed amount of heat. This process is repeated until a complete object is formed [43]. Among the main advantages of this technique is the possibility of using different materials, including metals [44], ceramics [45], and polymers [42]. Furthermore, this technique has low material waste and high dimensional accuracy. However, machines based on BJT method l have a high cost and often require a further

procedure to finish the printed parts, as in the case of metallic and ceramic objects, which generally require cleaning chambers and sintering furnaces to evaporate the binding material [42].

In contrast, in the PBF technique, a thin layer of powder is deposited on the printing bed and an energy source (laser or electron beam) is used to sinter the powder particles, as previously specified in the *.stl* file. After this process, a new layer of powder is applied, and the process is repeated until the object is formed [36]. This technique can be subdivided into selective laser sintering (SLS), selective laser melting (SLM), direct metal laser sintering (DMLS), direct metal laser melting (DMLM), and electron beam melting (EBM) according to the powder fusion process [46,47]. In this type of printing, there is generally a powder distribution system formed by a piston responsible for supplying the powder and another responsible for holding the manufactured part, in addition to the energy supply system (laser or electron beam)[38].

The DED technique is similar to PBF; however, in this case, the energy source is focused (usually a laser or electron beam) to melt a metallic powder in a hermetically sealed chamber containing an inert gas to avoid oxidation processes on the metallic surface. Unlike PBF, in the DED process, the powder is not placed on a bed. In this case, the focused energy source melts the material as it is deposited. The energy is used to heat the substrate, melt it, and simultaneously deposit the material in the molten pool substrates. The power source is moved according to the cross-section of the model defined in the *.stl* file. The molten metal solidifies as the electron beam moves, and a new layer is deposited [38,48].

In SHL process, sheets of material containing adhesive are overlapped on one side to make it possible to build the object layer-by-layer with the help of a laser source. Generally, a material is wound on a coil that deposits its sheet on a platform where a heated roller passes over its surface, activating the adhesive that makes it possible to join its layers [36,49].

Finally, MEX printing is based on the extrusion of a material. In this technique, the material is forced by a speed-controlled motor and extruded through a temperature-controlled nozzle, being deposited layer-by-layer until the final piece is formed. This type of technology is the most reported in the literature in the development of devices, sensors, and other applications [6]. Its popularity is associated with the development of open-source printers, which has encouraged the construction of numerous commercially

available models. MEX is classified into two large groups: Direct ink laser-assisted writing (DIW, or also known as Robocasting), which uses an ink in the liquid phase of known viscosity through a small nozzle under controlled flow, and FDM, which employs thermoplastic filaments [38,50]. Among these, the FDM technique stands out due to its low cost, simplicity, and versatility of application [51,52], being the most reported technique in the development of electrochemical sensors [6]. **Table 1** summarizes some characteristics of 3D printing technology, including resolution and materials used in each technique.

Table 1. Some characteristics of 3D-printing techniques.

Techniques	Resolution	Material	Advantages	Disadvantages
SHL	100 µm	Polymer Metal Sheets	• Utilization of inexpensive material; • Fast and accurate	• Prone to fire hazard; • Not as good as materials used with other rapid prototyping techniques • Low dimensional accuracy
VPP	1 – 150 µm	Photopolymer Photoresin Resin (Acrylate or epoxy based with proprietary photo initiator)	• High resolution; • Support structure is not required; • Good for complex built; • High strength and time efficient.	• Expensive process • The post-processing method is mandatory due to its roughness • Need of post processing under UV light to ensure optimal mechanical properties; • Difficulty in obtaining colored objects.
DED	50-200 µm	Metals	• Possibility of printing metal alloys	• More expensive than other 3D-printing technique • Require laser that compromise part resolution;

Techniques	Resolution	Material	Advantages	Disadvantages
MEX	100-250 µm	Polymer, composite	• Rapid processing speed; • Less processing time; • Lower cost than other 3D-printing technology	• Low resolution; • Requires support; • The binder fabricated porous structures; • Feeble mechanical properties.
BJT	10-100 µm	Ceramics, metals and polymers	• can incorporate functionally-graded materials • Creation of large objects	• mechanical property (and even geometric accuracy) requirements are limited
PBF	10-100 µm	Metallic powder, polymer, ceramic	• No support material needed; • High resolution; • High strength and time efficient	• The post-processing is mandatory due to its roughness; • High-cost material; • Poor control over surface topography.
MJT	20 µm	Photopolymers	• Low waste than other 3D-printing techniques; • Possibility to produce color objects.	• High cost; • Post treatment is required; • Poor mechanical properties

1.3 Fused Deposition Modeling (FDM)

As mentioned previously, the FDM technique has been the most explored in the development of sensors and electrochemical devices. This became more pronounced after the manufacture and commercialization of composite filaments, attributing electrical conductivity to filaments composed of a mix of thermoplastic polymers (nonconductive) and conductive materials. In the FDM technique, the printing process requires the use of thermoplastic filaments, which are heated until the melting point is achieved when passing through an extrusion nozzle heated to the appropriate temperature. When expelled through the extrusion nozzle, the filament is deposited on a platform (or table) in layer-by layer process [22]. In general, the nozzle moves in different directions of the plane (x, y and z); however, there are printers in which the nozzle moved in the x and y directions of the plane, while the table moves along the z-axis, thus forming printing layers of thermoplastic polymer when constant pressure is applied. Soon after the deposition of the polymer, its cooling and consequent hardening occur, resulting in the desired 3D object [6,53]. This process occurs in a completely automated manner, which minimizes possible errors in the manufacturing process.

Among the polymers most used in the manufacture of objects by FDM are acrylonitrile butadiene styrene (ABS) and polylactic acid (PLA); however, several others materials can be used, such as polycarbonate, nylon, polyethylene terephthalate (PET), and polyvinyl acetate (PVA), among others [6]. ABS is widely used because of its good mechanical resistance and adequate extrusion temperature (between 200 and 250 ºC), allowing its easy use in FDM-type printers [21]. However, it produces toxic styrene vapors, making its use difficult in closed or unventilated places [6]. PLA is a biodegradable and relatively low-cost polymer with an extrusion temperature close to 230 ºC, and it has been widely used due to its attractive characteristics and is the basis for the synthesis of composite filaments [21].

The use of FDM technique for the production of 3D objects allows the extrusion of composite (conductive) filaments, which are capable of providing, for example, electrical conductivity to the printed material through the use of composite polymers for printing [54]. As a result, there has been an expansion in the applicability of 3D printing

in chemistry, enabling the printing of conductive substrates that can serve as electrodes in electrochemical analyses [6,55].

In this context, the use of metallic nanoparticles is an excellent option to provide electrical conductivity to these materials; however, in general, these materials tend to be more expensive compared to carbon-based materials [54]. Carbonaceous materials such as graphene , graphite, carbon black (CB), and carbon nanotubes (CNTs) have been widely used in the manufacture of composite filaments due to attractive features such as high electrical conductivity, and relatively low cost [54]. CB is a material of great interest for use in the manufacture of conductive filaments due to its extremely low cost, since it can be obtained as a by-product of the combustion of petroleum products, and can provide excellent electrical properties, ideal for the construction of electrochemical sensors [56]. Graphene consists of a 2D material with unique electrical, optical, and physicochemical properties, which has been widely explored in the printing of various conductive devices, with applications ranging from obtaining electrical circuits [57] and devices for storing energy [58], in addition to their use as electrochemical sensors and biosensors [6,59]. In fact, graphene and CB are the materials most used in the construction of 3D-printed electrodes using the FDM technique [21]. These conductive materials were largely used due to the availability of affordable commercial filaments containing graphene in a PLA matrix (G/PLA), called Black Magic®, and CB in a PLA matrix (CB/PLA), called Protopasta® [59]. Currently, Black Magic® is no longer commercially available; however, its use has been highly explored in the printing of electrochemical sensors.

1.4 Synthesis of Conductive Filaments Applied to Electroanalysis

In the field of electrochemistry and FDM, the emerging challenge lies in the production of bespoke filaments tailored for particular uses and understanding the behavior of the base materials. The development of conductive filaments for FDM has captured significant attention in recent times. These tailor-made conductive filaments are at the heart of thorough research, involving trials with various materials and combinations for additive manufacturing, with a keen focus on manufacture of electronic components [6]. Following the introduction of the pioneering custom-made conductive filament, scientists have proposed new methods to navigate past certain constraints and customize them for distinct laboratory environments. Two main techniques have emerged: one that

produces conductive composites via solvent-based processes, and another that employs thermal-based methods. Importantly, an extrusion step is generally essential after the initial method to shape the filaments into a form suitable for additive manufacturing [60].

In solvent-based methods, the thermoplastic polymer is dissolved, and the conductive carbon material can be easily dispersed in the matrix. The solvent is then removed by evaporation and drying, forming a solid composite material. In general, this method provides a homogeneous mixture and reduce agglomeration of the conductive particles; however, this route requires the use hazardous solvents to produce conductive filaments.

On the other hand, in thermal procedures, the polymer and the conductive filler are heated, melted and mixed in a sealed chamber. This method is faster than the solvent procedure. Moreover, it does not need the use of toxic organic solvents (environmentally friendly). However, it is necessary to use costly equipment and infrastructure, which may difficult its application in common research laboratories.

Recent studies have highlighted the creation of innovative carbon-based conductive filaments, which are more cost-effective than their commercial counterparts [5]. These custom-made filaments are produced using a variety of thermoplastic polymers, such as PLA, ABS, polystyrene, polypropylene, and modified polyethylene terephthalate glycol, combined with conductive agents like graphite, graphene, carbon black, carbon nanofibers, carbon nanotubes, and various metals. The proposed process involves mixing and melt extruding of these materials. Utilizing an extruder, similar to those used in 3D printer, the filament is heated and formed, ensuring a uniform distribution of all components within the polymer matrix. It is crucial to balance the ratio of components to preserve constant-electrical conductivity and print quality. An appropriate amount of conductive material is necessary (higher conductivity), but an overabundance can adversely affect the mechanical properties of conductive thermoplastic filaments, including stiffness, viscoelasticity, tensile strength, and yield strength. Moreover, the production of these new filaments offers notable benefits, such as customizable conductivity levels which can overcoming the main limitation of commercial conductive filaments (high surface resistance for sensors) and the integration of electrocatalysts to enhance electrochemical properties. **Table 2** summarizes some lab-made filaments for FDM printing reported in the literature.

Table 2. Some works reported in the literature for filament production applied in FDM printer.

Polymer	Conductive filler / wt.	Method	Application	Ref.
PCL	CB (15%)	Solvent	-	[61]
PLA	CB (28.5%)		Catechol, hydroquinone and H_2O_2 sensor	[62]
PLA	Graphene (20%)		Anodes in Lithium iron batteries	[63]
PLA	Graphene (20%)		Supercapacitors	[64]
PLA	Graphite (40%)		SARS-Cov-2 detection	[65]
PLA	Graphite or graphene (15-25%)		Electrodes	[66]
ABS	rGO (0.4-5.6%)		-	[67]
PLA and PCL	GNP (10-25%)	Thermal Mixing	Circuits	[68]
PI-PLA	CB (29.6%)		Caffeine sensor	[69]
rPLA	CB (15%) and graphite (10%)		Oxalate sensor	[70]
rPLA	CB (15%) MWNCT (10%)		Yellow fever virus	[71]
rPLA	CB (25%)		Bisphenol A sensor	[72]

Polymer: PLA: Poly(lactic acid); rPLA: recycled PLA; ABS: Acrylonitrile Butadiene Styrene; PCL: Polycaprolactone; PI-PLA: recycling of post-industrial waste poly (lactic acid). **Conductive material:** CB: Carbon black; GNP: graphite nanoparticles; MWNCT: Multiwall nanotube carbon.

1.5 Post-treatment of 3D-printed Electrodes

A key factor contributing to the high performance of unmodified 3D-printed sensors is the ability to perform treatment or activation processes directly on the electrode surface before use [6,73]. Generally, this procedure enhances the electrochemical characteristics of these electrodes significantly. The idea of "treatment" or "activating" of the surface of the obtained 3D-printed electrodes was of great importance for the growth in the use of this kind of sensors in electroanalysis. The process basically involves the elimination/removal of excessive polymeric material present on surfaces of native 3D-printed electrodes and consequent greater availability of the conductive material of the composite. The literature documents various treatment methods in order to improve the

performance of native 3D-printed electrodes. These procedures include chemical and/or electrochemical processes, treatments without use of reagents (environmentally-friendly), and methods integrating different treatments types. Each approach has its unique aspects, and in the quest to enhance electrochemical performance, several studies have adopted a mix of these preliminary treatments. A prevalent method involves mechanical polishing before treatment or activating of the surface through other procedures. This polishing step aims to achieve a smoother electrode surface, and/or partial removal of the insulating layer of PLA. Each pretreatment method offers distinct advantages and disadvantages, and selecting the most suitable one should be based on user objectives, which include considerations of time-consuming, use or non-use of chemicals and/or equipment's, manual or automatic procedure, and the interaction between the analyte and the 3D-printed electrode surface [74].

1.5.1 Chemical and/or electrochemical treatments on surface of 3D-printed electrodes.

Pumera and co-workers proposed an immersion in different organic solvents to partially remove of PLA on the 3D-printed electrode surface [75]. For this purpose, the 3D-printed composite (graphene and PLA) electrodes were immersed solvents such as acetone, dimethylformamide (DMF), methanol and/or ethanol for 7 min. After that, the electrodes were washed with deionized water, dried (~24 h), and evaluated using a $[Fe(CN)_6]^{3/-4-}$ as redox probe. According to the authors, no signals were observed when protic solvents were assessed. On the other hand, the voltammetric profile (peak-to-peak separation) was slightly better when aprotic solvents were used (ΔEp (acetone) = 296 mV and ΔEp (DMF) = 416 mV). Although the authors showed a significant enhancement in the electrochemical response, the use of hazardous organic solvents were required (non-eco-friendly). Moreover, it is also time-consuming since that the 3D-printed electrode may be dried for 24 h.

Another strategy to improve the electrochemical activity of 3D-printed electrodes is the use of electrochemical activation. Dos Santos *et al*. showed that applying +1.8 V *vs.* $Ag|AgCl|KCl_{(sat.)}$ for 900 s followed by -1.8 V/50 s *vs.* $Ag|AgCl|KCl_{(sat.)}$ in 0.1 mol L^{-1} phosphate buffer (pH = 7.2), remove partially PLA (exposition of nanostructured graphene fibers). Moreover, there was an insertion of oxygenated groups on the electrode surface, achieving a ΔEp of 185 mV for the $[Fe(CN)_6]^{3-/4-}$ probe [76,77]. Electrochemical

procedures in alkaline medium were also assessed due to PLA is susceptible to saponification reaction in which hydroxide ions react with electrophilic carbonyl presented in the ester group of the PLA polymer. In this sense, Wirth and collaborators [55] displayed the use of water electrolysis to generate OH^- for partial removal of PLA, using 3D-printed electrodes produced from different composites (G/PLA and CB/PLA). Although, this is an interesting approach to treat 3D-printed electrode surfaces, the ΔEp values for $[Fe(CN)_6]^{3-/4-}$ probe (300 and 1000 mV for G/PLA and CB/PLA, respectively) were not satisfactory when compared to other works in the literature [73]. A simple combination of pretreatments highly employed in the literature for CB/PLA types electrodes is mechanical polishing followed by one-step chemical/electrochemical activation, as detailed by Richter *et al*. [9]. The authors performed the one-step chemical/electrochemical activation of the 3D-printed electrode surface using 0.5 mol L^{-1} NaOH solution (chemical) and the following sequence of potential values (electrochemical) and application times (+1.4 V/200 s and −1.0 V/200 s). A considerable improvement (current increase and better reversibility) in the electrochemical behavior of the 3D-printed electrode was observed when model molecules such as dopamine, uric acid, ascorbic acid, hexaammineruthenium (III) chloride and the ferri/ferrocyanide were used as redox couples [9].

Another mode to activate 3D-printed electrode surfaces is the use of reducing agents such as ascorbic acid and/or sodium borohydride. Redondo *et al*. [78] proposed an activation protocol in two steps: *(i)* firstly, G/PLA electrodes were electrochemically treated through application of constant potential (+2.5 V/1000 s *vs.* $Ag|AgCl|KCl_{(sat.)}$) in 0.1 mol L^{-1} phosphate buffer (pH = 7.4); *(ii)* After that, 3D-printed electrodes were immersed in ascorbic acid or sodium borohydride solutions (both 0.1 mol L^{-1}) for 24 h. Despite the use of eco-friendly reagents, the procedure is time consuming and the improvement in the electrochemical response (ΔEp(ascorbic acid) = 680 mV and ΔEp(sodium borohydride) = 620 mV for $[Fe(CN)_6]^{3-/4-}$ redox couple) is not better than other works in the literature [12]. Silva and collaborators [79] also explored the reducing agent sodium borohydride for the treatment of G/PLA electrodes. Firstly, the 3D-printed electrode was immersed in DMF solution (15 min) and washed with ethanol. After this, the electrode was sequentially immersed in two solutions: 1 mol L^{-1} nitric acid and 0.15 mol L^{-1} sodium borohydride, both for 15 min. Interestingly, a notable voltammetric profile (current intensity and ΔEp = 130 mV) was observed for ferrocene-methanol probe.

Despite greater electrochemical response, the treatment still involves the use of toxic organic solvents.

An elegant way to remove PLA on electrode surface is a biocatalytic treatment. In this context, PLA was partially removed from the electrode surface through incubation in proteinase K (wide-spectrum protease) during 28 h. The authors achieved cyclic voltammograms with peak to peak separation of 350 mV for ferricyanide redox couple [80]. However, a long time is required, and the use of enzymes can be difficulted since they are affected by pH, temperature, humidity, etc.

1.5.2 Reagentless treatments

Mechanical polishing is usually favored treatment of working electrodes due to its simplicity, which facilitates the regeneration and subsequent reuse of electrodes. Cardoso and collaborators proposed a mechanical treatment of 3D-printed electrodes using sandpaper (1200 grit) wetted with deionized water (30 s). After the procedure, enhancement in the current response was achieved for catechol, dopamine and $[Ru(NH_3)_6]^{2+/3+}$. Thermal annealing procedure was developed by Pumera's group [81]. In this work, 3D-printed G/PLA was isotopically decomposed by heating, under vacuum at 350 ^oC (3 h). The authors displayed a peak-to-peak separation of 255 mV for ferricyanide couple. This method is a green alternative activation process, but it is costly and time-consuming.

Laser ablation is another route to enhance the electrochemical activity of 3D-printed electrodes. According to Glowacki and co-workers [82], when a laser with determined energy is irradiated at the 3D-printed electrode surface, the composite was molten, breaking the polymer chains after the re-melting mechanism. In fact, some works using CO_2 laser [83] or laser at 1064 nm [82], showed significative improvement in the electrochemical response of 3D-printed CB/PLA electrodes. Furthermore, plasma treatment was proposed by Silva, Rocha and co-workers [84]. In this context, the 3D-printed CB/PLA was subjected to O_2 plasma treatment for 2 min. A considerable improvement in the electrochemical response was achieved since that it was observed a peak-to-peak separation of 156 mV and a relation between anodic and cathodic currents of 1.1. **Table 3** summarizes a comparison between some activation/treatment reported in the literature.

Table 3. Comparison of some works regarding to 3D-printed surface treatments, using $[Fe(CN)_6]^{3-/4-}$ probe.

Treatment method	Electrode	ΔEp /mV	Time	Ref.
Electrochemical	CB/PLA	150	400 s	[9]
Immersion	G/PLA	416 (DMF) 296 (acetone)	24 hours	[75]
Oxygen plasma	CB/PLA	156	2 min.	[84]
Physical thermal annealing	G/PLA	255	4.3 hours	[81]
Enzymatic digestion	G/PLA	350	28 hours.	[80]
Electrochemical	G/PLA	180	30 min.	[77]
Laser-scribing	CB/PLA	130	< 1 min.	[83]
Laser-ablation	CB/PLA	161	-	[82]
Reducing agents	G/PLA	680 (ascorbic acid) 620 (sodium borohydride	< 24 hours	[78]

1.6 Application of 3D-Printed Electrochemical Sensors

3D printing technology, specially fused deposition modeling (FDM), has been widely used in studies with the aim to mass-scale production of bespoke and cost-effective devices in many areas, including the electrochemistry [5,6]. In this field, 3D printers are employed to produce batteries [7], electrochemical cells [85,86], and sensors [12]. The ease of production of complete electrochemical sensing with reduced cost, enable the development of electrochemical sensors with comparable performance to conventional carbon-based electrodes. In fact, researches indexed in Web of Science® database with the keywords *"3D-printing and electrochemical sensors"* showed that 51.3% of the published works correspond to the development of methods to detect different analytes in forensic, biological, environmental, fuels, and pharmaceutical samples [12,53,87].

In 2015, Ragones and co-workers [88] showed the possibility of the application of the 3D printing technique in electroanalytical chemistry. For this purpose, they developed a 3D-printed electrode composed by polydimethylsiloxane (PDMS) and graphite powder composite for the detection of biomarker alkaline phosphatase from colon cancer. In 2018, Palenzuela *et al*. produced disc shaped 3D-printed electrodes based on graphene/polylactic acid. The authors treated the electrodes with immersion DMF and evaluated the sensor's performance in detecting of ascorbic acid, ferricyanide and $Ru(NH_3)_6]^{2+/3+}$ [89]. In the same year, our laboratory showed the fabrication of 3D-printed BIA system combined with a 3D-printed G/PLA electrode and the detection of dopamine has been demonstrated as proof of concept [90]. After that, many other works were developed using the 3D-printing technology with applications in electroanalysis. **Table 4** summarizes some works reported in the literature about this topic.

Table 4. Some electrochemical sensors reported in the literature produced using 3D-printing FDM technology.

Filament	Treatment	Analyte	Sample	Analytical technique	LOD	Ref.
G/PLA	Mechanical polishing	Dopamine Catechol	-	BIA-AMP SWV	0.10 µmol L^{-1} 0.04 µmol L^{-1}	[90]
G/PLA	Mechanical polishing	TNT	Contaminated surface with TNT	SWV	0.40 µmol L^{-1}	[91]
G/PLA	Thermal Annealing	Picric Acid	-	CV	0.10 µg L^{-1}	[81]
G/PLA	Chemical	Glucose and sucrose	-	CV and CA	-	[92]
G/PLA	Chemical and electrochemical	L-methionine	Human Serum	SWV	1.39 µmol L^{-1}	[93]
C/ABS	No treatment	Paracetamol Caffeine	Pharmaceutical effervescent tablets and Urine	DPV	0.43 mg L^{-1} 0.39 mg L^{-1}	[94]
CNT/PLA	No treatment	H_2O_2		CV	1.20 µmol L^{-1}	[95]
CB/PLA	No treatment	Hg^{2+}	Bottled water and Fish oil	DPASV	0.52 µg L^{-1}	[96]
CB/PLA	No treatment	Hg^{2+} Caffeine	-	SWASV DPV	1.90 µg L^{-1} 1.80 g L^{-1}	[97]
CB/PLA	Laser ablation	Caffeine	-	CV and DPV	0.40 µmol L^{-1}	[82]
CB/PLA	Mechanical polishing and electrochemical	Cu^{2+}	Bioethanol	SWASV	0.10 µg L^{-1}	[98]
Gpt/PLA	No treatment	TNT	Water Samples	SWV	0.2 µmol L^{-1}	[99]
Gpt/PLA	No treatment	SARS-CoV-2	-	CV	0.38 µg mL^{-1}	[65]
CB/Gpt/rPLA	Electrochemical	Oxalic acid	Synthetic urine sample	SWV	5.7 µmol L^{-1}	[70]
CB/rPLA	Electrochemical	Atropine	Gin and Whisky	BIA-AMP		[100]

Electrodes: CB/PLA: Carbon black and PLA; **G/PLA:** graphene and PLA; **CNT/PLA:** carbon nanotube PLA; **Gpt/PLA:** graphite and PLA; **CB/Gpt/rPLA:** Carbon black, graphite and recycled PLA; **CB/rPLA:** Carbon black recycled PLA; **C/ABS**: Carbon-loaded ABS electrodes; **Techniques: CV:** Cyclic voltammetry; **SWV:** Square wave voltammetry; **DPV:** differential pulse voltammetry; **BIA-AMP**: Batch injection with amperometric detection; **DPASV**: differential pulse anodic stripping voltammetry; **SWASV**: square wave anodic stripping voltammetry.

2 OBJECTIVES

The general objectives in this thesis were to explore the 3D-printing FDM technology to produce 3D-printed electrodes for electroanalytical applications.

In the first work, $Ni(OH)_2$ microparticles were incorporated into the matrix of a commercial Black Magic® filament to produce of a non-enzymatic electrode for the selective determination of glucose. The 3D-printed electrode was coupled to a batch injection analysis system (BIA) with amperometric detection in order to improve the detectability and analytical frequency. Characterizations by thermogravimetry, Raman spectroscopy, scanning electron microscopy (SEM), and X-ray fluorescence were used to evaluate the incorporation of microparticles into the polymeric conductive matrix.

In the second study, the objective was to synthesize a Prussian blue film using iron ions present as impurities in in a commercial conductive filament (Black Magic®). The material was characterized by Raman spectroscopy, cyclic voltammetry (CV), and X-ray fluorescence. Furthermore, the Prussian-blue-modified 3D-printed electrode was used for the amperometric detection of H_2O_2 in milk samples using the BIA system.

The third and last work to be presented in this thesis aimed to evaluate how printing parameters (perimeter number, printing speed, printing orientation, and layer thickness) affect the electrochemical response of the 3D-printed sensors. CV, electrochemical impedance spectroscopy (EIS), and Raman spectroscopy were used to evaluate the effect of the printing parameters on the performance of 3D-printed electrodes. Furthermore, multivariate analysis using the Multivariate Curve Resolution method with alternating least squares (MCR-ALS) was used to extract more information from Raman spectra data in order to verify how printing parameters interfere with the arrangement of conductive particles in the conductive polymer matrix.

3 RESULTS

The studies caried out during this thesis led to the publication of three scientific articles. In this text, we chose to present the three scientific articles separately and in chronological order of publication. The first paper reports the production of 3D-printed electrochemical sensors produced from commercial conductive filaments modified with nickel microparticles for glucose detection (**Annex I**). The second paper reports the synthesis of Prussian blue from iron impurities present in a commercial conductive filament. Then, the Prussian blue 3D-printed electrode was applied for amperometric detection of hydrogen peroxide (**Annex II**). Finally, the third paper addresses the

influence of printing parameters of a 3D-printer on the performance of 3D-printed electrodes obtained using the FDM technique (**Annex III**).

The description of the experimental procedure steps, results, and discussions, in addition to the conclusions of each work will be presented in the respective **Annexes: I**, **II** and **III.**

4 ANNEX 1. Production of 3D-printed disposable electrochemical sensors for glucose detection using a conductive filament modified with nickel microparticles.

4.1 Introduction

In recent years, 3D printing technology, also known as additive manufacturing, has received great attention due to its ability for rapid and low-cost production of complex three-dimensional prototypes and devices. This technology is emerging to provide numerous applications in different areas, such as healthcare, biomedicine, pharmaceutical, engineering, chemistry, and electrochemistry, among others [22,101]. The numerous applications in the field of electrochemistry allow technological advances in the development of devices ranging from energy store [58], energy conversion (water splitting) [102,103] to sensors [21,104].

Taking advantage of 3D printing technology in the fields of sensing and electroanalysis, both conductive and non-conductive filaments have been used successfully in the printing of electrodes (sensors) as well as electrochemical cells (stationary state and flow systems), respectively. The most popular 3D printing mode is via fused deposition modeling (FDM), which employs thermoplastic filaments to create layer-by-layer three-dimensional structures. In this sense, polylactic acid (PLA), acrylonitrile butadiene styrene (ABS), polybutylene and polystyrene containing carbon conductive materials have been explored for the production of electrochemical sensors [58,89,97,104,105]. Nonetheless, the electrochemical response of newly printed electrodes was fairly poor if compared to other carbonaceous surfaces [58,105]. Given this limitation, 3D printed electrochemical sensors require previous pre-treatments (activations) [9,75,80,81,91,106,107] or surface modification to improve the conductivity before use as electrode [77,103,108,109].

Several strategies have already been used to improve the electrochemical properties of 3D-printing electrodes, such as mechanical polishing [16, 21], electrochemical activation [76], immersion in solvents [75], physical methods of thermal annealing [81], biological digestion using enzymes [80], water electrolysis generating hydroxide [55] and chemical/electrochemical activations [9]. Basically, all strategies were used to partially remove the non-conductive material from the surface and to expose

the conductive nanomaterial. Moreover, procedures for the modification of 3D-printed surfaces were also reported, such as the use of gold sputtering followed by polypyrrole electropolymerization for detection of copper [105], electrodeposition of Prussian blue nanoparticles for the detection of peroxide [77] and the electrodeposition of bimetallic hydroxide films (Ni-Fe) for electrocatalytic oxygen evolution in alkaline medium [103].

The possibility of use of 3D printed electrodes for the production of biosensors has also been reported [18, 24]. 3D-printed graphene/PLA electrodes modified with glucose oxidase [108] or with horseradish peroxidase [110] were used for selective amperometric detection of glucose in biologic samples after enzymatic conversion of glucose to hydrogen peroxide. However, the use of biosensors can present robustness problems once the activity of enzymes is easily affected by pH, temperature and/or humidity [111,112]. Furthermore, laborious steps such as adsorption, cross-linking or electropolymerization are required for the immobilization of enzymes on electrode surfaces. For this reason, electrochemical sensors using non-enzymatic materials for glucose detection has been promising due to some advantages, including stability, reproducibility, low cost, and easier construction. As shown in the literature, many metals (copper, gold, platinum, cobalt) have catalytic properties for the electrochemical oxidation of glucose [113–115].

Nickel-based materials have shown promising electrocatalytic activity for the electrochemical oxidation of alcohols [116,117] and carbohydrates [118–120]. In comparison to other metals, nickel compounds are much more abundant and present high stability in alkaline medium [121]. The electrocatalytic oxidation of glucose depends on the formation of $Ni(OH)_2$/NiOOH in alkaline medium [118,122]. In the literature, the use of carbonaceous surfaces modified with Ni particles has been employed successfully for the construction of sensors for the selective detection of glucose [113,123–125]. However, the development of electrodes modified with nickel often involves laborious manual steps which increase the cost and time required in the construction of them. In this sense, the production of conductive filaments based on Ni microparticles can be advantageous for direct printing of modified electrodes (without laborious and time-consuming modification steps). Some authors have been exploring the incorporation of metals within conductive polymeric matrices in order to increase the electrocatalytic properties of printed sensors. Hughes *et al.*[102] fabricated two types of conductive PLA filaments, through modification of the PLA matrix with 2D-$MoSe_2$ (10%)/ electro-

conductive carbon (15%) and with Pt on carbon (20%) for use as the cathode and anode, respectively. According to the authors, the 3D-printed material had an effective catalytic effect in the electrochemical water splitting process. In another example described in the literature, the authors reported the introduction of Cu-Ag core-shell nanowires in polycaprolactone (PCL) matrix to fabricate composite polymer filaments with higher conductivity [126]. The new proposed filament presented a resistivity of 0.002 Ω cm (100 times more conductive than commercially available graphene-based 3D printing filaments), thus considered a promising material for electronic and electroanalytical applications.

In the present study, the development of a new conductive composite filament based on the incorporation of $Ni(OH)_2$ microparticles within the graphene/PLA (G-PLA) matrix is presented. Both conductive composites (before and after modification with $Ni(OH)_2$) were characterized by thermal gravimetry, Raman spectroscopy, scanning electron microscopy and electrochemical methods. The 3D-printed electrodes using the new conductive filament were used for the development of a simple, low-cost, and non-enzymatic sensor for the selective determination of glucose.

4.2 Materials and methods

4.2.1 Chemical and samples

Highly pure deionized water (R ≥ 18 MΩ cm) obtained from a Millipore Direct-Q3 system (Bedford, MA, USA) was used to prepare all aqueous solutions. Glucose was obtained from Henrifarma (São Paulo, Brazil), sodium hydroxide from AppliChem Panreac (Barcelona, Spain), ascorbic acid from Vetec (Duque de Caxias, Brazil), potassium hydroxide from Synth (Diadema, Brazil), uric acid, $Ni(NO_3)_2\ 6H_2O$ and urea from Sigma Aldrich (Steinheim, Germany). All reagents were of analytical grade and used without further purification. The commercial conductive filament was composed by a mix of graphene and PLA (G-PLA) and was purchased from Black Magic 3D (volume resistivity of 0.6 Ω cm; New York, USA). Glucose, uric acid, ascorbic acid and urea solutions were freshly prepared just before the experiment by dissolution in supporting electrolyte (0.1 mol L^{-1} NaOH), as previously described in the literature [127–129].

4.2.2 Synthesis of $Ni(OH)_2$

The synthesis of $Ni(OH)_2$ was carried out using the chemical precipitation method [130,131]. Briefly, the procedure consisted of mixing (magnetic stirrer) of an aqueous solution of 0.3 mol L^{-1} KOH with 0.07 mol L^{-1} $Ni(NO_3)_2$ $6H_2O$ during 3 h to form a nickel hydroxide slurry. After that, the slurry was immediately separated from the solution by centrifugation, washed with deionized water until the supernatant liquid had pH around 6. Finally, the slurry was dried at 100 ºC under vacuum for 12 h.

4.2.3 Production of the modified filament and the 3D printed electrode

Commercial conductive filament purchased from Black Magic® (G-PLA) was used to incorporate $Ni(OH)_2$ microparticles previously synthetized. For this propose, a mixture containing 30 g of G-PLA (cut into small pieces) and 3 g of $Ni(OH)_2$ was solubilized in 250 mL of a solution composed by acetone and chloroform (3:1; v/v). Then, the material was dried at 100 °C in an oven for 12 h, cut into small pieces. Before the experimental procedures here described, many attempts were made to add the maximum amount of Ni catalyst while preserving the printability of the filaments. The relation 1:10 (catalyst/polymer; w/w), respectively, proved to be the best condition without severely diminishing the mechanical properties of the final material.

Figure 3 shows a scheme of the filament production and 3D printing of the Ni-G-PLA electrode. Firstly, the material containing PLA and $Ni(OH)_2$ microparticles was placed in a Filmaq 3D extruder (Curitiba, Brazil) at a temperature of 220 °C and the modified filament was extruded a screw speed of 30 rpm through a nozzle with inner diameter of 1.75 mm (Ni-G-PLA filament diameter) (**Figure 3A**). Then, the new filament was used to 3D print hollow square boxes (4 cm x 4 cm x 1 cm) with wall thickness of 0.72 mm in a vertical orientation (**Figure 3B**), using an open-source Graber i3 RepRap 3D printer (220 ºC of extrusion temperature, 70 ºC of bed temperature, and 0.8 mm nozzle) [90]. Square pieces were cut (1 cm x 1 cm) from the 3D printed hollow square box (**Figure** 3B) and were used as the working electrode in cyclic voltammetric and amperometric measurements. **Figure 3C** shows that the 3D printed electrode (square piece) was positioned at the bottom of the batch injection analysis (BIA) cell (wall-jet configuration).

Before use, the 3D electrodes were polished with abrasive paper (1200 Grit) wetted with deionized water for 30 s. After that, the 3D printed electrode was submitted

to an electrochemical pre-treatment (activation) adapted from the literature [9]. The activation (pretreatment) consisted in the application of +1.4 V (*vs* Ag/AgCl) for 200 s followed by -1.0 V (*vs* Ag/AgCl) for 200 s using 0.5 mol L^{-1} NaOH as the supporting electrolyte.

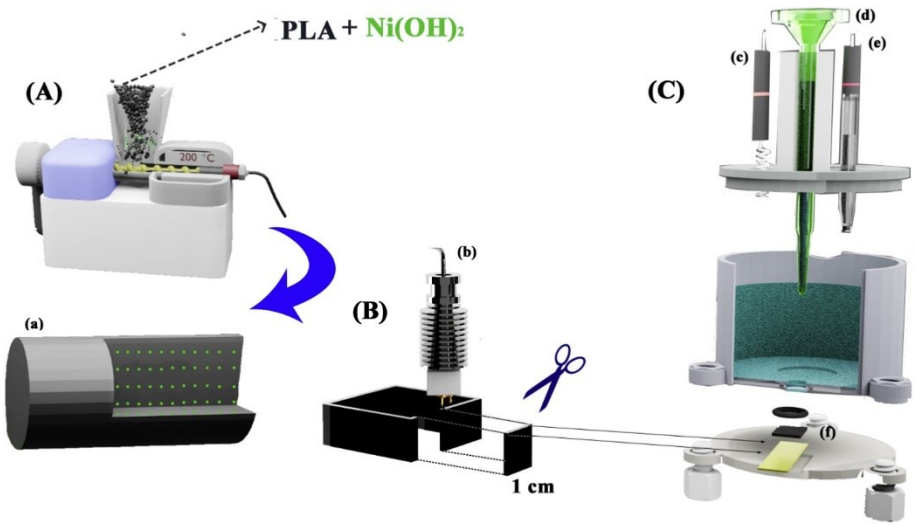

Figure 3. Schematic diagrams: **(A)** Production of the Ni-G-PLA filament using the 3D extruder; **(B)** 3D-printing of a hollow square box (4 cm×4 cm x 2 cm) with wall thickness of 0.72 mm; **(C)** The 3D-printing electrode (1×1 cm) is positioned at the bottom of the BIA cell on a metal plate (electrical contact); **(a)**illustration of Ni-G-PLA filament; **(b)** printer nozzle; **(c)** Pt counter electrode; **(d)** micropipette tip; **(e)** reference electrode ($Ag|AgCl|KCl_{(sat.)}$); **(f)** 3D printed Ni-G-PLA working electrode(1×1 cm).

4.2.4 Characterization techniques

The elemental composition of the materials was determined using energy dispersive X-Ray microfluorescence spectrometer (Shimadzu, microEDX 1300). The measurements were performed in the 0–40 keV range with acquisition time of 150 s. The surface morphology of the materials was analyzed by a FEI Quanta 250 field emission Scanning Electron Microscope (FE-SEM). Raman measurement was performed on the electrode surface using a confocal Horiba Jobin Yvon T64000 Raman confocal spectrometer using a 532 nm laser at 15 mW power and x50 lens. The crystallinity phase of the nickel hydroxide compound was investigated by XRD (X-ray diffractograms) collected in a Shimadzu 7000 XRD diffractometer (40 kV, 30 mA) with Cu-*K*α radiation

(λ = 1.5418 Å). The diffraction data were recorded at a scanning rate of 2.0° min^{-1} and 2θ angles between 10° and 90°. The thermal degradation of nickel hydroxide, PLA/graphene filament and modified filament with $Ni(OH)_2$ was investigated by thermogravimetric analysis (TGA) using an TG analyzer (Seiko Instruments TG/DTA 6200) from 25 to 1000 °C at a heating rate of 10 °C min^{-1} under oxidant atmosphere. The mass loss of samples was recorded and plotted as a function of temperature. The thermal properties were analyzed by differential scanning calorimetry (DSC) measurements performed with a TA Instruments (DSC 2910) equipment, heating from 25 to 250 °C at 10 °C min^{-1} under oxidant atmosphere. An empty aluminum pan served as a reference. The electrode specimens (8 - 10 mg) were analyzed under argon atmosphere (flow rate 50 mL min^{-1}). The melting temperature (T_m) was taken at the end of the melting peak, whereas crystallization temperature (T_c) was considered as the minimum of the exothermic peak. The area under the curve was calculated as the enthalpy according to the instrument software.

4.2.5 Electrochemical measurements

All electrochemical measurements were performed with a μ-AUTOLAB type III potentiostat/galvanostat controlled by NOVA 1.11 software. A mini Ag|AgCl saturated with KCl [132] and a platinum wire were employed as reference and auxiliary electrodes, respectively. The electrochemical measurements were performed at room temperature in the presence of dissolved oxygen. Cyclic voltammetric experiments were carried out using a 10 mL container and amperometric measurements were performed using batch injection analysis (BIA) system developed in our laboratory, as previously described [90]. All injections were performed using Eppendorf® electronic micropipette (Multipette® stream) with previous optimized injection volume and dispensing rate. The distance between the micropipette tip (Multipette® Combitip) and the working electrode was constant (2 mm). Reference and counter electrode were positioned at the top of the BIA system and the working electrode at the bottom of cell using a rubber O-ring in order to prevent leaks and define the geometric area of the electrode (ID = 0.54 cm; area = 0.22 cm^2). The electrolyte solution (0.1 mol L^{-1} NaOH) into the BIA system was stirred using a 12 V micro DC- motor [133]. All amperometric data were presented after baseline correction using NOVA 1.11 software.

4.3 Results and Discussion

4.3.1 Characterization

Initially, the $Ni(OH)_2$ was prepared by the chemical precipitation method [130] and was characterized by Raman spectroscopy, powder X ray diffraction (**Figure 4**) and scanning electron microscope (**Figure 5**). As can be seen in **Figure 4A**, Raman spectra showed the characteristic bands for α-$Ni(OH)_2$ at 990-1046, 1297, 3587 and 3664 cm^{-1}. In addition, bands at 445 and 3587 cm^{-1} are commonly found for β-$Ni(OH)_2$ particles, which were also observed on Raman spectra [130,134]. The wavenumbers around 445 and 3587 cm^{-1} are associated to stretching vibration of Ni-O(H) and O-H, respectively, which can be present in the α -$Ni(OH)_2$ material [134,135]. On the other hand, bands at 990-1046 cm^{-1} are assigned to second-order lattice mode transitions found in α-$Ni(OH)_2$. The wavenumber at 3587 cm^{-1} corresponds to the O-H stretching vibration in α and β phase [130,134,135]. Moreover, the powder XRD pattern for the sample highlights the phase mixture for nickel hydroxide α-$Ni(OH)_2$ and β-$Ni(OH)_2$ [130,134], as can be seen in **Figure 4B**. SEM image (**Figure 5**) shows that the morphology of $Ni(OH)_2$ particles is relatively uniform with sizes between 0.5 and 7.0 µm.

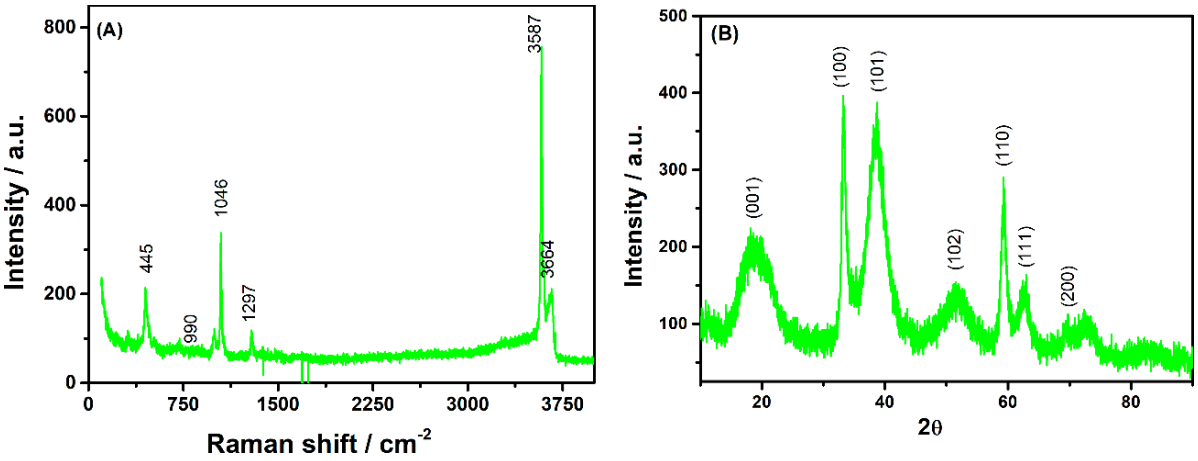

Figure 4. **(A)** Raman spectra and **(B)** powder X ray diffraction pattern for the synthetized nickel hydroxide ($Ni(OH)_2$) particles.

In the next step, the thermal decomposition of all studied materials (PLA, G-PLA, Ni-G-PLA and $Ni(OH)_2$) was investigated by TGA in order to understand the thermal stability and the printability of the designed filament (**Figure 6A**).

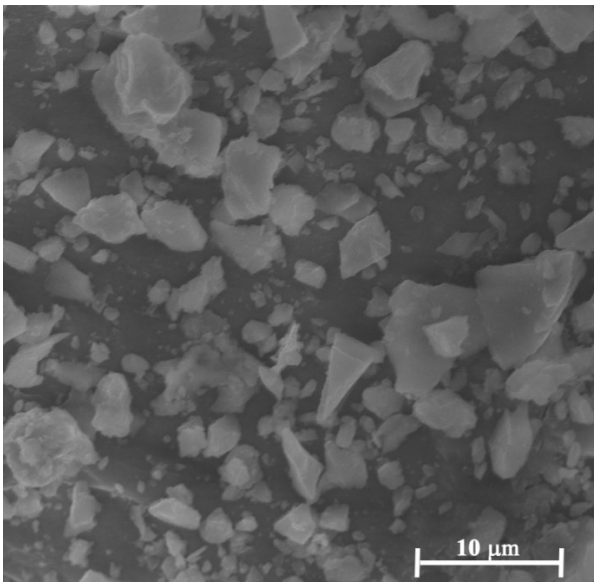

Figure 5. SEM images of $Ni(OH)_2$ particles.

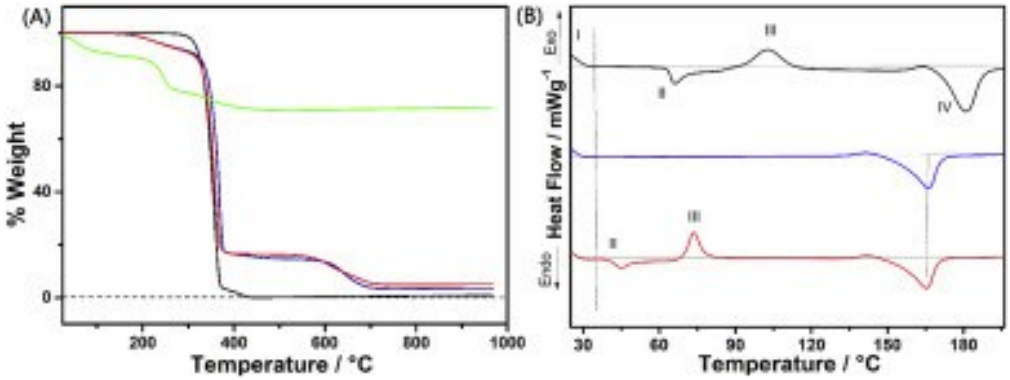

Figure 6. Physicochemical characterization of PLA (black line), G-PLA filament (blue line), Ni-G-PLA filament (red line) and $Ni(OH)_2$ (green line). **(A)** TGA, and **(B)** DSC.

The weight loss for PLA started around 300 ºC and corresponds to the decomposition of the PLA. The main products generated are carbon dioxide, carbon monoxide, and further cyclic oligomers up to nine monomer unit [136–138]. **Figure 6A** shows that the addition of conductive material presents a slight improvement of the thermal stability, once the maximum degradation temperature shift to higher values. According to the literature, the presence of conductive materials in polymeric matrix improves heat conduction, and consequently its thermal stability [138]. The TGA data of the Ni-G-PLA filament shows a thermal decomposition profile (around at 250 ºC) similar to the observed for G-PLA. The filament modified with $Ni(OH)_2$ does not decompose

before 250 ºC, consequently, a printing temperature of 220 ºC is adequate to print the electrodes.

The DSC curves are shown in **Figure 6B** and reveal the thermal properties of the studied materials such as melting and decomposition temperatures. Two endothermic processes were observed in the DSC curve of PLA. These peaks represent the glass transition (peak II, around at 66 ºC) and melting (peak IV, 181ºC) temperature process of PLA matrix and they are characteristic for semi crystalline polymers [136]. As can be seen in **Figure 6B** and **Table 5**, DSC analysis of these materials showed a decrease in the melting temperature (T_m) when comparing the pure PLA (181 °C) with the filaments obtained by processing the PLA mixture with graphene and nickel hydroxide (~166 °C). This difference of the melting temperature values indicates that the PLA processing causes a failure of the bonding energies between the polymer molecules. In addition, the temperature of crystallization (III) of the PLA phase observed at 103 C disappears after the addition of graphene, and this can be due to the high efficient nucleating effect of these material for the PLA [136,139]. The nickel hydroxide probably does not have a good interaction with the functional groups of PLA as graphene which difficult the package of the polymer chains and, consequently, a significant reduction in crystallization temperature is observed.

Table 5. DSC analysis of PLA and G-PLA and Ni-G-PLA filaments.

Sample	T_G / °C	T_C / °C	T_M/°C	ΔH_C/ J g^{-1}	ΔH_M / J g^{-1}
PLA	66	103	181	41.8	67.3
G-PLA	54	-	166	-	62.8
Ni-G-PLA	45	74	166	27.2	59.7

The Raman spectra of the G-PLA and Ni-G-PLA are presented in **Figure 7**. In these spectra it is possible to observe the D (1349 cm^{-1}), G (1571 cm^{-1}) and 2D (2686 cm^{-1}) vibrational bands. The D and G vibrational bands indicate the presence of defects, such as sp^3 hybridization, vacancies, edges sites and heteroatoms. The G band is associated to the presence of sp^2 carbon and the 2D signal is related to two-dimensional order in the graphene plane. The Raman analysis displayed no differences between G-PLA and Ni-G-PLA filament spectra. This effect can be explained by the fact that nickel hydroxide, being denser, remains occluded within the filament, while the surface will accommodate

lighter materials such as graphite during the extrusion process, regardless of the mode of filament modification with the catalyst load. However, the 2D band intensity for Ni-G-PLA is lower than that obtained for G-PLA filament in the Raman spectrum, which can be explained by the destruction of the regular layered structure of graphene, as observed by other authors in the formation of composites containing nickel and graphene [140–142].

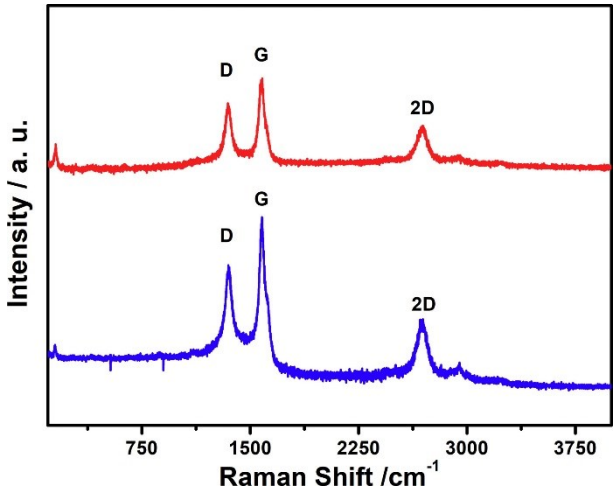

Figure 7. Raman spectra of G-PLA (blue line) and Ni-G-PLA (red line) filaments.

The G-PLA and Ni-G-PLA filaments were also analyzed by X-ray Fluorescence (XRF) to verify the incorporation of Ni in the polymer matrix. As can be seen in **Table 6**, the relative values of the inorganic composition (Ti: 60.82%; Fe: 24.52%; Ag: 8.23%, Cl: 3.92%, Ni: 1.01%; Cr: 1.59% and Mn: 0.93%) showed that Ti and Fe are the most abundant elements found in the G-PLA filament while Ag, Cl, Ni, Cr and Mn were detected in minor amounts. Those results are in agreement with the literature which also reported the presence of metallic impurities in commercial G-PLA filaments [143]. On the other hand, after the synthesis of the proposed filament, there is a significant increase in the amount of Ni (Ti: 39.21%; Fe: 13.78%; Ag: 3.82%, Cl: 3.42%, Ni: 39.35% and Cr: 0.41%) indicating that there was the incorporation of $Ni(OH)_2$ particles within the PLA matrix.

Table 6. XRF analysis of G-PLA and Ni-G-PLA filaments.

Element	G-PLA	Ni-G-PLA
	Composition / wt.%	
Ti	60.82	39.21
Fe	24.52	13.78
Ag	8.23	3.82
Cl	3.92	3.42
Ni	1.01	39.35
Cr	1.59	0.41
Mn	0.93	-

The G-PLA (**Figure 8A**) and Ni-G-PLA (**Figure 8B**) filaments were also examined by SEM. Both images show non-uniform surfaces as expected for thermoplastic composites. However, a crystalline material embedded within the surface is only visible in **Figure 8B**, which confirms the presence of Ni microparticles within this composite.

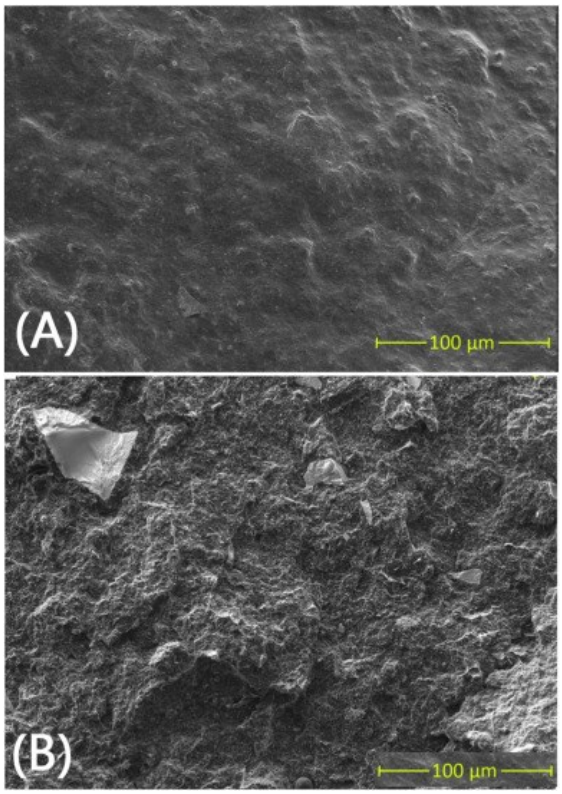

Figure 8. SEM images of **(A)** G-PLA and **(B)** Ni-G-PLA filaments.

4.3.2 Electrochemical measurements

The new filament (Ni-G-PLA) was created with the aim to develop of a non-enzymatic sensor for the selective determination of glucose. First, the electrochemical behavior of the 3D-printed sensor was studied in 0.1 mol L^{-1} NaOH using cyclic voltammetry according to procedures previously reported for nickel electrodes [111,119,127,129,144,145]. The redox peaks observed in **Figure 9** are related to the oxidation of Ni (II) to nickel oxyhydroxide (NiOOH) at around +0.55 V (*vs* Ag|AgCl|$KCl_{(sat.)}$), followed by a reduction peak at +0.37 V (*vs* Ag|AgCl|$KCl_{(sat.)}$), related to the reduction of NiOOH to $Ni(OH)_2$, according to the following reaction [116,122]:

$$Ni(OH)_2 + OH^- \rightarrow NiOOH + H_2O + e^-$$

The electrochemical response of the 3D-printed Ni-G-PLA electrode was relatively poor as can be seen in the inset of **Figure 9** (black line) due to the high amount of non-conductive PLA present in the composition of the 3D-printed electrodes. Therefore, studies were carried out in order to improve the electrochemical performance of the 3D-printed Ni-G-PLA electrode. Among the activation procedures proposed in the literature [58,76,90,106], better results were obtained after simultaneous chemical (PLA saponification) and electrochemical activation (+1.4 V *vs* Ag|AgCl|$KCl_{(sat.)}$ for 200 s followed by -1.0 V *vs* Ag|AgCl|$KCl_{(sat.)}$ for 200 s) in alkaline media (0.5 mol L^{-1} NaOH solution) [9]. This treatment was performed on the Ni-G-PLA electrode surface and a great improvement (36-fold increase in the anodic peak current) in the electrochemical response of this sensor was observed, as can be seen in **Figure 9** (red line). Hence, the nickel catalyst was more exposed once the PLA protective layer material was partially removed.

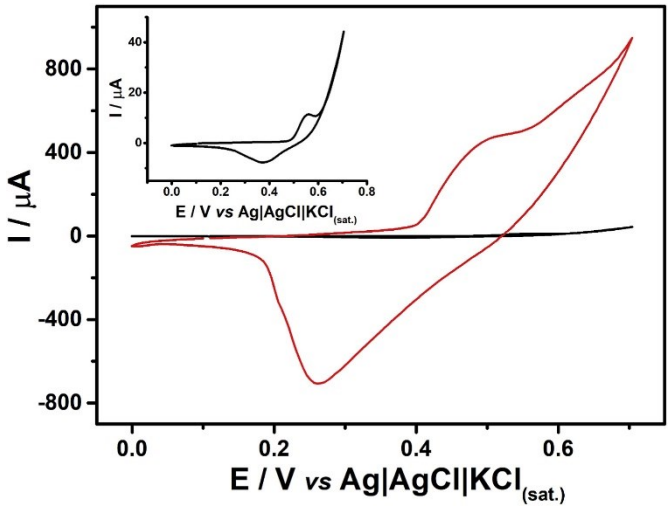

Figure 9. Cyclic voltammograms obtained with the 3D-printed Ni-G-PLA electrode in 0.1 mol L^{-1} NaOH solution before (black line) and after electrochemical treatment (red line). The inset figure shows the amplification of the cyclic voltammogram obtained with the 3D-printed Ni-G-PLA electrode without electrochemical treatment. Scan rate: 50 mV s^{-1}; step potential: 5 mV.

Glucose is electrochemically inactive on carbon-based electrodes, consequently, no electrochemical response was observed with the 3D-printed electrode composed by a mix of PLA and graphene, as shown in the inset of **Figure 10** (blue line). Some alternative platforms are available in the literature for the electrochemical detection of glucose, such as the use of electrodes modified with the enzyme glucose oxidase [80,108,146], electrodes based on the use of different metals such as platinum, gold, nickel, copper or even alloys containing one or a mix of these metals [147]. The operation of enzyme-modified electrodes is dependent on a number of factors, such as temperature, pH, and humidity [111,112], as well as to the use of laborious steps for immobilization of the enzyme on the electrode surface (adsorption, cross-linking, entrapment or electropolymerization) [112,128,146]. In this context, the Ni-G-PLA electrode is a promising material for non-enzymatic determination of glucose since nickel hydroxide (II) acts as a catalyst on the glucose oxidation to gluconolactone [118], as can be seen in the following equation:

$$NiOOH + glucose \rightarrow Ni(OH)_2 + gluconolactone$$

Thus, cyclic voltammograms performed in presence of glucose (**Figure 10**; red line) showed a considerable increase in anodic peak current, due to the electrochemical

reaction mechanism described above. In addition, a small decrease in the cathodic current peak was observed as a result of consumption of NiOOH by glucose as reported in literature [148].

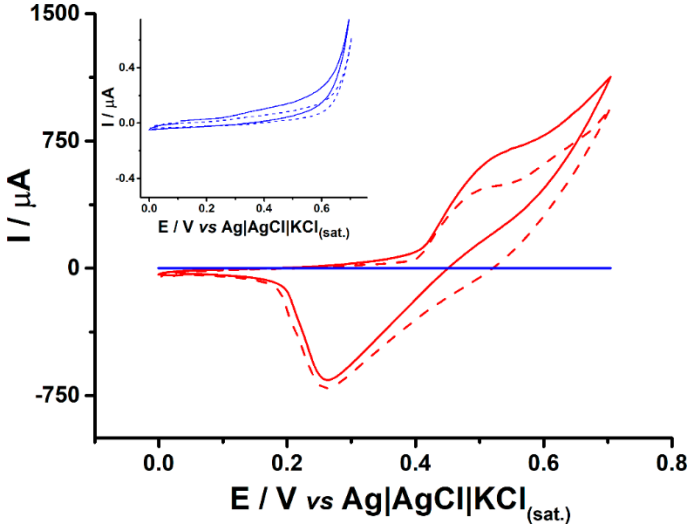

Figure 10. Cyclic voltammograms obtained for a solution containing 1 mmol L^{-1} GLU at G-PLA (blue line) and at Ni-G-PLA (red line) electrochemically treated electrode. The dashed lines refer to the blank solutions scans for both electrodes. The Inset figure shows the ampliation the lower y-axis. Scan rate: 50 mV s^{-1}; step potential: 5 mV.

After that, the BIA system with amperometric detection was used to demonstrate the applicability of the proposed Ni-G-PLA 3D-printed electrode for the rapid and selective detection of glucose. Experimental parameters (applied potential, injection volume and dispensing rate) were evaluated in order to obtain the best analytical sensitivity, high analytical throughput and adequate reproducibility in the analysis procedure. The use of a stirring system was required to avoid the enlargement of peaks and to provide faster reestablishment of baseline current after injection of solutions containing glucose or interfering species in the BIA system.

Figure 11 shows the amperometric responses obtained for triplicate injection of 100 µmol L^{-1} glucose as a function of applied potentials (+0.3 to +0.7 V *vs* Ag|AgCl|$KCl_{(sat.)}$). According to **Figure 11**, the glucose oxidation occurred in potentials higher than +0.4 V (*vs* Ag|AgCl|$KCl_{(sat.)}$) since NiOOH formation is required for glucose detection. Based on this experiment, +0.6 V (*vs* Ag|AgCl|$KCl_{(sat.)}$) was selected for subsequent analysis due to obtaining satisfactory current values and lower standard deviation. At +0.7 V (*vs* Ag|AgCl|$KCl_{(sat.)}$), higher current values were detected, however,

the long-term repeatability was affected. The effect of the other two BIA parameters is shown in **Figure 12A** (injection volume) and **Figure 12B** (dispensing rate). No significant improvement in peak current values was observed if injected volumes or dispensing rates higher than 200 µL (**Figure 12A**) and 213 µL s^{-1} (**Figure 12B**) were used, respectively. Therefore, these values were selected in further amperometric experiments.

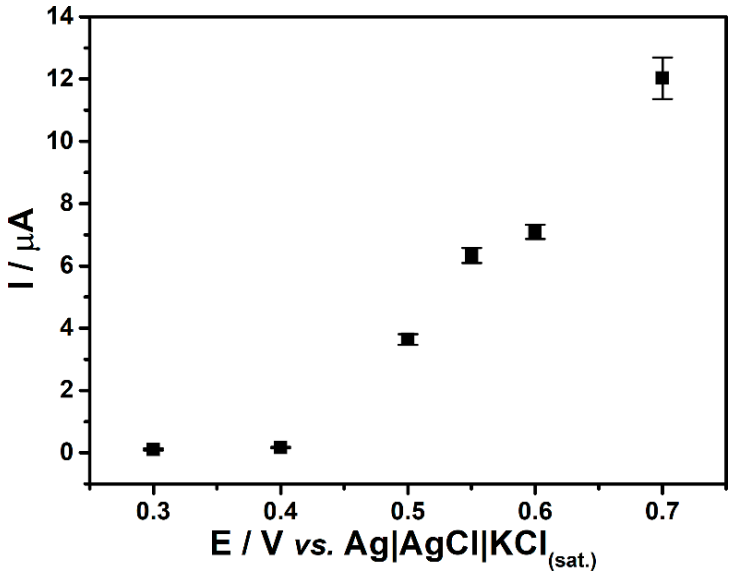

Figure 11. Hydrodynamic voltammograms obtained with the BIA system by plotting the peak current values as function of the corresponding applied potential using the electrochemically treated Ni-G-PLA material as the working electrode. GLU concentration: 100 µmol L^{-1}; supporting electrolyte: 0.1 mol L^{-1} NaOH; dispensing rate: 153 µLs^{-1}; injection volume: 150 µL.

Figure 13A shows the calibration curves for glucose using both non-treated (Δ) and electrochemically treated (□) Ni-G-PLA electrodes. The amperometric responses obtained at +0.6 V for injection of glucose concentrations (75 to 1000 µmol L^{-1}) in ascending and descending order using the electrochemical treated 3D-printed Ni-G-PLA electrode are shown in **Figure 13B**. The analytical characteristics (linear ranges, limits of detection, correlation coefficients, slopes, and intercepts) calculated from data of **Figure 13A** are listed in **Table 7**. The limits of detection were calculated based on IUPAC definition (3σ/s), where σ is the standard deviation of baseline noise and s is the analytical sensitivity of the calibration curve (slope).

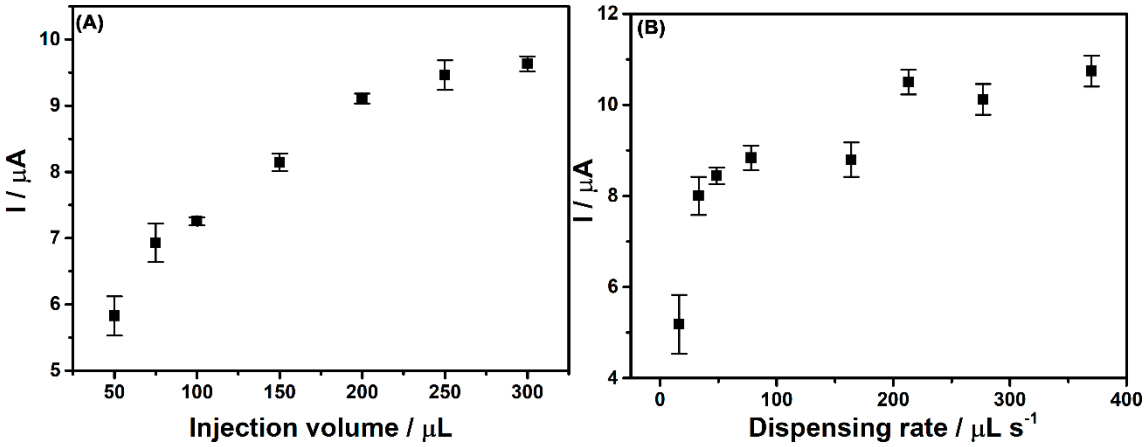

Figure 12. Effect of injection volume **(A)** and dispensing rate **(B)** on the amperometric response of the electrochemically treated Ni-G-PLA electrode for the injection of 100 μmol L^{-1} GLU in the BIA system. Applied potential +0.6 V; supporting electrolyte: 0.1 mol L^{-1} NaOH; dispensing rate in (A): 153 μL s^{-1}; injection volume in (B): 200 μL.

As can be seen in **Table 7** and **Figure 13A**, a higher sensitivity (slope) is achieved using the electrochemically treated 3D-printed Ni-G-PLA electrode (8-fold higher), consequently, lower LOD values were obtained with this electrode. These results are in agreement with SEM images and cyclic voltammograms which presented the higher amount of the catalyst nickel hydroxide (II) exposed after the treatment providing higher electrochemical response. The slopes of the curves indicated the absence of memory effects, since the ascending and descending slope values were similar. According to the literature, glucose can be found in a range of concentrations from 2.0 to 20.0 mmol L^{-1} in human blood serum [125] and from 0.02 to 0.20 mmol L^{-1} in saliva [124] for non-diabetic people. Thus, the LOD (2.4 μmol L^{-1}) obtained for the new proposed non-enzymatic sensor is useful for detection of glucose in these types of samples.

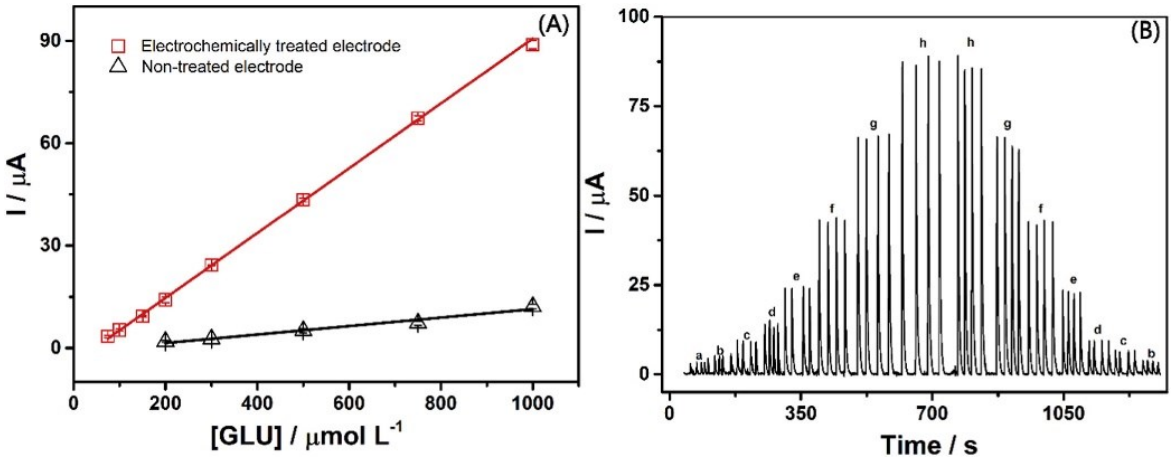

Figure 13. (A) Comparison between calibration curves of glucose obtained with non-treated (**Δ**; black line) and electrochemically treated (□; red line) 3D-printed Ni-G-PLA electrodes. **(B)** Baseline corrected BIA amperograms for glucose injections (n = 4) in concentrations of (a) 75; (b) 100; (c) 150; (d) 200; (e) 300; (f) 500; (g) 750 and (h) 1000 µmol L^{-1}, using Ni-G-PLA electrochemically treated electrode. Supporting electrolyte: 0.1 mol L^{-1} NaOH; applied potential: +0.6 V; dispensing rate: 213 µL s^{-1}; injection volume: 200 µL.

The precision was estimated based on the RSD value of the current peak for 500 µmol L^{-1} glucose (also in **Table 7**). The low RSD values (< 5%) indicated a high precision for the 3D-printed Ni-G-PLA electrode surface. The interelectrode precision was also calculated based on the RSD value of current peaks for 500 µmol L^{-1} glucose obtained on four different electrochemically treated electrodes. The RSD value obtained was 8.9%, indicating a high reproducibility of the construction process of the 3D-printed electrode.

Table 7. Comparison between analytical parameters obtained for both 3D-printed Ni-G-PLA electrodes (without and with electrochemical treatment) for BIA amperometric detection of glucose.

Analytical Parameters	Non-treated electrode	Electrochemically treated electrode
Linear range/µmol L^{-1}	200–1000	75–1000
r	0.987*/0.981**	0.999*/0.998**
Intercept/ µA	−0.991*/-3.144**	−4.317*/-7.589**
Slope/μmol^{-1} L µA	0.012*/0.015**	0.095*/0.096**
LOD/µmol L^{-1}	36.4	2.4
RSD (n = 10; 500 µmol L^{-1})/ %	3.7	2.2

Injection in *ascending and **descending order of concentration.

Usually, electroactive species such as ascorbic acid (AA), uric acid (UA) and urea (UR) can be found with glucose in real samples (blood serum, urine, saliva) as interfering species. According to the literature, the normal physiological level of glucose is several times higher than the concentration of interfering species [111,120,129,149]. **Figure 14A** shows BIA amperometric responses obtained for successive injections (n = 4) of the following solutions: 1.0 mmol L^{-1} glucose (GLU); 0.1 mmol L^{-1} ascorbic acid (AA); 0.1 mmol L^{-1} uric acid (UA); 0.1 mmol L^{-1} urea (UR); and multicomponent solution (MS) containing all previous compounds. As shown in **Figure 14B**, no significant influence (<10%) was observed when the response obtained for the solution with only glucose was compared to the multicomponent solution (with all compounds). These results indicated that the proposed 3D-printed Ni-G-PLA electrode has adequate sensitivity for glucose detection in biological samples.

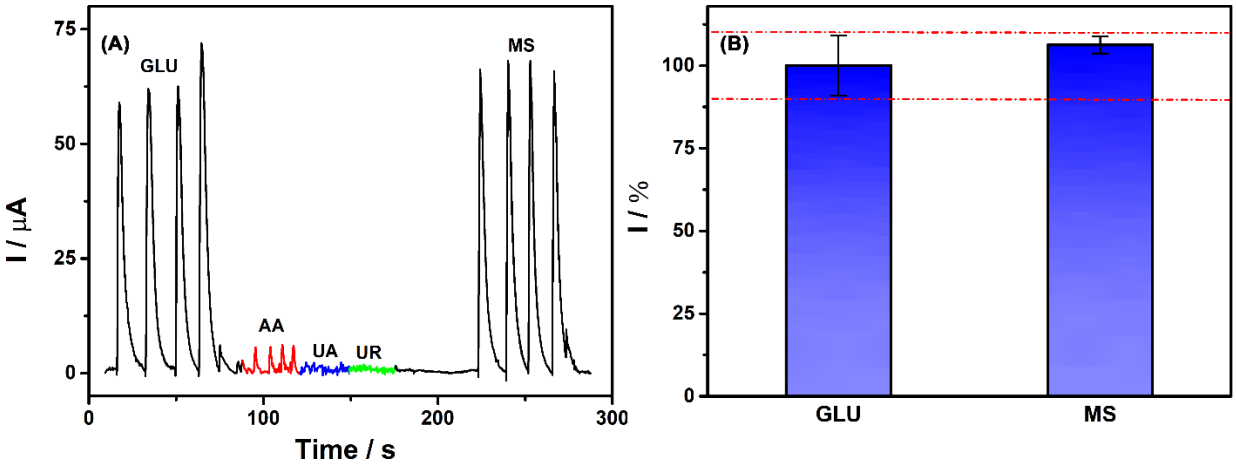

Figure 14. (A) Amperometric response obtained for 1 mmol L^{-1} glucose (GLU), 0.1 mmol L^{-1} ascorbic acid (AA), 0.1 mmol L^{-1} uric acid (UA) and 0.1 mmol L^{-1} urea (UR) and a multicomponent solution (MS) containing all compounds (1 mmol L^{-1} GLU and 0.1 mmol L^{-1} of AA, UA, and UR; **(B)** Effect of the presence of concomitant interfering species at the GLU peak current. Working electrode: electrochemically treated 3D-printed Ni-G-PLA; supporting electrolyte: 0.1 mol L^{-1} NaOH; applied potential: +0.6 V; dispensing rate: 213 μL s^{-1}; injection volume: 200 μL.

4.4 Conclusions

The production, characterization (physicochemical, spectroscopic, and electrochemical) and analytical application of a new conductive thermoplastic filament composed by PLA, graphene, and Ni microparticles was firstly reported. We showed here that disposable modified electrodes can be produced using a simple additive manufacturing 3D printer. The new conductive filament was used for fast production of 3D-printed electrodes for non-enzymatic glucose detection using a portable electrochemical system. The obtained results showed that Ni-G-PLA is a promising material for fast production of disposable sensors for electrochemical detection of glucose.

5 Annex 2. Electrochemical synthesis of Prussian blue from iron impurities in 3D-printed graphene electrodes: Amperometric sensing platform for hydrogen peroxide.

5.1 Introduction

Additive manufacturing (3D printing) technologies have been extensively applied in chemistry with relevant applications in material science, electrochemistry and analytical chemistry [97,150–152]. The fused deposition modelling (FDM) is the most inexpensive 3D-printing technique and has become popular in the fabrication of electrochemical sensors [21,97]. Commercially-available conductive filaments for FDM 3D-printers have contributed to the rapid development of this technique in the field of electrochemistry and the most common material is the PLA-based filament containing graphene [75,76,91,106,108].

Nevertheless, recent publications by Browne and coauthors have reported the presence of metallic impurities (Fe, Ti and Al) in commercial filaments of graphene/PLA, such as Black Magic®. These impurities affect the electrochemical properties of the 3D-printed material, such as for water splitting [143,153]. Previous investigations have demonstrated that residual metallic impurities in graphene and carbon nanotubes affect the electrochemistry of several processes [154–158]. Iron impurities have been commonly reported to affect the electrochemical oxidation and reduction of different analytes [155,157,158].

In this context, taking the advantage of the presence of iron impurities in 3D-printed graphene/PLA electrode obtained from commercially available filaments, we propose the electrochemical synthesis of iron hexacyanoferrate (Prussian blue) films by cyclic voltammetry in the presence of ferricyanide. It is well known that Prussian blue (PB) films can be formed electrochemically in the presence of iron (III) cations and ferricyanide [159]. In our approach, the iron (III) source is provided by the bulky 3D-printed G/PLA electrode, after electrode immersion in a solvent to remove the excess of PLA and expose iron sites. A PB-modified electrode is also known as an artificial peroxidase due to its electrocatalytic properties towards the reduction of H_2O_2, which is relevant for biosensing, food and security analysis [159–163]. To demonstrate the potential application of PB-3D printed modified electrode, the amperometric detection of

hydrogen peroxide under flow conditions provided by batch-injection analysis (BIA) is presented. BIA is a powerful technique, especially when allied to amperometric detection, due to its precision, rapidness, and portability [164].

5.2 Experimental

5.2.1 Reagents and materials

All solutions were prepared with deionized water (Millipore Direct-Q3, Bedford MA USA) with a resistivity no less than 18 Ω cm. All reagents were of analytical grade and used without further purification. Potassium ferricyanide ($K_3[Fe(CN)_6]$) purchased from Proquimios (Rio de Janeiro, Brazil). Chloride and phosphoric acids and potassium chloride were obtained from Synth (Diadema, Brazil) and hydrogen peroxide aqueous solution (30% wt.) from Dinamica (São Paulo, Brazil). Sodium hydroxide was obtained from AppliChem Panreac (Barcelona, Spain) and dimethylformamide (DMF) from Merck (Rio de Janeiro, Brazil). Conductive PLA filaments containing graphene (G/PLA) was purchased from Black Magic 3D with volume resistivity of 0.6 Ω cm (New York, USA).

5.2.2 Instrumentation

All electrochemical measurements were performed using an μ-Autolab type III potentiostat/galvanostat controlled by NOVA 1.11 software, which was responsible for the acquisition of data. A lab-made miniaturized $Ag|AgCl|KCl_{(sat)}$ [132], and a platinum wire were used as reference and counter electrodes, respectively.

All electrochemical experiments were performed using a 10 mL container or a 100mL batch-injection cell manufactured by FDM 3D-printing using an ABS filament as reported in the literature [90]. Along with the BIA cell, an electronic micropipette Eppendorf (Multipette® stream) was also used to perform reproductive injections at controlled dispensing rate and volume. A distance of 2 mm between the working electrode and the micropipette was kept constant as the best condition defined in previous works using BIA [165].

5.2.3 Manufacturing of the 3D-printed electrode

Hollow cubes (1 cm x 1 cm) with wall thickness of 0.72 mm were printed using an open-source Graber i3 RepRap 3D printer and a graphene doped PLA filament

(G/PLA). All printing was performed using a 0.5 mm hot end nozzle with an extrusion temperature of 220 ºC and heated bed temperature at 70 ºC. Before electrochemical deposition of PB films on electrode surface, the sides of the hollow cubes were polished with abrasive paper (1200 Grit) wetted with an ultrapure water for 30 s. After that, a piece of planar substrate was immersed in DMF for 30 min as proposed by Kalinke et al. [107]. The G/PLA electrode was then washed with ethanol and deionized water dried at room temperature for 24h and finally was coupled to the 3D-printed BIA cell.

5.2.4 Preparation of PB films on the 3D-printed electrode

PB films were electrodeposited following a procedure adapted from the literature [166]. Two hundred voltammetric cycles were carried out in presence of 1 mmol L^{-1} potassium ferricyanide, using 0.1 mol L^{-1} KCl acidified with 0.01 mol L^{-1} HCl over -0.3 to +1.2 V (*vs.* Ag|AgCl|$KCl_{(sat).}$) at room temperature and scan rate of 50 mV s^{-1}. In next step, the modified electrode (PB/G/PLA) was washed with ultrapure water several times. Thus, the electrode was used in the amperometric experiments.

5.2.5 Amperometric detection of H_2O_2 using a BIA cell

Amperometric detection of H_2O_2 was performed in a BIA cell under the application of a constant potential of 0.0 V (*vs.* Ag|AgCl|$KCl_{(sat.)}$) using a 0.1 mol L^{-1} phosphate buffer solution (pH 7.4) containing 0.1 mol L^{-1} KCl as supporting electrolyte as previously described in literature [167].

In this system, successive injections of increasing concentrations of H_2O_2 were performed directly at the electrode surface (wall-jet configuration). A volume and dispensing rate of 100 µL and 277 µL s^{-1} was selected, respectively, as proposed the literature [167]. The reference and counter electrodes were positioned at the top of the BIA cell, and the 3D-printed working electrode was placed at the bottom of the BIA cell using a rubber O-ring in order to prevent leaks and define the geometric area of the electrode (ID = 0.54 cm; area = 0.22 cm^2).

5.3 Results and discussion

The presence of iron in commercial graphene/PLA filaments was reported previously in the literature [143,153] and in this work we confirmed the presence of iron impurities at the 3D-printed graphene/PLA electrode by XRF analysis (**Table 6**, Annex I). Aiming to verify if these iron impurities are accessible to produce PB films, **Figure 15** shows cyclic voltammetric experiments in the presence of ferricyanide using a 3D-printed G/PLA electrode (A) before (as printed) and (B) after solvent immersion. The black line in both plots shows the profile of the redox probe ferricyanide on the 3D-printed electrode before and after solvent-treatment. As expected, the voltammetric profile improved as verified by the reduction of the ΔEp value from 300 to 150 mV and the substantial increase in current intensity. As long as the cyclic voltammetric scans were performed, it is possible to observe the formation of PB films on the solvent-treated 3D-printed electrode. The processes involved are described in **Figure 16**.

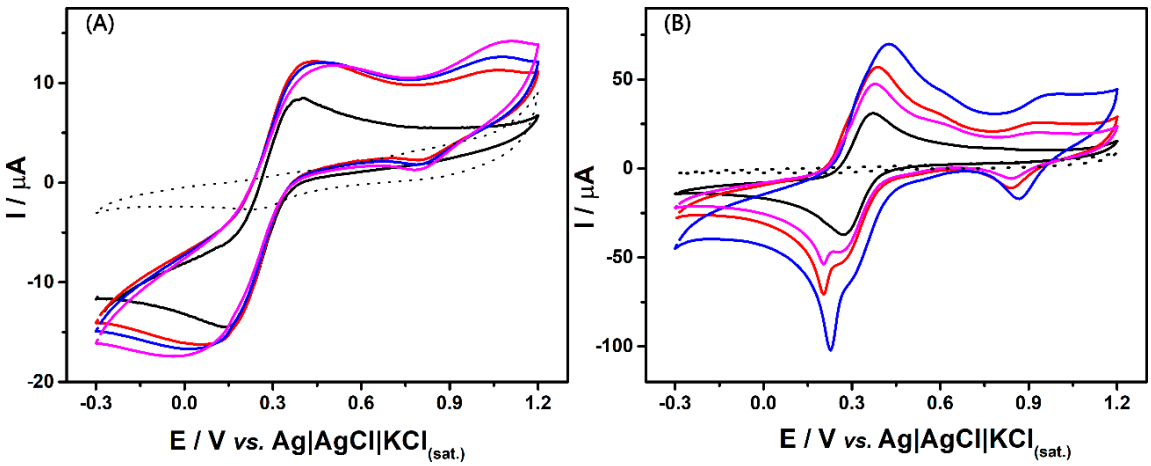

Figure 15. Cyclic voltammograms obtained at G/PLA electrode before (A) and after (B) DMF treatment to electrochemically synthetize PB films in the presence of 1 mmol L^{-1} ferricyanide in a 0.1 mol L^{-1} KCl + 0.01 mol L-1 HCl solution. 1st (black line), 50th (pink line), 100th (red line) and 200th (blue line) cycles are presented. Scan rate: 50 mV s^{-1}; step potential: 5 mV. The dotted line refers the blank of analysis (before PB films formation on electrode).

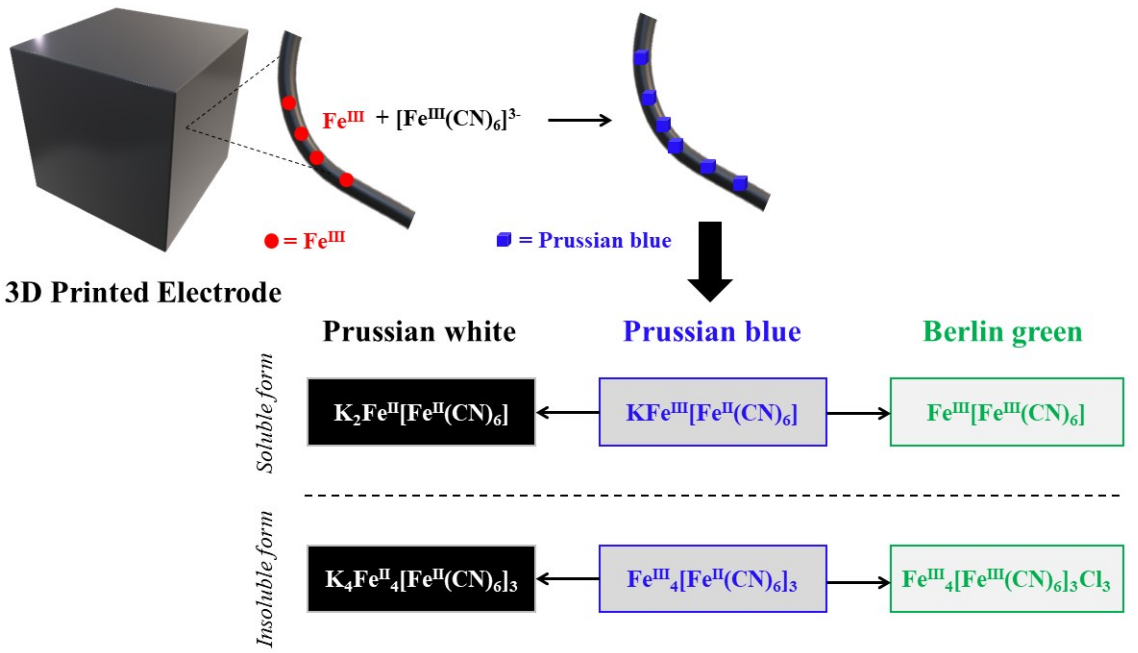

Figure 16. Illustrative scheme of the Prussian blue formation on the surface of the 3D-printed electrode.

The first process, occurring as a shoulder on the peak at +0.45 V (**Figure 15B**) and the corresponding reduction peak at −0.20 V, corresponds to the Prussian blue/Prussian white pair. The second pair (Berlin green/Prussian blue) occurs at around +0.9 V (oxidation and reduction peaks of **Figure 15B**). The same process does not occur so efficiently on the untreated electrode (**Figure 15A**), probably due to the lower amount of Fe(III) available in the bulky 3D-printed electrode.

Figure 17 shows the cyclic voltammograms of the 3D-printed G/PLA electrodes after modification with PB before and after surface treatment of the G/PLA electrode. These experiments were performed in the presence of the same supporting electrolyte used to grow the PB films. The black line shows the PB-modified surface using a 3D-printed electrode not treated by immersion in DMF after 200 cycles in the presence of ferricyanide. The typical profile of a PB-modified surface is not well defined (inset of **Figure 17**) likely due to the low amount of Fe(III) available (confirmed in **Figure 15A**). After solvent treatment, the expected profile of a PB-modified appears (pink, red, green and blue lines corresponding to the PB formation after 50, 100, 150 and 200 cycles, respectively). The increase in the number of scans from 50 to 200 cycles affects the formation of PB as verified by the substantial current increase of the processes of PB. The

peaks I and IV at +0.2 V correspond to the Prussian blue/Prussian white pair while the peaks II and III at +0.9 V to the Berlin green/Prussian blue pair, as presented in Scheme in **Figure 16**, and in agreement with data reported in the literature [159–162].

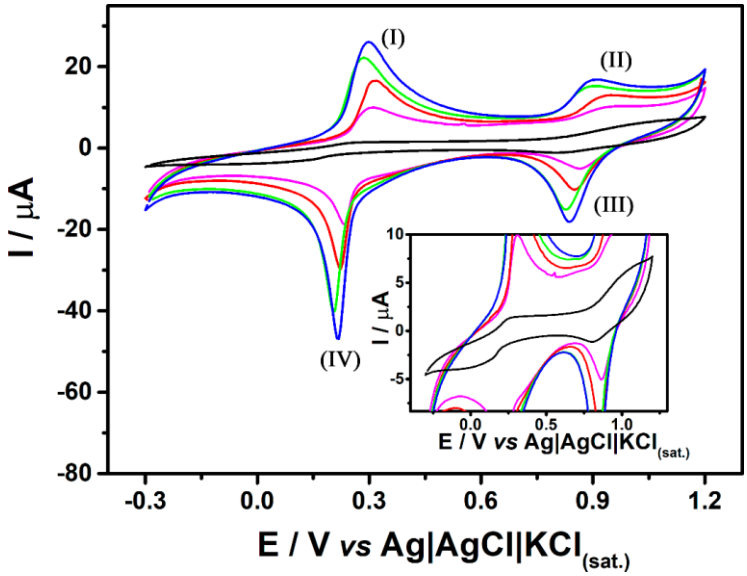

Figure 17. Cyclic voltammograms in electrolyte of 3D-printed G/PLA electrodes after modification with PB: Black line: untreated electrode and PB formation after 200 cycles; DMF-treated and PB formation after 50 (pink line); 100 (red line); 150 (green line) and (b blue line) 200 cycles. Scan rate: 50 mV s^{-1}; Step potential: 5 mV; Electrolyte: 0.1 mol L^{-1} KCl + 0.01 mol L^{-1} HCl.

The Raman spectra of 3D-printed electrode before and after the modification with PB are presented in **Figure 18**. The vibrational D (1356 cm^{-1}) and G (1585 cm^{-1}) bands are associated to the presence of defects, such as sp^3 hybridization, vacancies, edges and heteroatoms. Moreover, the G band is assigned to the presence of sp^2 carbon and the 2D signal is related to two-dimensional order in the graphene plane [167]. After the formation of PB, a characteristic band at 2150 cm^{-1} of iron hexacyanoferrate was observed, attributed to ν (CN) stretching vibration [77].

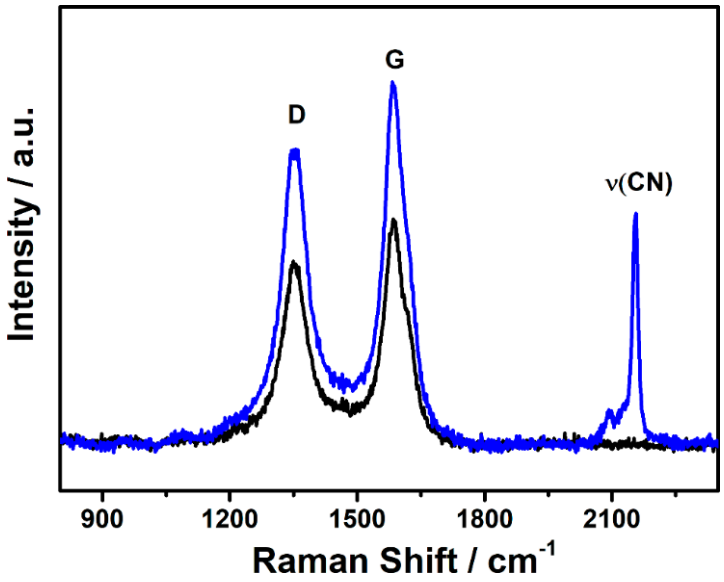

Figure 18. Raman spectra of the 3D-printed electrode before (black line) and modified with PB (blue line).

The inter-electrode reproducibility of PB modification was estimated based on the RSD values of the Prussian blue/Prussian white pair (peaks I and IV identified in **Figure 17**) obtained from three different electrodes, as this redox pair is responsible for the selective detection of H_2O_2. The low RSD values (6.5 and 11.3% for the peaks I and IV, respectively) indicated an acceptable reproducibility of the complete protocol to the formation of PB films on the 3D-printed G/PLA electrode surface using iron impurities. The 3D-printed G/PLA surface treated by DMF and modified with PB films (200 cycles) was evaluated for the amperometric determination of H_2O_2 using the BIA system taking advantage of the electrocatalytic action of the Prussian blue/Prussian white pair towards the electrochemical reduction of H_2O_2. **Figure 19A** shows the amperometric response of the PB/G/PLA modified electrode obtained at +0.0 V for injections (100 µL each) of H_2O_2 (from 1 to 1000 µmol L^{-1}) under a controlled injection rate of 277 µL s^{-1}. **Figure 19B** shows the corresponding analytical curve obtained by plotting current response as function of H_2O_2 concentration. A linear range between 1 and 700 µmolL^{-1} was obtained (equation of the curve in **Figure 19B**: i(µA) = –0.081 (±0.001) –0.0126 (±0.0009) × [H_2O_2] ; r = 0.999) and the limit of detection (LOD) was 0.56 µmol L^{-1} (LOD = 3 x SD_{blank}/slope). This result shows that the PB/G/PLA electrode presents a low LOD value comparable to previous PB-modified electrodes, in which the PB modification was performed by electrochemical synthesis from a mixture of iron(III) and ferricyanide in

KCl or where PB microparticles were incorporated into graphite composite electrodes [77,162]. The combination of the sensor with BIA enables precise and fast determinations (around 180 injection per hour), which is relevant for routine analysis. The modified electrode was stable during the continuous monitoring of H_2O_2 under flow conditions which indicates stability of the PB film synthetized through iron impurities in 3D-printed G/PLA electrodes. It is also important to mention that the electrode worked at 0.0 V for the H_2O_2 sensing which is a detection condition free from interference of several species found at biological, food, environmental samples.

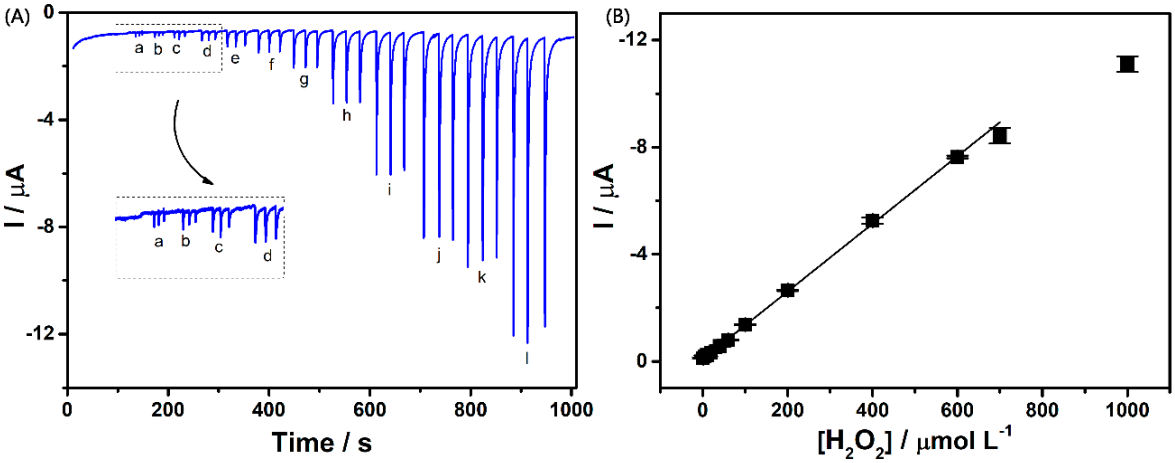

Figure 19. (A) Amperometric responses and **(B)** respective analytical curve for triplicate injections of H_2O_2 in increasing concentrations: 1 (a), 5 (b), 10 (c), 20 (d), 40 (e), 60 (f), 100 (g), 200 (h), 400 (i), 600 (j), 700 (k) and 1000 µmol L^{-1} (l) using a BIA cell containing 0.1 mol L^{-1} PBS (pH 7.4) + 0.1 mol L^{-1} KCl as supporting electrolyte. Working electrode: 3D-printed G/PLA DMF-treated and PB-modified after 200 cycles. Working potential: 0.0 V; Injected volume: 100 µL; Injection rate: 277 µL s^{-1}.

To demonstrate the applicability of the proposed 3D-printed PB/G/PLA electrode in the BIA cell, milk samples were analyzed. **Figure 20** shows the amperometric recording for triplicate injections of a milk sample just 10-fold diluted in the supporting electrolyte. To evaluate possible sample matrix, a recovery test was performed by the analysis of spiked milk sample with two known concentrations of H_2O_2 (50 and 100 µmol L^{-1}). Recovery values were between 94 and 101% (

Table 8), which indicates the absence of sample matrix in the electrochemical

Sample	Found / µmol L-1	Spiked / µmol L-1	Recovery / µmol L--1	Recovery / %
Milk	7.6±0.2	50	53.9±0.2	93±0.3
		100	108.5±2.3	101±2

detection of H_2O_2. Certainly, the low-potential detection (0.0 V *vs.* Ag|AgCl|$KCl_{(sat.)}$) of H_2O_2 only possible due to the electrocatalytic action of the PB films enabled the selective determination of the analyte free from the interference of sample matrix, even after a 10-fold dilution of a sample containing a complex matrix.

Table 9 lists several PB-based electrochemical sensors developed for H_2O_2 determination [77,159,175–178,166,168–174], highlighting the supporting electrolyte and pH solution, applied potential for its selective detection and detection limits. The proposed 3D-printed PB/G/PLA electrode easily obtained from iron impurities of G/PLA filaments shows one of the lowest values of limit of detection ever reported, with a wide linear concentration range. Most of the previous reported electrodes were designed using carbon nanotubes or graphene, as they provide increase in surface area and conductivity, combined to PB due to its electrocatalytic properties towards H_2O_2 detection. However, most of the procedures used for electrode modification involves many laborious steps and thus are time-consuming, which is not the case of the proposed 3D-printed PB/G/PLA electrode. Moreover, the high sample throughput (180 injection per hour) is an important advantage provided by the BIA system not highlighted in

Table 9 for routine analyses.

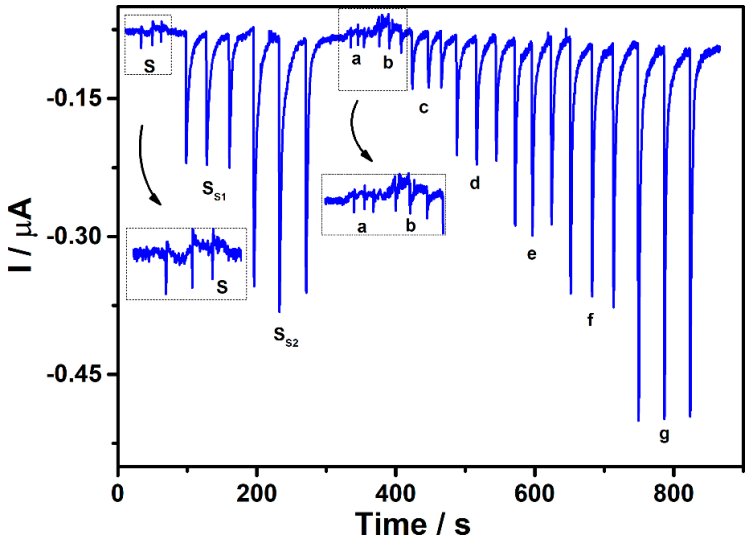

Figure 20. BIA amperograms obtained from injections of milk pure samples (S) and respective additions of 50 µmol L^{-1} (S_{s1}) and 100 µmol L^{-1} (S_{s2}) of H_2O_2. Injections of standard solutions of H_2O_2 (a-g) in a range of 1-150 µmol L^{-1}. The same conditions of **Figure 19**.

Table 8. Concentrations of H_2O_2 obtained by the BIA system and recovery values for the milk spiked samples (n = 3).

Sample	Found / µmol L^{-1}	Spiked / µmol L^{-1}	Recovery / µmol L^{-1}	Recovery / %
Milk	7.6±0.2	50	53.9±0.2	93±0.3
		100	108.5±2.3	101±2

Table 9. Comparison of the proposed 3D-printed PB/G/PLA electrode with other previous electrochemical sensors developed for H_2O_2 detection.

Electrode	Linear Range / µmol L^{-1}	LOD / µmol L^{-1}	pH	Potential	Ref.
GCE/PB	0.1 – 100	0.10	PBS/KCl 6.0	-0.05 V*	[159]
SPE/PB	0.4-100	0.4	PBS/KCl 7.4	0.0 V*	[177]
Au-CDlectrode/PB	1-1200	0.4	PBS 5.3	-0.1 V*	[176]
CPE/FeCNT/PB	0.5-30	0.02	PBS/KCl 7.3	+0.15 V*	[166]
GCE/PB/rGO	0.05-120	0.004	PBS/KCl 7.0	+0.20 V*	[175]
GCE/PB-G	10–1440	3	PBS/KCl 6.0	0.0 V*	[174]
GCE/GO/PB	5-1200	0.12	PBS/KCl 6.0	+0.10 V**	[173]
FTO/PB	90-350	36.0	HCl/KCl	-0.10 V *	[172]
3D-G/PB	2-112	0.44	PBS/KCl 7.4	-0.15 V	[77]
PB-GNPs/BG/GC	9.16-143000	3.2	HCl/KCl	-0.05V*	[171]
NPS-PB/ BDD	0.1-1000	NR	PBS 6.0	0.0 V*	[170]
ITO/Fe-Ni-PB	200-5000000	NR	Basic aqueous solution 8.0	NR	[169]
RGO/MWCNT/PB	50-1000	8.7	BR/KCl 4.0	-0.05 V*	[168]
PB/G/PLA	1-700	0.56	PBS/KCl 7.4	0.0 V*	This work

Electrodes: GCE – Glassy carbon electrodes; SPE - Screen Printed electrode based on carbon paste; Au-CDlectrode – Gold CD electrode; CPE/FeCNT – Carbon paste electrode containing carbon nanotubes and Fe; rGO – Reduced graphene oxide; PB-G – Graphene containing nanoparticles of PB; GO – graphene oxide; FTO- F-doped tin oxide; 3D-G – 3D-printed graphene electrode; GNPs/BG/GC – Gold nanoparticles in glassy carbon electrodes modified with a bucky gel; NPS-PB/ BDD – Nanoparticles of Prussian blue in boron doped diamond electrode; ITO/ Fe-Ni-PB – Indium tin oxide modified with Ni, Fe and Prussian Blue. RGO/MWCNT/PB- reduced graphene oxide, carbon nanotubes, and Prussian blue transparent chemically synthetized. E / V *vs.* *Ag|AgCl|$KCl_{(sat.)}$ and ** *vs.* SCE.

5.4 Conclusion

We have demonstrated that iron impurities within 3D-printed G/PLA electrodes can be accessed after solvent treatment to electrochemically generate PB films (iron(III) hexacyanoferrate) using ferricyanide in a KCl/HCl medium. The stability of the obtained PB/G/PLA electrode was assessed by the continuous amperometric monitoring of H_2O_2 using a BIA system. The sensor responds to H_2O_2 within a wide concentration range reaching a submicromolar detection limit. This investigation shows that the iron impurities in the G/PLA filament can be used as a benefit in the fabrication of highly selective amperometric sensors, which can be extended for the production of novel iron-based sensors.

6 Annex 3. Printing parameters affect the electrochemical performance of 3D-Printed carbon electrodes obtained by fused deposition modeling.

6.1 Introduction

Additive manufacturing (AM) has emerged as an important tool in electrochemistry field for the development of sensors, energy-storage devices, and general accessories [21,51,60]. One of the most used techniques for the fabrication of 3D-printed objects is fused deposition modeling (FDM) due to its simplicity, low cost, versatility, and ability to produce complex three-dimensional and multi-material structures [52,60,179]. In FDM process, a thermoplastic polymer is heated to a temperature that is slightly above the melting point and extruded through a metallic nozzle and deposited layer-by-layer on a platform. The 3D printer movement is computer-controlled along three directions (XYZ axes). When the deposition of the first layer is completed, the second layer is assembled over the first layer. This process continues until the part-manufacturing is concluded [9, 10].

Some composites containing thermoplastic and conductive particles have been used in additive manufacturing in numerous applications [104,182–186]. The most affordable commercial conductive filament used for the production of electrochemical devices is composed of a mix of carbon black (CB) and polylactic acid (PLA) [9,55,187–190]. However, some studies have shown that this material in its native form has high charge transfer resistance and, to overcome this problem, many research groups have explored surface treatment/ activation procedures of 3D-printed electrodes to improve their conductivity and performance as electrochemical sensors. The papers published employed mechanical [91], electrochemical [9,55,76,106], physical [81], solvents[75,89], and biological [80] treatments or use of chemical modifiers on the surface [77] to increase its electrochemical activity. Although these procedures improve the performance of 3D printed sensors, most of them require multiple steps (time-consuming) or the use of additional equipment and/or even use toxic organic solvents [7,8,11–15]. In addition, these works did not explore how 3D printing parameters affect the electrochemical performance or/and did not present the parameters used in their studies.

The selection of suitable parameters can be a feasible alternative to improve the response of electrodes produced by FDM 3D printing [3,16–21]. These parameters that affect the quality of 3D printing processes can be divided into two groups: machine and printing parameters. Nozzle diameter, bed and extruder temperatures are considered machine parameters while printed orientation (vertical or horizontal), layer thickness, printed perimeter or shell count, print speed, and fill density are called of printing parameters. These parameters are chosen in the slicing stage of the project using specialized software compatible with the 3D printer [191]. Generally, some print settings (bed and extruder temperatures and extruder multiplier) were recommended by the manufacturer [187].

Patel's group printed cone-shaped CB/PLA electrodes and has shown that the printed orientation of the object can affect the electrochemical response of some analytes when 3D-printed sensors were used [7,23]. According to the authors, vertically printed electrodes provided the greatest faradaic current response when compared to the horizontally printed electrodes. In addition, layer thickness has been reported as another important factor that introduces significant variations in the electrochemical response (charge transfer resistance and faradaic current) of the sensors [192]. However, to best our knowledge, detailed investigations on the effect of printing parameters on the charge transfer resistance of 3D-printed electrodes have been rarely evaluated [191–193].

Herein, we studied the influence of printing parameters (print orientation, layer thickness, perimeter count and print speed) on the electrochemical performance (peak-to-peak separation, faradaic current peak intensity, charge transfer resistance and electrochemically active surface area) of FDM 3D-printed CB/PLA electrodes. Electrochemical characterizations were performed by cyclic voltammetry (CV) and electrochemical impedance spectroscopy (EIS). Moreover, the differences in the structure integrity in terms of CB and PLA distribution over the electrode surface for the different printing parameters was investigated by Raman spectroscopy and multivariate curve resolution by alternating least squares (MCR-ALS) to extract the fundamental vibrational characteristics within the data. Our results showed that printing parameters noticeably influence the electrochemical activity (active surface area and faradaic peak current) of FDM 3D-printed sensors due to the direct influence on the conductivity and distribution of CB particles over PLA matrix in the electrodes surface.

6.2 Experimental

6.2.1 Manufacture of 3D-printed carbon black/polylactic acid (CB/PLA) electrodes

A rectangular piece (30 mm length, 11 mm width, and 1.2 mm thickness) was printed using a commercial filament composed by CB/PLA (Protopasta, WA, USA) and a Flashforge Dreamer NX printer (São José dos Campos, São Paulo, Brazil) with a direct drive extruder equipped with a 0.4 mm nozzle at 220 ºC and a bed temperature of 70 ºC. The electrodes were printed with 100% infill density and extrusion multiplier was set up to 1.1 (constant value), varying the perimeter (1 to 2 shells), layer thicknesses (0.05 to 0.30 mm), printing perimeters speed (30 to 120 mm s^{-1}) and orientation (horizontal and vertical). These ranges were selected based on mechanical limitation of 3D-printer used in this study. Printing parameters performed outside the capabilities of the printer provide uncertain and non-reproducible results.

Finally, the 3D-printed CB/PLA electrodes (without any treatment before analysis) were placed at the bottom of a 3D-printed electrochemical cell fabricated according to Cardoso *et al.* [90]. Briefly, the electrochemical cell (cylindrical shape; internal volume = 10 mL) was produced using acrylonitrile butadiene styrene (ABS) filament purchased from GTMax 3D (São Paulo, Brazil). A schematic image of the electrochemical cell is shown in **Figure 21**. This cell is composed by a (a) cell body; (b) top cover containing two orifices to introduce both (c) counter and (d) reference ($Ag|AgCl|KCl_{(sat.)}$ - ALS Co, Ltd, Japan) electrodes; (e) bottom cover with three holes for the insertion of (f) screws and nuts. The geometric electrode area (0.18 cm^2) was limited by a rubber O-ring allocated over the working electrode (3D-printed CB/PLA in rectangular planar shape).

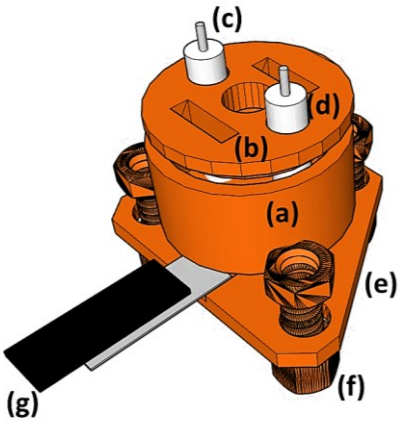

Figure 21. Schematic representation of 3D-printed cell used in the experiments. This cell is composed by: (a) cell body (internal volume = 10 mL); (b) top cover containing two orifices to introduce of both (c) counter and (d) reference electrodes; (e) bottom cover with three holes for the insertion of (f) screws and nuts; and (g) the 3D-printed CB/PLA electrode in rectangular planar shape (geometric area of 0.18 cm^2 limited by a rubber O-ring).

6.2.2 Electrochemical measurements

CV (without IR-drop compensation) and EIS measurements, controlled by NOVA 2.1.4 software, were carried out using a PGSTAT 128N potentiostat/galvanostat (Metrohm Autolab, Utrecht, Netherlands). Electrochemical characterizations of the 3D-printed electrodes were performed in the presence of 10 mmol L^{-1} hexaaminеruthenium chloride (III) (Sigma Aldrich, Steinheim, Germany) and 0.1 mol L^{-1} potassium chloride (Carlo Erba, São Paulo, Brazil) as electrochemical probe and supporting electrolyte, respectively.

EIS measurements were accomplished from 100 kHz to 0.01 Hz with amplitude of 10 mV in the presence of 10 mmol L^{-1} $[Ru(NH_3)_6]^{2+/3+-}$, using 0.1 mol L^{-1} KCl as the supporting electrolyte. The Randles equivalent circuit was applied to fit the experimental data to acquire the charge transfer resistance (Rct) between the working 3D-printed electrode surface and the probe dissolved in the supporting electrolyte.

The electrochemically active surface area of 3D-printed CB/PLA electrodes were estimated by CV experiments at different scan rates (10 to 150 mV s^{-1}), according to the Randles-Sevcik equation [194,195] (**Eq. 1**), where I_p is the faradaic peak current, A is the electrochemically active surface area (cm^2), C is the concentration of the redox probe

(mol cm^{-3}), *D* is diffusion coefficient (cm^2 s^{-1}), *v* is the scan rate (V s^{-1}) and *n* is the number of electrons transferred (n=1, for $[Ru(NH_3)_6]^{2+/3+}$ probe). All electrochemical experiments were performed at room temperature and in the presence of dissolved oxygen.

$$Ip = 2.69x10^5\ ACD^{1/2}n^{3/2}v^{1/2} \qquad \textbf{(Eq. 1)}$$

The electrochemical data (peak-to-peak separation, faradaic cathodic current, and electroactive area) obtained for each of the evaluated printing parameters were statistically compared using the student t-tests at 95% confidence level.

6.2.3 Raman measurements

3D-printed CB/PLA electrodes were analyzed through Raman scattering measurements. Raman scattering measurements were performed in different points within a mapped area (surface scanning mappings) in each sample using a 785 nm excitation source with a 1 s acquisition time in a Horiba Xplora spectrometer in a microscopy setup. Firstly, the sample was illuminated with a 10-fold amplification objective, and the radiation power was adjusted to 6 mW (the diameter of spot associate to the laser beam is *ca.* 2 mm^2) aiming at preventing sample decomposition, which was confirmed by no time-dependent changes in the acquired spectra and optical microscopy images. For the dispersion of scattered radiation wavelengths, it was used a diffraction grating of 400 g mm^{-1}, which allows the acquisition of the Raman spectrum in the range of ca. 3000 cm^{-1} in a single measurement.

6.2.3.1 Data Analysis

The acquisition of large range Raman spectra allows the application of multivariate techniques for the investigation of the sample overall behavior. Herein, it was employed multivariate curve resolution by alternating least squares (MCR-ALS) to extract the fundamental vibrational characteristics within the data. The general idea behind MCR-ALS is the description of the data matrix (*D*) as a linear combination of pure spectra (described in the rows of matrix S^T), according to **Eq. 2** [195,196]:

$$D=CS^T+E \qquad \textbf{(Eq. 2)}$$

Where *E* is the matrix of residuals, and the *C* is the matrix contains the weights of each pure spectra in the description of the experimental data. The *C* matrix, therefore, contains information of the surface distribution of different types of spectral signatures in

a mapping measurement. MCR-ALS analyses were performed using the *R* language using the Alsace package [197,198]. The solution to **Eq. 2** is obtained in a least-squares algorithm after an initial estimate of pure components in *S*. Such estimation was performed via an orthogonal projection analysis (OPA) algorithm, where spectra of maximum dissimilarity are considered as initial pure components input [199].Thus, the number of components was selected to reduce the lack of fit (**Eq. 2**), which was generally observed to be below 5% for two components.

6.3 Results and Discussion

6.3.1 Electrochemical characterization of 3D-printed electrode by varying of printing parameters

The printing perimeter speed is an important parameter that influences the surface quality of 3D printed objects. **Figure 22** shows an optical image of 3D-printed CB/PLA electrodes using two printing speeds (30 and 120 mm s^{-1}) to better illustrate the final aspect of the objects. Higher resolution was achieved when lower printing speed was used. **Figure *22*** showed difference in the quality of 3D-printed CB/PLA electrodes.

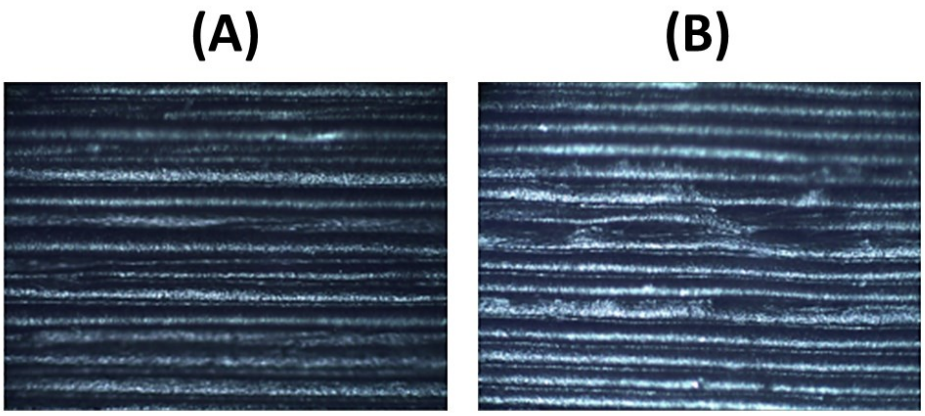

Figure 22. Optical images (10x objective lens) of 3D-printed electrode surfaces at low (A: 30 mm s^{-1}) and higher (B: 120 mm s^{-1}) printing speed. Printing parameters: 0.05 mm layer thickness, 2 shell and 100% infill density.

As can be observed, a more uniform and reproducible surface is obtained when the lowest speed was used. In this case, the influence of the printing perimeter speed (30-120 mm s^{-1}) in the electrochemical response (faradaic current and peak-to-peak

separation) of the 3D-printed CB/PLA electrodes using 10 mmol L^{-1} $[Ru(NH_3)_6]^{2+/3+}$ as redox probe was investigated (**Figure 23A**).

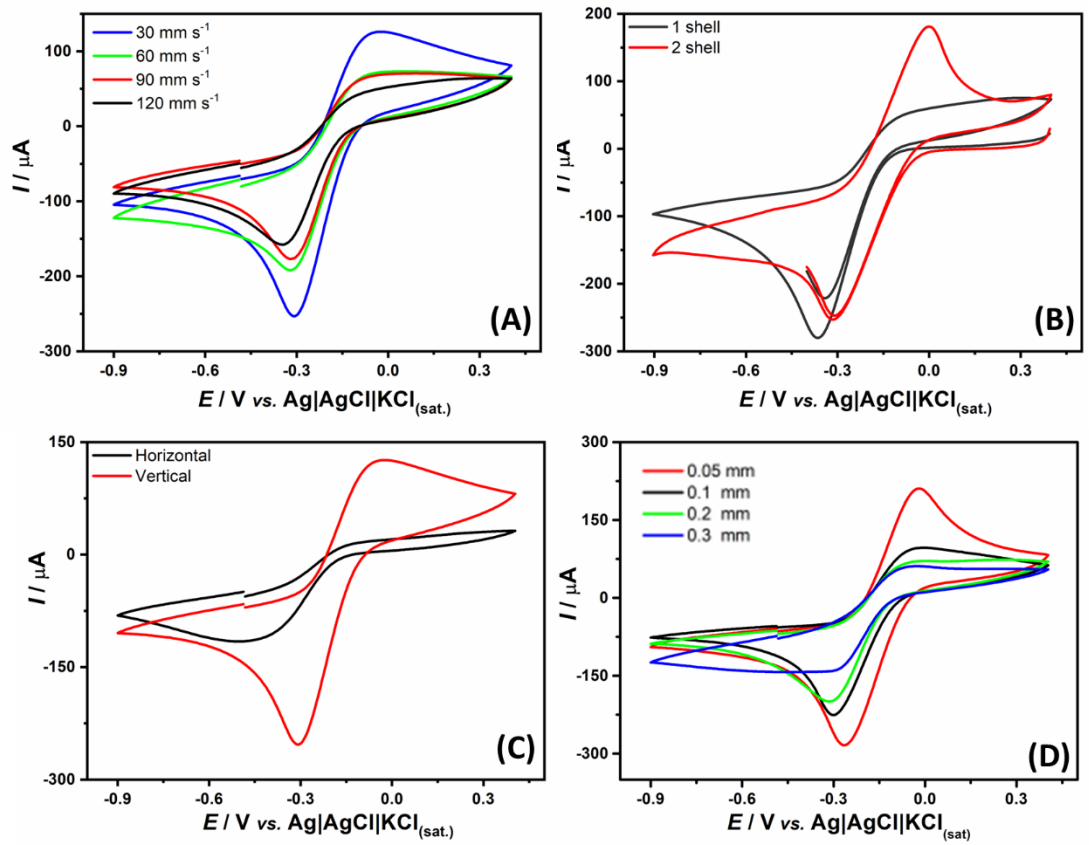

Figure 23. CV profiles for 10 mmol L^{-1} hexaammineruthenium chloride (III) in the presence of 0.1 mol L^{-1} KCl concerning variations in the following 3D-printing: **(A)** printing perimeter speed (30-120 mm s^{-1}); **(B)** perimeter number (1 or 2 shells); **(C)** printing orientation and **(D)** layer thickness (0.05-0.3 mm). CV parameters: scan rate: 50 mV s^{-1}; step potential: 5 mV. Constant printing parameters: vertical orientation, layer thickness: 0.2 mm; printing perimeter speed: 40 mm s^{-1} with 1 shell in vertical orientation. Working electrode: printed rectangular piece without activation.

Table 10 summarizes the faradaic cathodic current (I_{pc}) as well as the peak-to-peak separation (ΔE_p) values obtained for three different working electrodes printed varying parameters (average values ± SD). Printing perimeter speeds lower than 30 mm s^{-1} was also investigated; however, the time required to build the electrode is very high (~6 hours), making the construction of disposable electrodes unfeasible. In addition, minimal improvements were observed with the decrease in the speed.

Table 10. Electrochemical data (peak to peak separation and cathodic peak current) obtained from cyclic voltammograms of 10 mmol L^{-1} $[Ru(NH_3)_6]^{2+/3+}$ using three different working electrodes (n=3) printed using different parameters.

Parameters		ΔEp /mV	Ipc / µA
Orientation	**Vertical**	239 ± 4	181 ± 3
	Horizontal	316 ± 3	43 ± 5
Layer thickness / mm	**0.05**	244 ± 6	241 ± 3
	0.1	251 ± 7	165 ± 4
	0.2	239 ± 4	189 ± 7
	0.3	242 ± 11	116 ± 4
Printing speed / mm s^{-1}	**30**	185 ± 6	210 ± 10
	60	240 ± 3	158 ± 7
	90	236 ± 2	132 ± 3
	120	270 ± 5	144 ± 12
Perimeter number	**1**	241 ± 11	185 ± 6
	2	187 ± 8	210 ± 10

As can be seen, better voltammetric profile and higher faradaic current response were achieved when a lower printing speed value (30 mm s^{-1}) was used (**Table 10**), which differed significantly when compared to 60 ($p<0.005$, n = 3), 90 ($p<0.003$, n = 3) and 120 mm s^{-1} ($p<0.01$, n = 3); respectively. In addition, the peak-to-peak separation (ΔE_p) also decreased considerably with the reduction of the printing speed (ΔE= 270 ± 5 and 185 ± 6 mV for 120 and 30 mm s^{-1} ($p<0.003$, n = 3), respectively). Lower printing speed (e.g., 20 mm s^{-1}) was also evaluated, however, required time to produce each electrode is very high (~6 hours) and the increase in the faradaic current was minimal.

The electrochemically active surface area (*A*) calculated by the Randles-Sevcik method [194,195] displayed a significant decrease for higher printing perimeter speeds (0.072 cm^2 and 0.012 cm^2 for 30 and 120 mm s^{-1} ($p < 0.001$, n = 3), respectively), as can be seen in **Table 11**. The use of the Randles-Sevcik method is indicated for diffusional control redox processes and has limitations for sluggish/irreversible processes (black curves in **Figure 23**), however, the results are useful for the comparisons made here.

Table 11. Electroactive area calculated by Randles-Sevcik method for 3D-printed electrode by varying printing parameters.

Parameters		Electroactive area / cm^2
Orientation	Vertical*	0.072 ± 0.001
	Horizontal	0.032 ± 0.004
Speed / mm s^{-1}	30*	0.072 ± 0.001
	120	0.012 ± 0.002
Layer thickness / mm	0.05*	0.072 ± 0.001
	0.3	0.044 ± 0.002
Perimeter	1	0.023 ± 0.001
	2*	0.072 ± 0.001

*Best condition for printing.

The effect of the printing parameters on the performance of the 3D-printed CB/PLA electrode was also evaluated by EIS (**Figure 24A** and **Table 12**). A notably reduction in Rct values was acquired with the decrease of the printing perimeter speed (632 and 1030 Ω for 30 and 120 mm s^{-1}, respectively). These results agree with those observed by CV and the estimated electrochemically active surface areas. Hence, sensors produced at low printing perimeter speed (30 mm s^{-1}) enhanced electrochemical performance of the 3D-printed sensors.

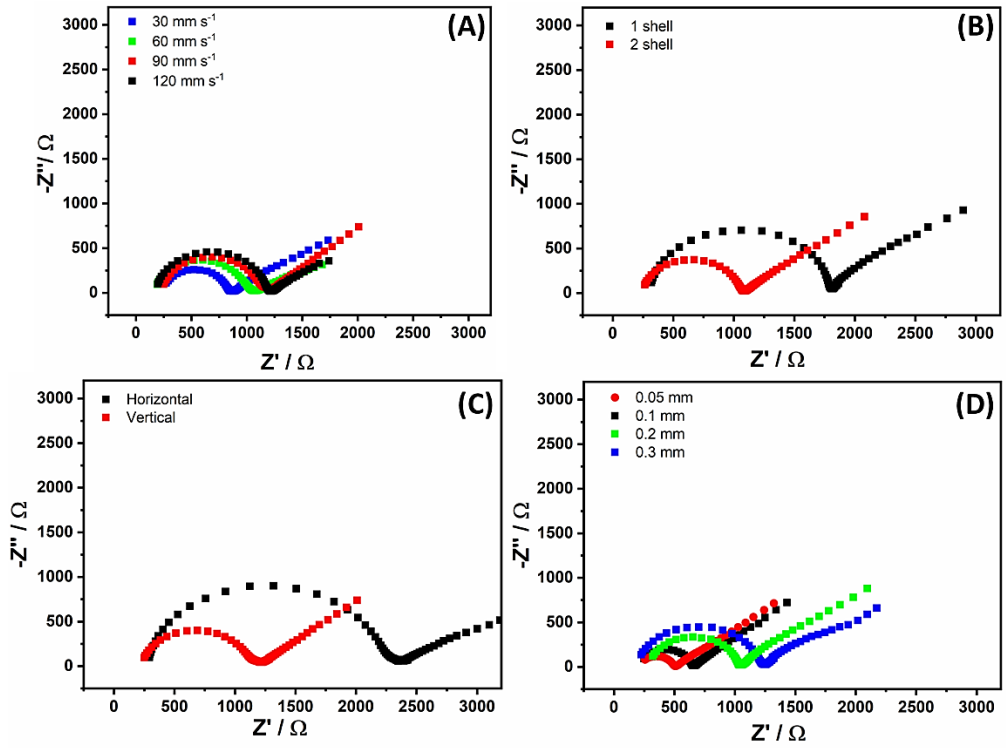

Figure 24. Nyquist plots of impedance spectra at -0.17 V (*vs.* Ag|AgCl|$KCl_{(sat.)}$) in the presence of 10 mmol L^{-1} $[Ru(NH_3)_6]^{2+/3+}$ and 0.1 mol L^{-1} KCl solution varying 3D printing parameters: **(A)** printing perimeter speed (30-120 mm s^{-1}); **(B)** perimeter number (1 or 2 shells); **(C)** printing orientation and **(D)** layer thickness (0.05-0.30 mm). All EIS measurements were performed at a frequency range 100 kHz to 0.01 Hz with amplitude of 10 mV. Working electrode: printed rectangular piece without activation.

Table 12 Resistance charge transfer (Rct) obtained through Nyquist plots for 3D-printed electrodes.

Printing parameters	Conditions	Rct / Ω
Orientation	Vertical	958
	Horizontal	2060
Speed / mm s^{-1}	30	632
	60	899
	90	958
	120	1030
Layer thickness / mm	0.05	298
	0.10	435
	0.20	740
	0.30	1050
Perimeter	1	1490
	2	825

In addition, these results showed that a printing speed study is essential, however, each equipment has its individual limitations, and the optimization of these parameters depends on the printer configuration. Probably, this behavior can be attributed to the position of CB particles in PLA matrix. When the filament is extruded at lower printing perimeter speed, the conductive particles are more ordered and compacted within polymeric structure. On the other hand, when the printing speed increase, CB particles are more scattered and aggregates in the PLA matrix, reducing the electric paths within the composite [27, 36].

To better understand these observations, it is important to mention how 3D printer extruders work at low and high printing speeds. The filament is heated and extruded trough the nozzle, however, the amount of the material depends on the printing speed. At lower printing speed, the printable material stays longer in the heating block, resulting in a better distribution of CB particles within the PLA matrix. On the other hand, the increase in the printing speeds, the filament spends a short period in the heating block and, consequently, the CB particles are more scattered and aggregated in the 3D-printed electrode. Moreover, some works in literature reported that there is formation of voids at

higher printing speed [201,202] that can influence in the electrochemical activity of 3D-printed CB/PLA electrodes.

In the next step, we investigated the effect of the number of perimeters (known as walls and shells) in the electrochemical performance of the 3D-printed CB/PLA sensor. Basically, the number of perimeters controls how many contours the 3D printer makes around the printed object. **Figure 25** shows optical images of the two 3D-printed CB/PLA electrodes with a different number of perimeters (1 and 2 shells) and **Figure 23B** displays CV responses for the evaluated redox probe using 3D-printed CB/PLA sensors printed with two different perimeters (1 and 2 shells).

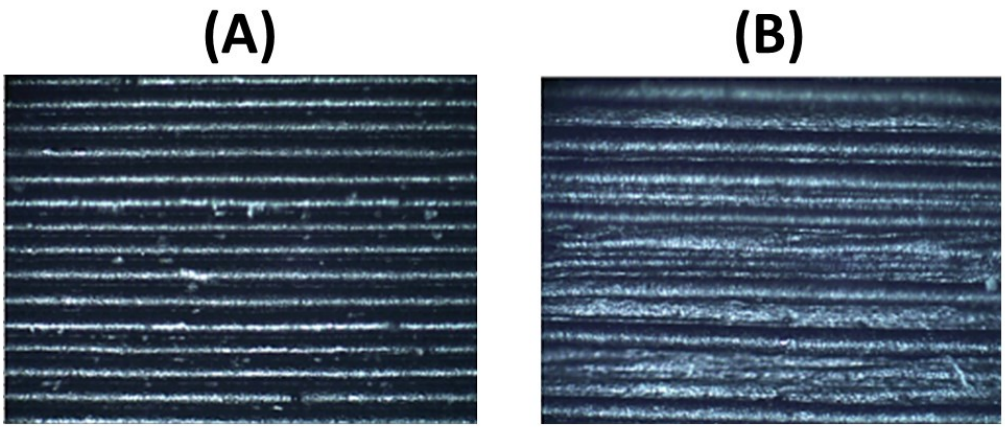

Figure 25. Optical images (10x objective lens) of top-view cross section of 3D printed CB/PLA electrodes, using different number of walls or shells (A: 1; B: 2). Printing parameters: 0.05 mm layer thickness, speed of 30 mm s^{-1} and 100% infill density.

As can be noticed in **Figure 23B**, a significant difference was achieved in the cathodic faradaic peak current ($p < 0.02$, $n = 3$). Moreover, in the anodic region, the sensor printed with 2 shells has a better-defined peak than the sensor with 1 shell. In addition, the calculated electrochemically active surface area for the sensor with 1 shell was significantly lower than the sensor with 2 shells (0.023 cm^2 and 0.072 cm^2 ($p < 0.0006$, $n = 3$), respectively). Similarly, the electrode produced with 2 shells showed a lower Rct value than the electrode with 1 shell (**Figure 24B** and **Table 12**). Probably, in thin-walled printed objects, the final object is composed of concentric contour (outer perimeter) without space for infill, enabling the appearance of pores (structural defects). When the number of perimeters increase (inner perimeter), it is possible to select an appropriate amount of infill [191], improving the strength and water-tightness of the piece. We observed that thin-walled printed electrodes showed problems with leakage or soaking,

which can explain an increase in the Rct value for a sensor with a single perimeter (1 shell). In addition, the use of more shells increases the print time and the consumption of the filament. Thus, we did not investigate electrodes manufacture with more perimeters.

The orientation of the printed layers is also a relevant printing parameter that influences the electrochemical response of some analytes using 3D-printed conductive materials. The filaments were extruded and deposited in vertical (transverse 90°) and horizontal (longitudinal 0°) printing orientations, as seen in **Figure 26**. Moreover, **Figure 23C** shows the influence of this parameter in the voltammetric response of 10 mmol L^{-1} $[Ru(NH_3)_6]^{2+/3+}$. In the vertical orientation, a well-defined voltammetric profile and higher faradaic current were observed in comparison to horizontal orientation ($p < 0.005$, $n = 3$).

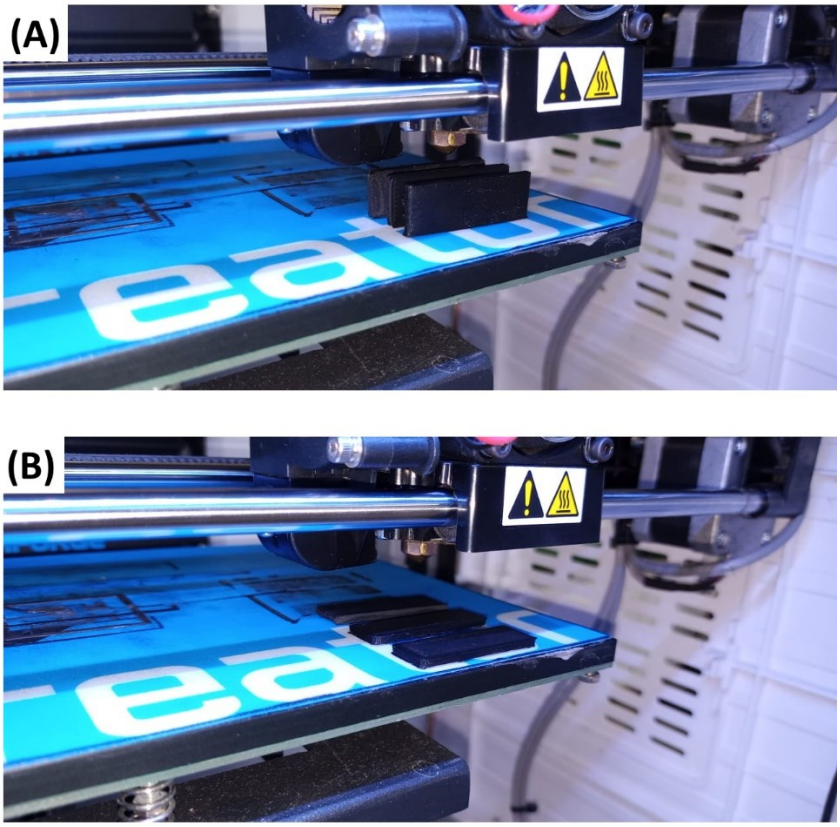

Figure 26. Real images of 3D-printed CB/PLA electrodes printed in (A) vertical and (B) horizontal orientation.

Additionally, the electrode printed in vertical orientation ($\Delta Ep = 239 \pm 4$ mV) showed lower peak-to-peak separation ($p < 0.002$, $n = 3$) if compared to the horizontally printed electrode ($\Delta Ep = 316 \pm 3$ mV) EIS experiments were also used to estimate the Rct

values for both electrodes. As can be seen in the Nyquist plot (**Figure 24C**), there was a significantly decreased in Rct value in vertically printed sensor (Rct = 958 **Ω**) than in the horizontal (Rct = 2060 **Ω**), as observed in **Table 12**, which supports other previously published works. In fact, Patel's group [192,193] observed a reduction in Rct value using vertical orientation when compared to horizontal printed electrodes. Furthermore, the estimated electrochemically active surface area for vertical and horizontal printed electrodes were 0.072 and 0.032 cm^2, respectively, which are statistically different ($p < 0.009$, $n = 3$) indicating more available conductive sites in electrodes printed in vertical orientation (**Table 11**). Probably, the difference observed in the voltammetric behavior between electrodes printed with different orientations is associated with the distribution and/or conductive pathways within the composite material, as described by other previous studies [192,193,200].

The layer thickness is a printing parameter associated with printing resolution, as described by other authors [191,192,203–205]. The quality of surfaces of 3D-printed objects is improved by reducing the layer thickness (smoother surface). This printing parameter is adjusted through a slicer program [41] and corresponds to the exact height of each layer polymer is extruded by a 3D printer. **Figure 27** presents the visual difference between 3D-printed CB/PLA electrodes with different layer thickness (0.05 and 0.30 mm). In addition, Abdalla and collaborators also showed that the layer thickness affects the electrochemical activity. Here, we investigated the influence of layer thickness in our design electrode (rectangular piece) using CV experiments and 10 mmol L^{-1} $[Ru(NH_3)_6]^{2+/3+}$ as the redox couple.

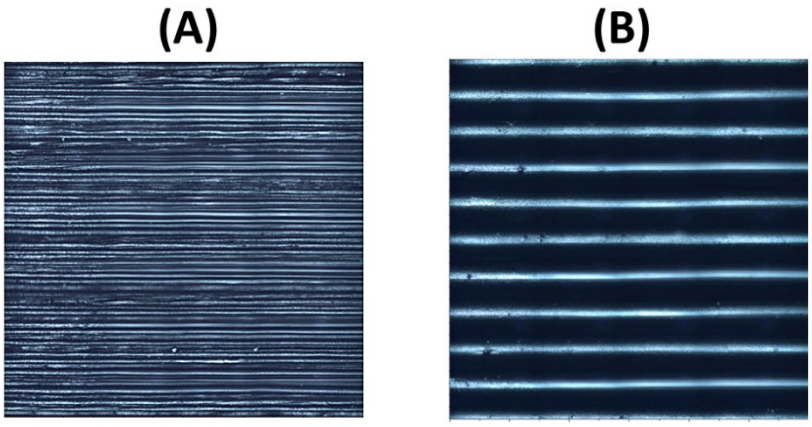

Figure 27. Optical (10x objective lens) images of 3D-printed electrodes in different layer heigh (**A**: 0.05 mm; **B**: 0.30 mm), Printing conditions: 100% infill density, 2 perimeter, speed of 30 mm s^{-1}.

As seen in **Figure 23D**, a better voltammetric profile (well-defined anodic and cathodic peaks) were achieved with electrodes printed with lower layer thickness (0.05 and 0.10 mm) when compared to the use of higher layer thickness (0.20 and 0.30 mm). Additionally, a considerable improvement in the faradaic current (~2-fold) was observed when the electrode was printed with 0.05 mm layer thickness in comparison to the electrode printed with 0.3 mm layer thickness ($p < 0.02$, $n = 3$). Even when comparing the layer thickness of 0.05 with 0.1 mm, noticeable difference in terms of faradaic current ($p < 0.03$, $n = 3$) and peak-to-peak separation ($p < 0.04$, $n = 3$) were obtained. The results obtained through EIS experiments (Nyquist plots, **Figure 24D**) are also in agreement with CV and electrochemically active surface area ($p < 0.0005$, $n = 3$). Lower layer thickness (0.05 mm) provided less Rct values (298 **Ω)** when compared to higher layer thickness (0.30 mm; Rct = 1050 **Ω**). These results can indicate more uniform distribution of conductive materials within the composite when 0.05 mm layer thickness is used. According to Abdalla *et. al* [192], when the filament is extruded, CB particles are more ordered and compacted in thinner layers, making a higher probability for conductive routes. As the layer height increases, the CB particles can be less ordered, resulting in the decrease of conductive pathways [192].

6.3.2 Understanding how the arrangement of CB particles in PLA matrix determines the improvement of electrochemical activity.

As can be seen in **Figure 23** and **Figure 24**, a considerable difference in the electrochemical behavior was observed for the evaluated redox probe with the variation of the printing parameters. In the present section, we investigated if these changes can be associated with the arrangement of CB conductive particles in PLA matrix after printing. For this purpose, Raman measurements were performed in a given area of the electrode, point by point, to construct multivariate curve resolution by alternating least squares (MCR-ALS). Raman scattering is a well-suited technique for studying distribution of carbon-based materials, such as CB, in a matrix. When coupled with macroscopy it can be widely used for spatial distribution of such materials. In this manuscript we performed Raman mapping analyses for spatial characterization of CB in printed electrodes with the aim of correlating such results with the observed differential electrochemical responses. In this analysis, it was possible to map the CB population within the polymeric matrix and its distribution for each type of printing parameter. Raman spectra and mappings of the 3D printed electrodes for the two different printing perimeter speeds (30 and 120 mm s^{-1}) before MCR analysis are shown in **Figure 28**.

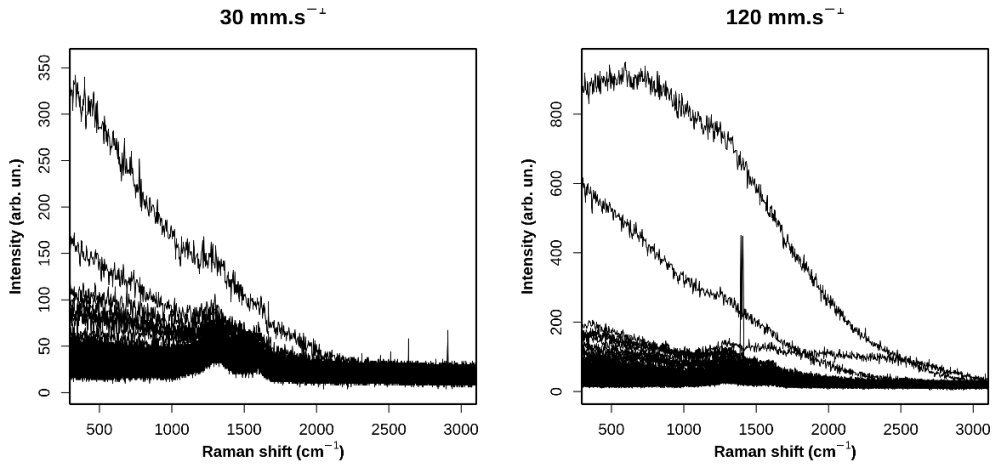

Figure 28. Raman spectra for electrodes fabricated with two different printing speeds (30 and 120 mm s^{-1}).

The Raman spectra in the mappings show bands around 1320 and 1650 cm^{-1} which are respectively assigned to D and G bands of CB [206,207]. Moreover, it can be observed in some spectra of the mapped area an underlying background not commonly associated to CB. Such background could be due to sample decomposition and/or to the presence of

other molecular structures besides CB. Indeed, we could observe sample decomposition upon higher laser intensities through decrease in CB intensities of time. Therefore, the laser power was adjusted until no CB intensity change is observed over time. Therefore, we interpret this background as a Raman feature due to the matrix environment for CB. Since CB is responsible for sample conductivity, we use the observation of clear CB bands as an indicative of its spatial distribution over the sample. Considering the filament composition as being mainly of CB and PLA, such background could be related to the PLA matrix, although it should be clear that the vibrational signatures of PLA are not clearly visible in the spectra. Based on the previous observations, MCR-ALS analyses were performed aiming at separating the CB and matrix contributions to the Raman spectrum. The results after the MCR analysis can be seen in **Figure 29**, where component 1 is to CB and component 2 is associated to the matrix (PLA). **Figure 29A** and **E** show the components 1 and 2 for different speed of printing, indicating the MCR-ALS successful separation of both features. **Figure 29B** and **F** show the optical images for each sample.

For 30 mm s^{-1} parameter (**Figure 29A-D**), it was observed that the mathematical separation between components 1 and 2 was not complete, and it is still possible to notice a little contribution of component 1 (D and G carbon band on the background) in the curve of component 2 (**Figure 29E** – blue line). Otherwise, when analyzing the printing perimeter speed of 120 mm s^{-1} (**Figure 29E–H**), it is possible to observe a better separation between components 1 and 2 (**Figure 29E**), indicating the existence of heterogeneous areas containing more conductive material and areas with PLA as background. The presence of higher areas with background domination (PLA) could indicate a lower material conductivity, affecting the electrochemical performance (faradaic response, peak-to-peak separation, Rct values). These results are in accordance and help to explain the electrochemical data, which shows that the electrode printed with 30 mm s^{-1} presented a better electrochemical response (faradaic current and lower peak-to-peak separation) and higher electrochemically active surface area. Therefore, a faster printing speed would decrease the carbon black exposure, thus, decreasing its activity and electrochemical response (faradaic current, peak-to-peak separation and charge transfer resistance).

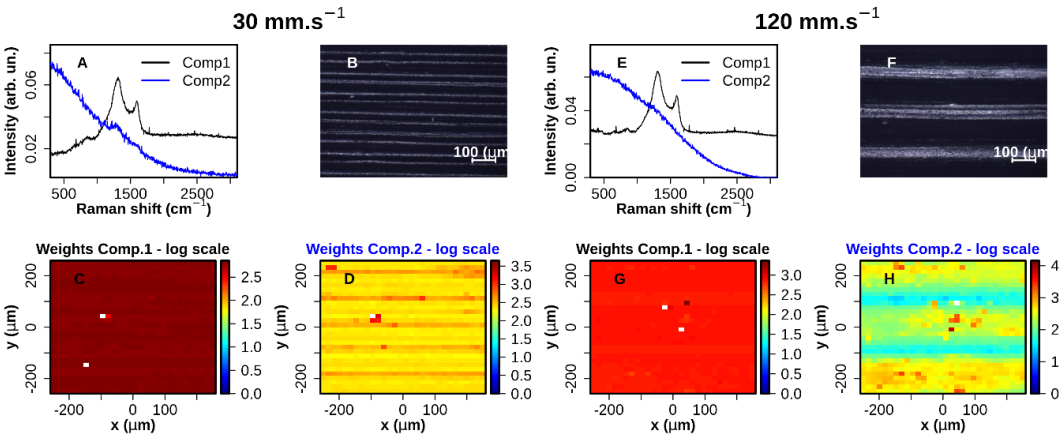

Figure 29. Raman study for the electrodes with printing perimeter speed variation in which (A and E) represent MCR-ALS pure component spectra, from which all the spectra collected in the mapped area are recovered by linear combinations. (B and F) Optical microscopy imagens of electrodes obtained with a 10x objective lens in the microscope coupled to the Raman spectrometer; (C, D, G and H) Electrode surface distribution of coefficients in the linear combination of MCR-ALS components.

The same studies were performed for electrodes with different perimeters (1 and 2 shells, **Figure 30** and **Figure 31**). As the optical microscopy images show (**Figure 31B** and **F**), there are no significant differences between both electrodes.

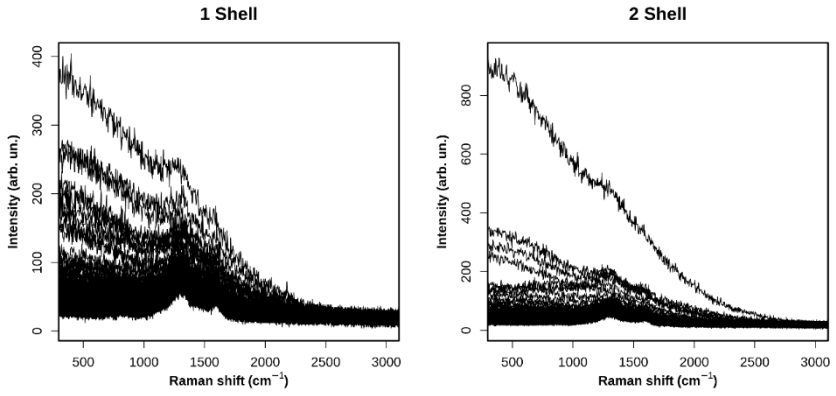

Figure 30. Raman spectra for two electrodes obtained with different perimeters (1 shell and 2 shells).

This can also be seen with the analysis of the separation of the components (**Figure 31A** and **E**), and in both mappings (**Figure 31C**, **D**, **G**, and **H**). The CB

distribution in PLA matrix appears less scattered and aggregates, this similarity is also seen on the CV experiments, showing one more time, a small difference between both perimeters. Thus, it is possible to affirm the different perimeters that were chosen did not drastically affect the electrode electrochemical response.

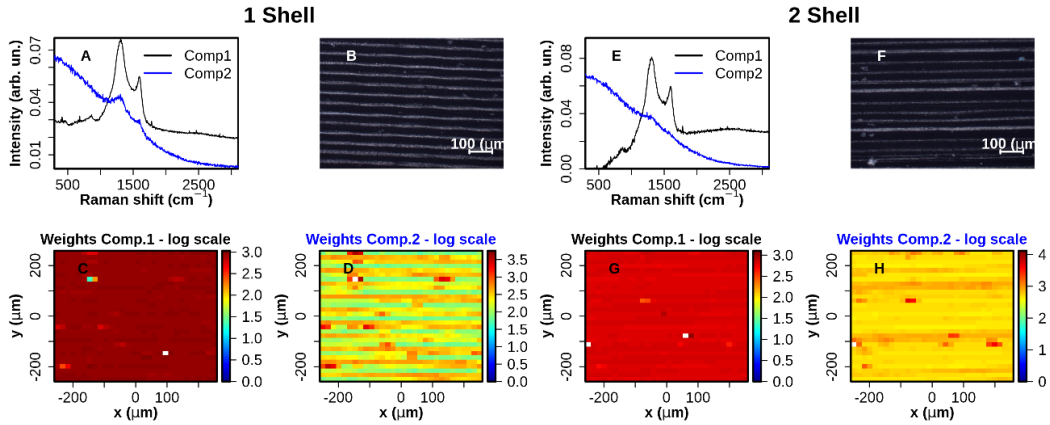

Figure 31. Raman study for the electrodes with perimeter number variation in which (**A** and **E**) showed MCR-ALS analysis representing 2 different components for the spectra. (**B** and **F**) Microscopic imaging of electrodes (10x objective lens). (**C**, **D**, **G** and **H**) Electrode mapping containing the component concentration distribution of across the mapping area.

Raman spectra and mappings of 3D-printed electrodes for both vertical and horizontal printing samples before MCR analysis are shown in **Figure 32**.

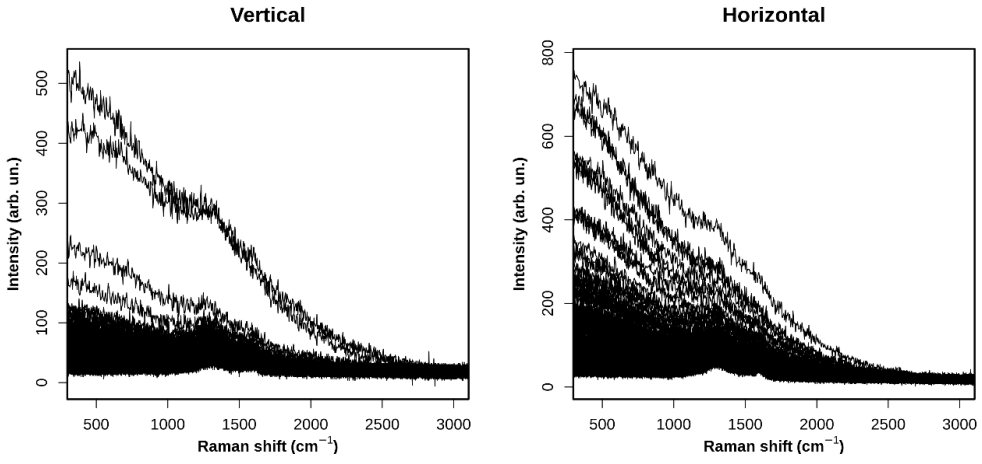

Figure 32. Raman spectra for electrodes obtained by horizontal and vertical printing orientations.

From the MCR-ALS concentration matrix we can obtain the surface distribution of the spectral features described by components 1 and 2. The results are presented in **Figure 33C** and **D** for horizontal printing and in **Figure 33G** and **H** for vertical printing. For CB (component 1 in both samples), it can be observed a mostly distribution over the mapped area, with a decreased contribution in points where in the background dominates (component 2). This same behavior can be observed for both samples.

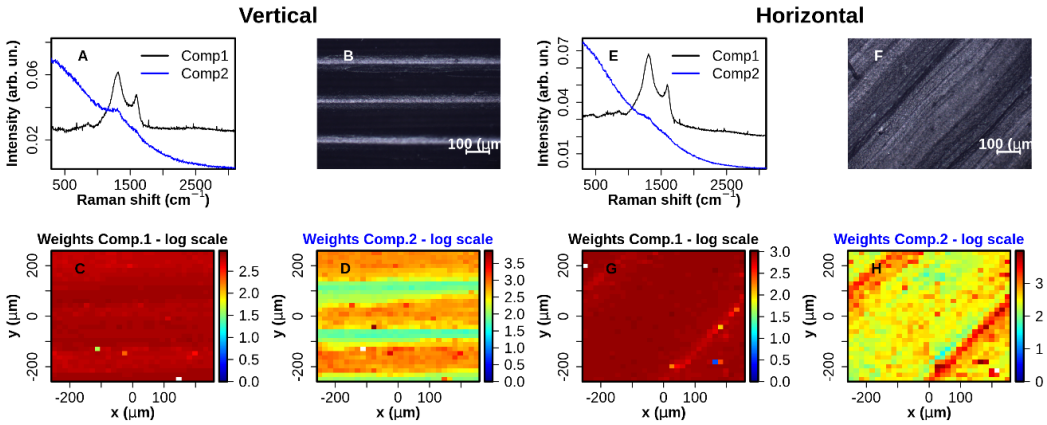

Figure 33. Raman study for the electrodes with vertical and horizontal printing orientation in which (**A** and **E**) represent MCR-ALS pure component spectra, from which all the spectra collected in the mapped area are recovered by linear combinations. (**B** and **F**) Optical microscopy imagens of electrodes obtained with a 10x objective lens in the microscope coupled to the Raman spectrometer; (**C**, **D**, **G** and **H**) Electrode surface distribution of coefficients in the linear combination of MCR-ALS components.

The comparison between surface distributions of CB Raman signals (**Figure 33C** and **G**) for vertical and horizontal printing orientations indicates a higher distribution of CB particles for the former. This could be the reason for the improvement in electrochemical response in the vertical printing.

Raman spectra and mappings of 3D-printed electrodes for the two different layer thicknesses (0.05 and 0.30 mm) before MCR analysis are shown in **Figure 34**.

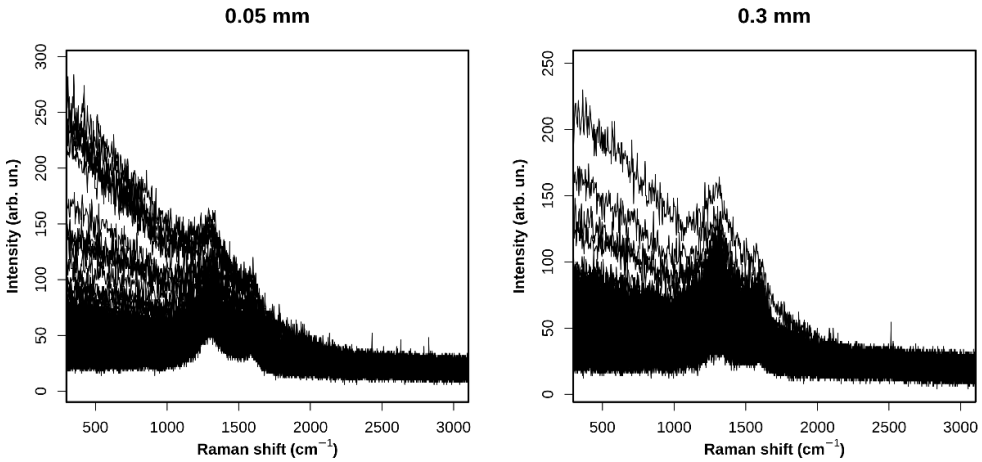

Figure 34. Raman spectra of electrodes obtained with two different layer thicknesses (0.05 and 0.3 mm).

In both electrodes, it was observed a low separation between components 1 and 2 after the mathematical treatment. The observed results suggest low phase segregation with the presence of D and G carbon band (component 1) on the background (PLA, component 2) (**Figure 35A** and **E** – blue lines).

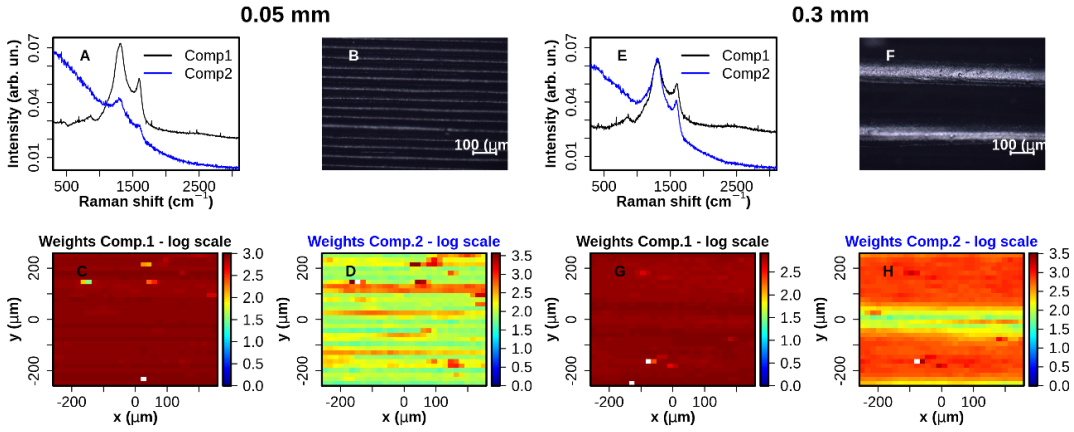

Figure 35. Raman study for the electrodes as function of layer thickness in which (**A** and **E**) represent MCR-ALS analysis of 2 different components for the spectra; (**B** and **F**) Microscopic imaging of electrode (10x objective lens) and (**C**, **D**, **G** and **H**) Electrode mapping containing the components concentration distribution across the mapping area.

Although the visual sample heterogeneity for 0.30 mm samples is higher than in 0.05 mm sample in terms of components 1 and 2 (obtained from chemometric analysis – MCR-ALS), it is not possible to quantify the influence of this difference. **Figure 35C** and **G** represent the distribution of conductive filler on the surface of the electrodes and the

observed results are similar. However, analyzing **Figure 35D** and **H**, different profiles are observed for the PLA (background). Sample 0.30 mm has valleys and peaks, and it has a distribution of PLA when compared with the sample of 0.05 mm, see **Figure 35B** and **F**. These results suggest that the distribution of conductive filaments during the printing process is an important parameter for the electrochemical activity of the 3D-printed electrodes.

6.4 Conclusion

Herein, it was demonstrated that 3D-printing parameters (printing perimeter speed, layer thickness, orientation, and perimeter number) can significantly influence the electrochemical performance of 3D-printed CB/PLA electrodes. In this study, lower printing perimeter speed (30 mm s^{-1}) presented a smaller charge transfer resistance of the electrodes. In addition, the perimeter number was also investigated and better voltammetric profile was achieved when two shells were used. Vertically printed electrodes and lower layer thickness (0.05 mm) provided enhancement in the cyclic voltammetric response for $[Ru(NH_3)_6]^{2+/3+}$ redox probe. EIS experiments and the estimated electrochemically active surface area agree with the cyclic voltammetric profile and indicated that the choice of 3D-printing parameters influences the charge transfer resistance. Experiments by Raman associated with MCR-ALS suggested that the differences in the peak-to-peak separation as well as faradaic current, are related to aggregation and scattering of CB particles in the internal structure of 3D-printed sensors.

7. GENERAL CONCLUSIONS

Herein, it was possible to clearly demonstrate potential applicability of FDM 3D-printers in the production of electrochemical sensors.

The possibility of incorporation of nickel microparticles in a conductive filament was shown for the first time. As a potential application, 3D-printed electrodes produced from this filament were evaluated in catalytic detection of glucose in basic medium. Although only nickel microparticles were added to the filament, this work can be used as a reference for the addition of other metals to conductive filaments. In other study, the Fe impurities present in the commercial conductive filaments were used to construct Prussian blue films, and the sensor was used to determine H_2O_2 in milk samples. This work was very interesting because it demonstrated that impurities present in conductive filaments could affect the electrochemical response of 3D-printed electrodes produced from the respective filament. Although 3D-printed electrodes can be a promising approach for developing low-cost sensors with suitable electrocatalytic properties, these electrodes present poor electrochemical responses, requiring activation/treatment on the electrode surface. This behavior was also demonstrated in this study because activation in an alkaline medium or immersion in DMF were used to enhance the electrochemical performance.

Finally, it was shown that the electrochemical activity of 3D-printed electrodes can be affected by printing parameters of 3D-printers. The results obtained by CV, Raman MCR-ALS, and EIS measurements indicate that printing parameters considerably affects the electrochemical response of 3D-printed electrodes. The results of Raman MCR-ALS analysis showed that the printing parameters can affect the aggregation and scattering of CB particles in the internal structure of 3D-printed sensors.

8. REFERENCES

[1] Q. He, B. Wang, J. Liang, J. Liu, B. Liang, G. Li, Y. Long, G. Zhang, H. Liu, Research on the construction of portable electrochemical sensors for environmental compounds quality monitoring, Mater. Today Adv. 17 (2023) 100340. https://doi.org/10.1016/j.mtadv.2022.100340.

[2] A. García-Miranda Ferrari, P. Carrington, S.J. Rowley-Neale, C.E. Banks, Recent advances in portable heavy metal electrochemical sensing platforms, Environ. Sci. Water Res. Technol. 6 (2020) 2676–2690. https://doi.org/10.1039/D0EW00407C.

[3] R. Umapathi, S.M. Ghoreishian, S. Sonwal, G.M. Rani, Y.S. Huh, Portable electrochemical sensing methodologies for on-site detection of pesticide residues in fruits and vegetables, Coord. Chem. Rev. 453 (2022) 214305. https://doi.org/10.1016/j.ccr.2021.214305.

[4] A. García-Miranda Ferrari, S.J. Rowley-Neale, C.E. Banks, Screen-printed electrodes: Transitioning the laboratory in-to-the field, Talanta Open 3 (2021) 100032. https://doi.org/10.1016/j.talo.2021.100032.

[5] R.D. Crapnell, C. Kalinke, L.R.G. Silva, J.S. Stefano, R.J. Williams, R.A. Abarza Munoz, J.A. Bonacin, B.C. Janegitz, C.E. Banks, Additive manufacturing electrochemistry: An overview of producing bespoke conductive additive manufacturing filaments, Mater. Today 71 (2023) 73–90. https://doi.org/10.1016/j.mattod.2023.11.002.

[6] J.S. Stefano, C. Kalinke, R.G. da Rocha, D.P. Rocha, V.A.O.P. da Silva, J.A. Bonacin, L. Angnes, E.M. Richter, B.C. Janegitz, R.A.A. Muñoz, Electrochemical (Bio)Sensors Enabled by Fused Deposition Modeling-Based 3D Printing: A Guide to Selecting Designs, Printing Parameters, and Post-Treatment Protocols, Anal. Chem. 94 (2022) 6417–6429. https://doi.org/10.1021/acs.analchem.1c05523.

[7] Z. Lyu, G.J.H. Lim, J.J. Koh, Y. Li, Y. Ma, J. Ding, J.J. Wang, Z. Hu, J.J. Wang, W. Chen, Y. Chen, Design and Manufacture of 3D-Printed Batteries, Joule 5 (2021) 89–114. https://doi.org/10.1016/j.joule.2020.11.010.

[8] C.M. Costa, R. Gonçalves, S. Lanceros-Méndez, Recent advances and future challenges in printed batteries, Energy Storage Mater. 28 (2020) 216–234. https://doi.org/10.1016/j.ensm.2020.03.012.

[9] E.M. Richter, D.P. Rocha, R.M. Cardoso, E.M. Keefe, C.W. Foster, R.A.A. Munoz, C.E. Banks, Complete Additively Manufactured (3D-Printed) Electrochemical Sensing Platform, Anal. Chem. 91 (2019) 12844–12851. https://doi.org/10.1021/acs.analchem.9b02573.

[10] M. Alizadehgiashi, A. Gevorkian, M. Tebbe, M. Seo, E. Prince, E. Kumacheva, 3D-Printed Microfluidic Devices for Materials Science, Adv. Mater. Technol. 3 (2018). https://doi.org/10.1002/admt.201800068.

[11] Y. He, Y. Wu, J. Fu, Q. Gao, J. Qiu, Developments of 3D Printing Microfluidics and Applications in Chemistry and Biology: a Review, Electroanalysis 28 (2016) 1658–1678. https://doi.org/10.1002/elan.201600043.

[12] A. Abdalla, B.A. Patel, 3D Printed Electrochemical Sensors, Annu. Rev. Anal. Chem. 14 (2021) 47–63. https://doi.org/10.1146/annurev-anchem-091120-093659.

[13] J. Muñoz, M. Pumera, Accounts in 3D-Printed Electrochemical Sensors: Towards Monitoring of Environmental Pollutants, ChemElectroChem 7 (2020) 3404–3413. https://doi.org/10.1002/celc.202000601.

[14] J. Yuan, M. Qiu, J.X. Chen, X. Hu, Y. Liu, B. Yu, G. Zhong, Z. Weng, H. Zhan, Z. Wen, High Mass Loading 3D-Printed Sodium-Ion Hybrid Capacitors, Adv. Funct. Mater. 32 (2022). https://doi.org/10.1002/adfm.202203732.

[15] N. V. Blaž, L.D. Živanov, M.G. Kisić, A.B. Menićanin, Fully 3D printed rolled capacitor based on conductive ABS composite electrodes, Electrochem. Commun. 134 (2022) 107178. https://doi.org/10.1016/j.elecom.2021.107178.

[16] M. May, A DIY approach to automating your lab, Nature 569 (2019) 587–588. https://doi.org/10.1038/d41586-019-01590-z.

[17] A.B. Kakarla, I. Kong, V.I. Patel, Additive Manufacturing for Building and Constructions, in: Addit. Manuf. with Nov. Mater., Wiley, 2024: pp. 485–508. https://doi.org/10.1002/9781394198085.ch16.

[18] I. Gibson, D.W. Rosen, B. Stucker, Additive Manufacturing Technologies, Springer US, Boston, MA, 2010. https://doi.org/10.1007/978-1-4419-1120-9.

[19] F. Calignano, D. Manfredi, E.P. Ambrosio, S. Biamino, M. Lombardi, E. Atzeni, A. Salmi, P. Minetola, L. Iuliano, P. Fino, Overview on Additive Manufacturing Technologies, Proc. IEEE 105 (2017) 593–612. https://doi.org/10.1109/JPROC.2016.2625098.

[20] K.R. Ryan, M.P. Down, C.E. Banks, Future of additive manufacturing: Overview of 4D and 3D printed smart and advanced materials and their applications, Chem. Eng. J. 403 (2021) 126162. https://doi.org/10.1016/j.cej.2020.126162.

[21] R.M. Cardoso, C. Kalinke, R.G. Rocha, P.L. dos Santos, D.P. Rocha, P.R. Oliveira, B.C. Janegitz, J.A. Bonacin, E.M. Richter, R.A.A. Munoz, Additive-manufactured (3D-printed) electrochemical sensors: A critical review, Anal. Chim. Acta 1118 (2020) 73–91. https://doi.org/10.1016/j.aca.2020.03.028.

[22] A. Ambrosi, M. Pumera, 3D-printing technologies for electrochemical applications, Chem. Soc. Rev. 45 (2016) 2740–2755. https://doi.org/10.1039/C5CS00714C.

[23] Ö. Keleş, C.W. Blevins, K.J. Bowman, Effect of build orientation on the mechanical reliability of 3D printed ABS, Rapid Prototyp. J. 23 (2017) 320–328. https://doi.org/10.1108/RPJ-09-2015-0122.

[24] J.J. Tully, G.N. Meloni, A Scientist's Guide to Buying a 3D Printer: How to Choose the Right Printer for Your Laboratory, Anal. Chem. 92 (2020) 14853–14860. https://doi.org/10.1021/acs.analchem.0c03299.

[25] T. Mikolajczyk, T. Malinowski, L. Moldovan, H. Fuwen, T. Paczkowski, I.

Ciobanu, CAD CAM System for Manufacturing Innovative Hybrid Design Using 3D Printing, Procedia Manuf. 32 (2019) 22–28. https://doi.org/10.1016/j.promfg.2019.02.178.

[26] S. Junk, C. Kuen, Review of Open Source and Freeware CAD Systems for Use with 3D-Printing, Procedia CIRP 50 (2016) 430–435. https://doi.org/10.1016/j.procir.2016.04.174.

[27] M. Pagac, J. Hajnys, Q.-P. Ma, L. Jancar, J. Jansa, P. Stefek, J. Mesicek, A Review of Vat Photopolymerization Technology: Materials, Applications, Challenges, and Future Trends of 3D Printing, Polymers (Basel). 13 (2021) 598. https://doi.org/10.3390/polym13040598.

[28] T. Duda, L.V. Raghavan, 3D Metal Printing Technology, IFAC-PapersOnLine 49 (2016) 103–110. https://doi.org/10.1016/j.ifacol.2016.11.111.

[29] B. Evans, Practical 3D printers: The science and art of 3D printing, Apress, 2012.

[30] A. Savini, G.G. Savini, A short history of 3D printing, a technological revolution just started, in: IEEE Int. Hist. High-Technologies Their Socio-Cultural Context. Conf., IEEE, 2015: pp. 1–8. https://doi.org/10.1109/HISTELCON.2015.7307314.

[31] S.J. Al'Aref, B. Mosadegh, S. Dunham, J.K. Min, 3D Printing Applications in Cardiovascular Medicine, Elsevier, 2018. https://doi.org/10.1016/C2015-0-00622-0.

[32] C.W. Hull, Apparatus for production of three dimensional objects by Stereolithography, 1986.

[33] C.R. Deckard, Apparatus for Producing Parts by Selective Sintering, 1997.

[34] S.S. Crump, Apparatus and method for creating three-dimensional objects, 1992.

[35] J. Horvath, Mastering 3D Printing, Apress, Berkeley, CA, 2014. https://doi.org/10.1007/978-1-4842-0025-4.

[36] ISO/ASTM 52900: Additive manufacturing — General principles — Fundamentals and vocabulary (second edition), (2021).

[37] F. Zhang, L. Zhu, Z. Li, S. Wang, J. Shi, W. Tang, N. Li, J. Yang, The recent development of vat photopolymerization: A review, Addit. Manuf. 48 (2021) 102423. https://doi.org/10.1016/j.addma.2021.102423.

[38] I. Gibson, D. Rosen, B. Stucker, Additive manufacturing technologies: 3D printing, rapid prototyping, and direct digital manufacturing, second edition, 2015. https://doi.org/10.1007/978-1-4939-2113-3.

[39] M.P. Watters, M.L. Bernhardt, Curing parameters to improve the mechanical properties of stereolithographic printed specimens, Rapid Prototyp. J. 24 (2018) 46–51. https://doi.org/10.1108/RPJ-11-2016-0180.

[40] Y.L. Yap, C. Wang, S.L. Sing, V. Dikshit, W.Y. Yeong, J. Wei, Material jetting additive manufacturing: An experimental study using designed metrological

benchmarks, Precis. Eng. 50 (2017) 275–285. https://doi.org/10.1016/j.precisioneng.2017.05.015.

[41] O. Gülcan, K. Günaydın, A. Tamer, The State of the Art of Material Jetting—A Critical Review, Polymers (Basel). 13 (2021) 2829. https://doi.org/10.3390/polym13162829.

[42] M. Ziaee, N.B. Crane, Binder jetting: A review of process, materials, and methods, Addit. Manuf. 28 (2019) 781–801. https://doi.org/10.1016/j.addma.2019.05.031.

[43] H. Miyanaji, N. Momenzadeh, L. Yang, Effect of printing speed on quality of printed parts in Binder Jetting Process, Addit. Manuf. 20 (2018) 1–10. https://doi.org/10.1016/j.addma.2017.12.008.

[44] M. Li, W. Du, A. Elwany, Z. Pei, C. Ma, Metal binder jetting additive manufacturing: A literature review, J. Manuf. Sci. Eng. Trans. ASME 142 (2020). https://doi.org/10.1115/1.4047430/1084395.

[45] X. Lv, F. Ye, L. Cheng, S. Fan, Y. Liu, Binder jetting of ceramics: Powders, binders, printing parameters, equipment, and post-treatment, Ceram. Int. 45 (2019) 12609–12624. https://doi.org/10.1016/j.ceramint.2019.04.012.

[46] S. Vock, B. Klöden, A. Kirchner, T. Weißgärber, B. Kieback, Powders for powder bed fusion: a review, Prog. Addit. Manuf. 4 (2019) 383–397. https://doi.org/10.1007/s40964-019-00078-6.

[47] W.E. King, A.T. Anderson, R.M. Ferencz, N.E. Hodge, C. Kamath, S.A. Khairallah, A.M. Rubenchik, Laser powder bed fusion additive manufacturing of metals; physics, computational, and materials challenges, Appl. Phys. Rev. 2 (2015) 041304. https://doi.org/10.1063/1.4937809.

[48] S.L. Sing, C.F. Tey, J.H.K. Tan, S. Huang, W.Y. Yeong, 3D printing of metals in rapid prototyping of biomaterials: Techniques in additive manufacturing, in: Rapid Prototyp. Biomater., Elsevier, 2020: pp. 17–40. https://doi.org/10.1016/B978-0-08-102663-2.00002-2.

[49] N. Volpato, J.V.L. Silva, Aplicação direta da manufatura aditiva na fabricação final, in: Manufatura Aditiva Tecnol. e Apl. Da Impressão 3D, Blusher, São Paulo, 2017: pp. 325–344.

[50] D.J. Braconnier, R.E. Jensen, A.M. Peterson, Processing parameter correlations in material extrusion additive manufacturing, Addit. Manuf. 31 (2020) 100924. https://doi.org/10.1016/j.addma.2019.100924.

[51] S.C. Daminabo, S. Goel, S.A. Grammatikos, H.Y. Nezhad, V.K. Thakur, Fused deposition modeling-based additive manufacturing (3D printing): techniques for polymer material systems, Mater. Today Chem. 16 (2020) 100248. https://doi.org/10.1016/j.mtchem.2020.100248.

[52] R.B. Kristiawan, F. Imaduddin, D. Ariawan, Ubaidillah, Z. Arifin, A review on the fused deposition modeling (FDM) 3D printing: Filament processing, materials, and printing parameters, Open Eng. 11 (2021) 639–649. https://doi.org/10.1515/ENG-

2021-0063/HTML.

[53] J. Muñoz, M. Pumera, 3D-printed biosensors for electrochemical and optical applications, TrAC Trends Anal. Chem. 128 (2020) 115933. https://doi.org/10.1016/J.TRAC.2020.115933.

[54] K.R. Ryan, M.P. Down, N.J. Hurst, E.M. Keefe, C.E. Banks, Additive manufacturing (3D printing) of electrically conductive polymers and polymer nanocomposites and their applications, EScience 2 (2022) 365–381. https://doi.org/10.1016/j.esci.2022.07.003.

[55] D.M. Wirth, M.J. Sheaff, J. V. Waldman, M.P. Symcox, H.D. Whitehead, J.D. Sharp, J.R. Doerfler, A.A. Lamar, G. Leblanc, Electrolysis activation of fused-filament-fabrication 3D-printed electrodes for electrochemical and spectroelectrochemical analysis, Anal. Chem. 91 (2019) 5553–5557. https://doi.org/10.1021/acs.analchem.9b01331.

[56] T.A. Silva, F.C. Moraes, B.C. Janegitz, O. Fatibello-Filho, Electrochemical biosensors based on nanostructured carbon black: A review, J. Nanomater. 2017 (2017) 1–14. https://doi.org/10.1155/2017/4571614.

[57] D. Zhang, B. Chi, B. Li, Z. Gao, Y. Du, J. Guo, J. Wei, Fabrication of highly conductive graphene flexible circuits by 3D printing, Synth. Met. 217 (2016) 79–86. https://doi.org/10.1016/j.synthmet.2016.03.014.

[58] C.W. Foster, M.P. Down, Y. Zhang, X. Ji, S.J. Rowley-Neale, G.C. Smith, P.J. Kelly, C.E. Banks, 3D Printed graphene based energy storage devices, Sci. Rep. 7 (2017) 42233. https://doi.org/10.1038/srep42233.

[59] G.D. O'Neil, Toward single-step production of functional electrochemical devices using 3D printing: Progress, challenges, and opportunities, Curr. Opin. Electrochem. 20 (2020) 60–65. https://doi.org/10.1016/j.coelec.2020.02.023.

[60] M.H. Omar, K.A. Razak, M.N. Ab Wahab, H.H. Hamzah, Recent progress of conductive 3D-printed electrodes based upon polymers/carbon nanomaterials using a fused deposition modelling (FDM) method as emerging electrochemical sensing devices, RSC Adv. 11 (2021) 16557–16571. https://doi.org/10.1039/d1ra01987b.

[61] S.J. Leigh, R.J. Bradley, C.P. Purssell, D.R. Billson, D.A. Hutchins, A Simple, Low-Cost Conductive Composite Material for 3D Printing of Electronic Sensors, PLoS One 7 (2012) e49365. https://doi.org/10.1371/journal.pone.0049365.

[62] J.S. Stefano, L.R.G. e Silva, B.C. Janegitz, New carbon black-based conductive filaments for the additive manufacture of improved electrochemical sensors by fused deposition modeling, Microchim. Acta 189 (2022) 414. https://doi.org/10.1007/s00604-022-05511-2.

[63] C.W. Foster, G. Zou, Y. Jiang, M.P. Down, C.M. Liauw, A. Garcia-Miranda Ferrari, X. Ji, G.C. Smith, P.J. Kelly, C.E. Banks, Next-Generation Additive Manufacturing: Tailorable Graphene/Polylactic(acid) Filaments Allow the Fabrication of 3D Printable Porous Anodes for Utilisation within Lithium-Ion

Batteries, Batter. Supercaps 2 (2019) 448–453. https://doi.org/10.1002/batt.201800148.

[64] A. García-Miranda Ferrari, J.L. Pimlott, M.P. Down, S.J. Rowley-Neale, C.E. Banks, MoO 2 Nanowire Electrochemically Decorated Graphene Additively Manufactured Supercapacitor Platforms, Adv. Energy Mater. 11 (2021). https://doi.org/10.1002/aenm.202100433.

[65] J.S. Stefano, L.R. Guterres e Silva, R.G. Rocha, L.C. Brazaca, E.M. Richter, R.A. Abarza Muñoz, B.C. Janegitz, New conductive filament ready-to-use for 3D-printing electrochemical (bio)sensors: Towards the detection of SARS-CoV-2, Anal. Chim. Acta 1191 (2022) 339372. https://doi.org/10.1016/j.aca.2021.339372.

[66] O. Urra Sanchez, H. Besharatloo, J. Yus, A.J. Sanchez-Herencia, B. Ferrari, Material thermal extrusion of conductive 3D electrodes using highly loaded graphene and graphite colloidal feedstock, Addit. Manuf. 72 (2023) 103643. https://doi.org/10.1016/j.addma.2023.103643.

[67] X. Wei, D. Li, W. Jiang, Z. Gu, X. Wang, Z. Zhang, Z. Sun, 3D Printable Graphene Composite, Sci. Rep. 5 (2015) 11181. https://doi.org/10.1038/srep11181.

[68] N.-A. Masarra, M. Batistella, J.-C. Quantin, A. Regazzi, M.F. Pucci, R. El Hage, J.-M. Lopez-Cuesta, Fabrication of PLA/PCL/Graphene Nanoplatelet (GNP) Electrically Conductive Circuit Using the Fused Filament Fabrication (FFF) 3D Printing Technique, Materials (Basel). 15 (2022) 762. https://doi.org/10.3390/ma15030762.

[69] E. Sigley, C. Kalinke, R.D. Crapnell, M.J. Whittingham, R.J. Williams, E.M. Keefe, B.C. Janegitz, J.A. Bonacin, C.E. Banks, Circular Economy Electrochemistry: Creating Additive Manufacturing Feedstocks for Caffeine Detection from Post-Industrial Coffee Pod Waste, ACS Sustain. Chem. Eng. 11 (2023) 2978–2988. https://doi.org/10.1021/acssuschemeng.2c06514.

[70] I.V.S. Arantes, R.D. Crapnell, E. Bernalte, M.J. Whittingham, T.R.L.C. Paixão, C.E. Banks, Mixed Graphite/Carbon Black Recycled PLA Conductive Additive Manufacturing Filament for the Electrochemical Detection of Oxalate, Anal. Chem. 95 (2023) 15086–15093. https://doi.org/10.1021/acs.analchem.3c03193.

[71] C. Kalinke, R.D. Crapnell, E. Sigley, M.J. Whittingham, P.R. de Oliveira, L.C. Brazaca, B.C. Janegitz, J.A. Bonacin, C.E. Banks, Recycled additive manufacturing feedstocks with carboxylated multi-walled carbon nanotubes toward the detection of yellow fever virus cDNA, Chem. Eng. J. 467 (2023) 143513. https://doi.org/10.1016/j.cej.2023.143513.

[72] R.D. Crapnell, I.V.S. Arantes, M.J. Whittingham, E. Sigley, C. Kalinke, B.C. Janegitz, J.A. Bonacin, T.R.L.C. Paixão, C.E. Banks, Utilising bio-based plasticiser castor oil and recycled PLA for the production of conductive additive manufacturing feedstock and detection of bisphenol A, Green Chem. 25 (2023) 5591–5600. https://doi.org/10.1039/D3GC01700A.

[73] D.P. Rocha, R.G. Rocha, S.V.F. Castro, M.A.G. Trindade, R.A.A. Munoz, E.M. Richter, L. Angnes, Posttreatment of 3D-printed surfaces for electrochemical

applications: A critical review on proposed protocols, Electrochem. Sci. Adv. 2 (2022). https://doi.org/10.1002/elsa.202100136.

[74] A.W. Hashmi, H.S. Mali, A. Meena, K.K. Saxena, S. Ahmad, M.K. Agrawal, B. Sagbas, A.P. Valerga Puerta, M.I. Khan, A comprehensive review on surface post-treatments for freeform surfaces of bio-implants, J. Mater. Res. Technol. 23 (2023) 4866–4908. https://doi.org/10.1016/j.jmrt.2023.02.007.

[75] R. Gusmão, M.P. Browne, Z. Sofer, M. Pumera, The capacitance and electron transfer of 3D-printed graphene electrodes are dramatically influenced by the type of solvent used for pre-treatment, Electrochem. Commun. 102 (2019) 83–88. https://doi.org/10.1016/j.elecom.2019.04.004.

[76] P.L. dos Santos, V. Katic, H.C. Loureiro, M.F. dos Santos, D.P. dos Santos, A.L.B. Formiga, J.A. Bonacin, Enhanced performance of 3D printed graphene electrodes after electrochemical pre-treatment: Role of exposed graphene sheets, Sensors Actuators B Chem. 281 (2019) 837–848. https://doi.org/10.1016/j.snb.2018.11.013.

[77] V. Katic, P.L. dos Santos, M.F. dos Santos, B.M. Pires, H.C. Loureiro, A.P. Lima, J.C.M. Queiroz, R. Landers, R.A.A. Muñoz, J.A. Bonacin, 3D Printed Graphene Electrodes Modified with Prussian Blue: Emerging Electrochemical Sensing Platform for Peroxide Detection, ACS Appl. Mater. Interfaces 11 (2019) 35068–35078. https://doi.org/10.1021/acsami.9b09305.

[78] E. Redondo, J. Muñoz, M. Pumera, Green activation using reducing agents of carbon-based 3D printed electrodes: Turning good electrodes to great, Carbon N. Y. 175 (2021) 413–419. https://doi.org/10.1016/j.carbon.2021.01.107.

[79] V.A.O.P. Silva, W.S. Fernandes-Junior, D.P. Rocha, J.S. Stefano, R.A.A. Munoz, J.A. Bonacin, B.C. Janegitz, 3D-printed reduced graphene oxide/polylactic acid electrodes: A new prototyped platform for sensing and biosensing applications, Biosens. Bioelectron. 170 (2020) 112684. https://doi.org/10.1016/j.bios.2020.112684.

[80] C.L. Manzanares-Palenzuela, S. Hermanova, Z. Sofer, M. Pumera, Proteinase-sculptured 3D-printed graphene/polylactic acid electrodes as potential biosensing platforms: towards enzymatic modeling of 3D-printed structures, Nanoscale 11 (2019) 12124–12131. https://doi.org/10.1039/C9NR02754H.

[81] F. Novotný, V. Urbanová, J. Plutnar, M. Pumera, Preserving Fine Structure Details and Dramatically Enhancing Electron Transfer Rates in Graphene 3D-Printed Electrodes via Thermal Annealing: Toward Nitroaromatic Explosives Sensing, ACS Appl. Mater. Interfaces 11 (2019) 35371–35375. https://doi.org/10.1021/acsami.9b06683.

[82] M.J. Glowacki, M. Cieslik, M. Sawczak, A. Koterwa, I. Kaczmarzyk, R. Jendrzejewski, L. Szynkiewicz, T. Ossowski, R. Bogdanowicz, P. Niedzialkowski, J. Ryl, Helium-assisted, solvent-free electro-activation of 3D printed conductive carbon-polylactide electrodes by pulsed laser ablation, Appl. Surf. Sci. 556 (2021) 149788. https://doi.org/10.1016/j.apsusc.2021.149788.

[83] D.P. Rocha, V.N. Ataide, A. de Siervo, J.M. Gonçalves, R.A.A. Muñoz, T.R.L.C. Paixão, L. Angnes, Reagentless and sub-minute laser-scribing treatment to produce enhanced disposable electrochemical sensors via additive manufacture, Chem. Eng. J. 425 (2021) 130594. https://doi.org/10.1016/j.cej.2021.130594.

[84] J.F.S. Pereira, R.G. Rocha, S.V.F. Castro, A.F. João, P.H.S. Borges, D.P. Rocha, A. de Siervo, E.M. Richter, E. Nossol, R. V. Gelamo, R.A.A. Muñoz, Reactive oxygen plasma treatment of 3D-printed carbon electrodes towards high-performance electrochemical sensors, Sensors Actuators B Chem. 347 (2021) 130651. https://doi.org/10.1016/j.snb.2021.130651.

[85] S.M. Sibug-Torres, L.P. Go, V.C.G. Castillo, J.L.R. Pauco, E.P. Enriquez, Fully integrated 3D-printed electrochemical cell with a modified inkjet-printed Ag electrode for voltammetric nitrate analysis, Anal. Chim. Acta 1160 (2021) 338430. https://doi.org/10.1016/j.aca.2021.338430.

[86] G.D. da Silveira, L.P. Bressan, M.E.P. Schmidt, T.R. Dal Molin, C.A. Teixeira, R.J. Poppi, J.A.F. da Silva, Electrochemical behavior of 5-type phosphodiesterase inhibitory drugs in solid state by voltammetry of immobilized microparticles, J. Solid State Electrochem. 24 (2020) 1999–2010. https://doi.org/10.1007/s10008-020-04533-1.

[87] L.A. Pradela-Filho, D.A.G. Araújo, V.N. Ataide, G.N. Meloni, T.R.L.C. Paixão, Challenges faced with 3D-printed electrochemical sensors in analytical applications, Anal. Bioanal. Chem. (2024). https://doi.org/10.1007/s00216-024-05308-7.

[88] H. Ragones, D. Schreiber, A. Inberg, O. Berkh, G. Kósa, A. Freeman, Y. Shacham-Diamand, Disposable electrochemical sensor prepared using 3D printing for cell and tissue diagnostics, Sensors Actuators B Chem. 216 (2015) 434–442. https://doi.org/10.1016/j.snb.2015.04.065.

[89] C.L. Manzanares Palenzuela, F. Novotný, P. Krupička, Z. Sofer, M. Pumera, 3D-Printed Graphene/Polylactic Acid Electrodes Promise High Sensitivity in Electroanalysis, Anal. Chem. 90 (2018) 5753–5757. https://doi.org/10.1021/acs.analchem.8b00083.

[90] R.M. Cardoso, D.M.H. Mendonça, W.P. Silva, M.N.T. Silva, E. Nossol, R.A.B. da Silva, E.M. Richter, R.A.A. Muñoz, 3D printing for electroanalysis: From multiuse electrochemical cells to sensors, Anal. Chim. Acta 1033 (2018) 49–57. https://doi.org/10.1016/j.aca.2018.06.021.

[91] R.M. Cardoso, S.V.F. Castro, M.N.T. Silva, A.P. Lima, M.H.P. Santana, E. Nossol, R.A.B. Silva, E.M. Richter, T.R.L.C. Paixão, R.A.A. Muñoz, 3D-printed flexible device combining sampling and detection of explosives, Sensors Actuators B Chem. 292 (2019) 308–313. https://doi.org/10.1016/j.snb.2019.04.126.

[92] K.P.A. Kumar, K. Ghosh, O. Alduhaish, M. Pumera, Metal-plated 3D-printed electrode for electrochemical detection of carbohydrates, Electrochem. Commun. 120 (2020) 106827. https://doi.org/10.1016/j.elecom.2020.106827.

[93] C. Kalinke, N.V. Neumsteir, P. Roberto de Oliveira, B.C. Janegitz, J.A. Bonacin,

Sensing of L-methionine in biological samples through fully 3D-printed electrodes, Anal. Chim. Acta 1142 (2021) 135–142. https://doi.org/10.1016/j.aca.2020.10.034.

[94] V. Katseli, A. Economou, C. Kokkinos, A novel all-3D-printed cell-on-a-chip device as a useful electroanalytical tool: Application to the simultaneous voltammetric determination of caffeine and paracetamol, Talanta 208 (2020) 120388. https://doi.org/10.1016/j.talanta.2019.120388.

[95] J. Junpha, A. Wisitsoraat, R. Prathumwan, W. Chaengsawang, K. Khomungkhun, K. Subannajui, Electronic tongue and cyclic voltammetric sensors based on carbon nanotube/polylactic composites fabricated by fused deposition modelling 3D printing, Mater. Sci. Eng. C 117 (2020) 111319. https://doi.org/10.1016/j.msec.2020.111319.

[96] C. Kokkinos, A. Economou, A. Pournara, M. Manos, I. Spanopoulos, M. Kanatzidis, T. Tziotzi, V. Petkov, A. Margariti, P. Oikonomopoulos, G.S. Papaefstathiou, 3D-printed lab-in-a-syringe voltammetric cell based on a working electrode modified with a highly efficient Ca-MOF sorbent for the determination of Hg(II), Sensors Actuators B Chem. 321 (2020) 128508. https://doi.org/10.1016/j.snb.2020.128508.

[97] V. Katseli, A. Economou, C. Kokkinos, Single-step fabrication of an integrated 3D-printed device for electrochemical sensing applications, Electrochem. Commun. 103 (2019) 100–103. https://doi.org/10.1016/j.elecom.2019.05.008.

[98] A.F. João, A.L. Squissato, E.M. Richter, R.A.A. Muñoz, Additive-manufactured sensors for biofuel analysis: copper determination in bioethanol using a 3D-printed carbon black/polylactic electrode, Anal. Bioanal. Chem. 412 (2020) 2755–2762. https://doi.org/10.1007/s00216-020-02513-y.

[99] G.P. Siqueira, D.A.G. Araújo, L. V. de Faria, D.L.O. Ramos, T.A. Matias, E.M. Richter, T.R.L.C. Paixão, R.A.A. Muñoz, A novel 3D-printed graphite/polylactic acid sensor for the electrochemical determination of 2,4,6-trinitrotoluene residues in environmental waters, Chemosphere 340 (2023) 139796. https://doi.org/10.1016/j.chemosphere.2023.139796.

[100] I.V.S. Arantes, R.D. Crapnell, M.J. Whittingham, E. Sigley, T.R.L.C. Paixão, C.E. Banks, Additive Manufacturing of a Portable Electrochemical Sensor with a Recycled Conductive Filament for the Detection of Atropine in Spiked Drink Samples, ACS Appl. Eng. Mater. 1 (2023) 2397–2406. https://doi.org/10.1021/acsaenm.3c00345.

[101] H.H. Hamzah, S.A. Shafiee, A. Abdalla, B.A. Patel, 3D printable conductive materials for the fabrication of electrochemical sensors: A mini review, Electrochem. Commun. 96 (2018) 27–31. https://doi.org/10.1016/j.elecom.2018.09.006.

[102] J.P. Hughes, P.L. dos Santos, M.P. Down, C.W. Foster, J.A. Bonacin, E.M. Keefe, S.J. Rowley-Neale, C.E. Banks, Single step additive manufacturing (3D printing) of electrocatalytic anodes and cathodes for efficient water splitting, Sustain. Energy Fuels 4 (2020) 302–311. https://doi.org/10.1039/C9SE00679F.

[103] P.L. Santos, S.J. Rowley-Neale, A.G.M. Ferrari, J.A. Bonacin, C.E. Banks, Ni−Fe (Oxy)hydroxide Modified Graphene Additive Manufactured (3D-Printed) Electrochemical Platforms as an Efficient Electrocatalyst for the Oxygen Evolution Reaction, ChemElectroChem 6 (2019) 5633–5641. https://doi.org/10.1002/celc.201901541.

[104] Z. Rymansaib, P. Iravani, E. Emslie, M. Medvidović-Kosanović, M. Sak-Bosnar, R. Verdejo, F. Marken, All-Polystyrene 3D-Printed Electrochemical Device with Embedded Carbon Nanofiber-Graphite-Polystyrene Composite Conductor, Electroanalysis 28 (2016) 1517–1523. https://doi.org/10.1002/elan.201600017.

[105] C.Y. Foo, H.N. Lim, M.A. Mahdi, M.H. Wahid, N.M. Huang, Three-Dimensional Printed Electrode and Its Novel Applications in Electronic Devices, Sci. Rep. 8 (2018) 7399. https://doi.org/10.1038/s41598-018-25861-3.

[106] M.P. Browne, F. Novotný, Z. Sofer, M. Pumera, 3D Printed Graphene Electrodes' Electrochemical Activation, ACS Appl. Mater. Interfaces 10 (2018) 40294–40301. https://doi.org/10.1021/acsami.8b14701.

[107] C. Kalinke, N.V. Neumsteir, G. de O. Aparecido, T.V. de B. Ferraz, P.L. dos Santos, B.C. Janegitz, J.A. Bonacin, Comparison of activation processes for 3D printed PLA-graphene electrodes: electrochemical properties and application for sensing of dopamine, Analyst 145 (2020) 1207–1218. https://doi.org/10.1039/C9AN01926J.

[108] R.M. Cardoso, P.R.L. Silva, A.P. Lima, D.P. Rocha, T.C. Oliveira, T.M. do Prado, E.L. Fava, O. Fatibello-Filho, E.M. Richter, R.A.A. Muñoz, 3D-Printed graphene/polylactic acid electrode for bioanalysis: Biosensing of glucose and simultaneous determination of uric acid and nitrite in biological fluids, Sensors Actuators B Chem. 307 (2020) 127621. https://doi.org/10.1016/j.snb.2019.127621.

[109] M.M. Barsan, T.A. Enache, N. Preda, G. Stan, N.G. Apostol, E. Matei, A. Kuncser, V.C. Diculescu, Direct Immobilization of Biomolecules through Magnetic Forces on Ni Electrodes via Ni Nanoparticles: Applications in Electrochemical Biosensors, ACS Appl. Mater. Interfaces 11 (2019) 19867–19877. https://doi.org/10.1021/acsami.9b04990.

[110] A.M. López Marzo, C.C. Mayorga-Martinez, M. Pumera, 3D-printed graphene direct electron transfer enzyme biosensors, Biosens. Bioelectron. 151 (2020) 111980. https://doi.org/10.1016/j.bios.2019.111980.

[111] Y. Zhang, W. Lei, Q. Wu, X. Xia, Q. Hao, Amperometric nonenzymatic determination of glucose via a glassy carbon electrode modified with nickel hydroxide and N-doped reduced graphene oxide, Microchim. Acta 184 (2017) 3103–3111. https://doi.org/10.1007/s00604-017-2332-y.

[112] P. Du, P. Wu, C. Cai, A glucose biosensor based on electrocatalytic oxidation of NADPH at single-walled carbon nanotubes functionalized with poly(nile blue A), J. Electroanal. Chem. 624 (2008) 21–26. https://doi.org/10.1016/j.jelechem.2008.07.031.

[113] S.K. Hassaninejad–Darzi, M. Rahimnejad, S.N. Mirzababaei, Electrocatalytic oxidation of glucose onto carbon paste electrode modified with nickel hydroxide decorated NaA nanozeolite, Microchem. J. 128 (2016) 7–17. https://doi.org/10.1016/j.microc.2016.03.016.

[114] L. Rong, C. Yang, Q. Qian, X. Xia, Study of the nonenzymatic glucose sensor based on highly dispersed Pt nanoparticles supported on carbon nanotubes, Talanta 72 (2007) 819–824. https://doi.org/10.1016/j.talanta.2006.12.037.

[115] H. Qiu, X. Huang, Effects of Pt decoration on the electrocatalytic activity of nanoporous gold electrode toward glucose and its potential application for constructing a nonenzymatic glucose sensor, J. Electroanal. Chem. 643 (2010) 39–45. https://doi.org/10.1016/j.jelechem.2010.03.011.

[116] W. Wang, R. Li, X. Hua, R. Zhang, Methanol electrooxidation on glassy carbon electrode modified with bimetallic Ni(II)Co(II)salen complexes encapsulated in mesoporous zeolite A, Electrochim. Acta 163 (2015) 48–56. https://doi.org/10.1016/j.electacta.2015.02.128.

[117] J.L. Bott-Neto, T.S. Martins, S.A.S. Machado, E.A. Ticianelli, Electrocatalytic Oxidation of Methanol, Ethanol, and Glycerol on Ni(OH)2 Nanoparticles Encapsulated with Poly[Ni(salen)] Film, ACS Appl. Mater. Interfaces 11 (2019) 30810–30818. https://doi.org/10.1021/acsami.9b08441.

[118] R.E. Reim, R.M. Van Effen, Determination of carbohydrates by liquid chromatography with oxidation at a nickel(III) oxide electrode, Anal. Chem. 58 (1986) 3203–3207. https://doi.org/10.1021/ac00127a062.

[119] C.-Y. Ko, J.-H. Huang, S. Raina, W.P. Kang, A high performance non-enzymatic glucose sensor based on nickel hydroxide modified nitrogen-incorporated nanodiamonds, Analyst 138 (2013) 3201. https://doi.org/10.1039/c3an36679k.

[120] K.-C. Lin, Y.-C. Lin, S.-M. Chen, A highly sensitive nonenzymatic glucose sensor based on multi-walled carbon nanotubes decorated with nickel and copper nanoparticles, Electrochim. Acta 96 (2013) 164–172. https://doi.org/10.1016/j.electacta.2013.02.098.

[121] S. Zhang, Y. Fu, Q. Sheng, J. Zheng, Nickel–cobalt double hydroxide nanosheets wrapped amorphous Ni(OH) 2 nanoboxes: development of dopamine sensor with enhanced electrochemical properties, New J. Chem. 41 (2017) 13076–13084. https://doi.org/10.1039/C7NJ01835E.

[122] M. Fleischmann, K. Korinek, D. Pletcher, The oxidation of organic compounds at a nickel anode in alkaline solution, J. Electroanal. Chem. Interfacial Electrochem. 31 (1971) 39–49. https://doi.org/10.1016/S0022-0728(71)80040-2.

[123] P.K. Sonkar, V. Ganesan, S.A. John, D.K. Yadav, R. Gupta, Non-enzymatic electrochemical sensing platform based on metal complex immobilized carbon nanotubes for glucose determination, RSC Adv. 6 (2016) 107094–107103. https://doi.org/10.1039/C6RA16064F.

[124] M. Rezaeinasab, A. Benvidi, M.D. Tezerjani, S. Jahanbani, A.H. Kianfar, M.

Sedighipoor, An Electrochemical Sensor Based on Ni(II) Complex and Multi Wall Carbon Nano Tubes Platform for Determination of Glucose in Real Samples, Electroanalysis 29 (2017) 423–432. https://doi.org/10.1002/elan.201600162.

[125] B. Peng, J. Lu, A.S. Balijepalli, T.C. Major, B.E. Cohan, M.E. Meyerhoff, Evaluation of enzyme-based tear glucose electrochemical sensors over a wide range of blood glucose concentrations, Biosens. Bioelectron. 49 (2013) 204–209. https://doi.org/10.1016/j.bios.2013.05.014.

[126] M.A. Cruz, S. Ye, M.J. Kim, C. Reyes, F. Yang, P.F. Flowers, B.J. Wiley, Multigram Synthesis of Cu-Ag Core-Shell Nanowires Enables the Production of a Highly Conductive Polymer Filament for 3D Printing Electronics, Part. Part. Syst. Charact. 35 (2018) 1700385. https://doi.org/10.1002/ppsc.201700385.

[127] P. Chaturvedi, S. Sarker, X. Chen, S. Das, H. Luo, S.N. Smirnov, Enhancing the Cooperative Catalytic Effect in Ni/Co Hydr(oxy)oxide Porous Electrodes for Overall Water Splitting and Glucose Sensing, ACS Sustain. Chem. Eng. 7 (2019) 11303–11312. https://doi.org/10.1021/acssuschemeng.9b00822.

[128] X. Chen, G. Wu, Z. Cai, M. Oyama, X. Chen, Advances in enzyme-free electrochemical sensors for hydrogen peroxide, glucose, and uric acid, Microchim. Acta 181 (2014) 689–705. https://doi.org/10.1007/s00604-013-1098-0.

[129] C. Kalinke, V. Wosgrau, P.R. Oliveira, G.A. Oliveira, G. Martins, A.S. Mangrich, M.F. Bergamini, L.H. Marcolino-Junior, Green method for glucose determination using microfluidic device with a non-enzymatic sensor based on nickel oxyhydroxide supported at activated biochar, Talanta 200 (2019) 518–525. https://doi.org/10.1016/j.talanta.2019.03.079.

[130] D.S. Hall, D.J. Lockwood, C. Bock, B.R. MacDougall, Nickel hydroxides and related materials: a review of their structures, synthesis and properties, Proc. R. Soc. A Math. Phys. Eng. Sci. 471 (2015) 20140792. https://doi.org/10.1098/rspa.2014.0792.

[131] D. Yang, R. Wang, M. He, J. Zhang, Z. Liu, Ribbon- and Boardlike Nanostructures of Nickel Hydroxide: Synthesis, Characterization, and Electrochemical Properties, J. Phys. Chem. B 109 (2005) 7654–7658. https://doi.org/10.1021/jp050083b.

[132] J.J. Pedrotti, L. Angnes, I.G.R.R. Gutz, Miniaturized reference electrodes with microporous polymer junctions, Electroanalysis 8 (1996) 673–675. https://doi.org/10.1002/elan.1140080713.

[133] P.F. Pereira, M.C. Marra, R.A.A. Munoz, E.M. Richter, Fast batch injection analysis system for on-site determination of ethanol in gasohol and fuel ethanol, Talanta 90 (2012) 99–102. https://doi.org/10.1016/j.talanta.2012.01.004.

[134] D.S. Hall, D.J. Lockwood, S. Poirier, C. Bock, B.R. MacDougall, Raman and Infrared Spectroscopy of α and β Phases of Thin Nickel Hydroxide Films Electrochemically Formed on Nickel, J. Phys. Chem. A 116 (2012) 6771–6784. https://doi.org/10.1021/jp303546r.

[135] S. Deabate, F. Fourgeot, F. Henn, X-ray diffraction and micro-Raman

spectroscopy analysis of new nickel hydroxide obtained by electrodialysis, J. Power Sources 87 (2000) 125–136. https://doi.org/10.1016/S0378-7753(99)00437-1.

[136] F. Signori, M.B. Coltelli, S. Bronco, Thermal degradation of poly(lactic acid) (PLA) and poly(butylene adipate-co-terephthalate) (PBAT) and their blends upon melt processing, Polym. Degrad. Stab. 94 (2009) 74–82. https://doi.org/10.1016/j.polymdegradstab.2008.10.004.

[137] Y. Zhuang, W. Song, G. Ning, X. Sun, Z. Sun, G. Xu, B. Zhang, Y. Chen, S. Tao, 3D–printing of materials with anisotropic heat distribution using conductive polylactic acid composites, Mater. Des. 126 (2017) 135–140. https://doi.org/10.1016/j.matdes.2017.04.047.

[138] K. Gnanasekaran, T. Heijmans, S. van Bennekom, H. Woldhuis, S. Wijnia, G. de With, H. Friedrich, 3D printing of CNT- and graphene-based conductive polymer nanocomposites by fused deposition modeling, Appl. Mater. Today 9 (2017) 21–28. https://doi.org/10.1016/j.apmt.2017.04.003.

[139] L.A.S. de A. Prado, M. Kwiatkowska, S.S. Funari, Z. Roslaniec, G. Broza, K. Schulte, Studies on morphology and interphase of poly(butylene terephthalate)/carbon nanotubes nanocomposites, Polym. Eng. Sci. 50 (2010) 1571–1576. https://doi.org/10.1002/pen.21689.

[140] T. Yan, R. Li, Z. Li, Nickel-cobalt layered double hydroxide ultrathin nanoflakes decorated on graphene sheets with a 3D nanonetwork structure as supercapacitive materials, Mater. Res. Bull. 51 (2014) 97–104. https://doi.org/10.1016/j.materresbull.2013.11.044.

[141] J. Zhu, S. Chen, H. Zhou, X. Wang, Fabrication of a low defect density graphene-nickel hydroxide nanosheet hybrid with enhanced electrochemical performance, Nano Res. 5 (2012) 11–19. https://doi.org/10.1007/s12274-011-0179-9.

[142] P.L. dos Santos, R.A. Timm, L.T. Kubota, J.A. Bonacin, Modulation of Electrochemical Properties of Graphene Oxide by Photochemical Reduction Using UV-Light Emitting Diodes, ChemistrySelect 1 (2016) 1168–1175. https://doi.org/10.1002/slct.201600121.

[143] M.P. Browne, M. Pumera, Impurities in graphene/PLA 3D-printing filaments dramatically influence the electrochemical properties of the devices, Chem. Commun. 55 (2019) 8374–8377. https://doi.org/10.1039/C9CC03774H.

[144] A.L. Rinaldi, E. Rodríguez-Castellón, S. Sobral, R. Carballo, Application of a nickel hydroxide gold nanoparticles screen-printed electrode for impedimetric sensing of glucose in artificial saliva, J. Electroanal. Chem. 832 (2019) 209–216. https://doi.org/10.1016/j.jelechem.2018.11.008.

[145] M.L. Chelaghmia, M. Nacef, A.M. Affoune, M. Pontié, T. Derabla, Facile Synthesis of Ni(OH)2 Modified Disposable Pencil Graphite Electrode and its Application for Highly Sensitive Non-enzymatic Glucose Sensor, Electroanalysis 30 (2018) 1117–1124. https://doi.org/10.1002/elan.201800002.

[146] S.H. Lim, J. Wei, J. Lin, Q. Li, J. KuaYou, A glucose biosensor based on electrodeposition of palladium nanoparticles and glucose oxidase onto Nafion-solubilized carbon nanotube electrode, Biosens. Bioelectron. 20 (2005) 2341–2346. https://doi.org/10.1016/j.bios.2004.08.005.

[147] G. Wang, X. He, L. Wang, A. Gu, Y. Huang, B. Fang, B. Geng, X. Zhang, Non-enzymatic electrochemical sensing of glucose, Microchim. Acta 180 (2013) 161–186. https://doi.org/10.1007/s00604-012-0923-1.

[148] A.L. Rinaldi, S. Sobral, R. Carballo, Nickel Hydroxide Nanoparticles on Screen-printed Electrodes as an Impedimetric Non-enzymatic Glucose Sensor, Electroanalysis 29 (2017) 1961–1967. https://doi.org/10.1002/elan.201700187.

[149] G. Başkaya, Y. Yıldız, A. Savk, T.O. Okyay, S. Eriş, H. Sert, F. Şen, Rapid, sensitive, and reusable detection of glucose by highly monodisperse nickel nanoparticles decorated functionalized multi-walled carbon nanotubes, Biosens. Bioelectron. 91 (2017) 728–733. https://doi.org/10.1016/j.bios.2017.01.045.

[150] C.K. Dixit, K. Kadimisetty, J. Rusling, 3D-printed miniaturized fluidic tools in chemistry and biology, TrAC Trends Anal. Chem. 106 (2018) 37–52. https://doi.org/10.1016/j.trac.2018.06.013.

[151] D.J. Cocovi-Solberg, P.J. Worsfold, M. Miró, Opportunities for 3D printed millifluidic platforms incorporating on-line sample handling and separation, TrAC Trends Anal. Chem. 108 (2018) 13–22. https://doi.org/10.1016/j.trac.2018.08.007.

[152] A.F. João, A.L. Squissato, G.M. Fernandes, R.M. Cardoso, A.D. Batista, R.A.A. Muñoz, Iron (III) determination in bioethanol fuel using a smartphone-based device, Microchem. J. 146 (2019) 1134–1139. https://doi.org/10.1016/j.microc.2019.02.053.

[153] M.P. Browne, V. Urbanova, J. Plutnar, F. Novotný, M. Pumera, Inherent impurities in 3D-printed electrodes are responsible for catalysis towards water splitting, J. Mater. Chem. A 8 (2020) 1120–1126. https://doi.org/10.1039/C9TA11949C.

[154] C.E. Banks, A. Crossley, C. Salter, S.J. Wilkins, R.G. Compton, Carbon Nanotubes Contain Metal Impurities Which Are Responsible for the “Electrocatalysis” Seen at Some Nanotube-Modified Electrodes, Angew. Chemie Int. Ed. 45 (2006) 2533–2537. https://doi.org/10.1002/anie.200600033.

[155] J. Kruusma, N. Mould, K. Jurkschat, A. Crossley, C.E. Banks, Single walled carbon nanotubes contain residual iron oxide impurities which can dominate their electrochemical activity, Electrochem. Commun. 9 (2007) 2330–2333. https://doi.org/10.1016/j.elecom.2007.06.024.

[156] M. Pumera, A. Ambrosi, E.L.K. Chng, Impurities in graphenes and carbon nanotubes and their influence on the redox properties, Chem. Sci. 3 (2012) 3347. https://doi.org/10.1039/c2sc21374e.

[157] J.S. Stefano, D.P. Rocha, R.M. Dornellas, L.C.D. Narciso, S.R. Krzyzaniak, P.A. Mello, E. Nossol, E.M. Richter, R.A.A. Munoz, Highly sensitive amperometric detection of drugs and antioxidants on non-functionalized multi-walled carbon

nanotubes: Effect of metallic impurities?, Electrochim. Acta 240 (2017) 80–89. https://doi.org/10.1016/j.electacta.2017.04.050.

[158] J.S. Stefano, A.P. Lima, C.C. Nascentes, S.R. Krzyzaniak, P.A. Mello, J.M. Gonçalves, E.M. Richter, E. Nossol, R.A.A. Munoz, Electrochemical detection of 2,4,6-trinitrotoluene on carbon nanotube modified electrode: Effect of acid functionalization, J. Solid State Electrochem. 24 (2020) 121–129. https://doi.org/10.1007/s10008-019-04465-5.

[159] A.A. Karyakin, E.E. Karyakina, Prussian Blue-based `artificial peroxidase' as a transducer for hydrogen peroxide detection. Application to biosensors, Sensors Actuators B Chem. 57 (1999) 268–273. https://doi.org/10.1016/S0925-4005(99)00154-9.

[160] R.A.A. Munoz, D. Lu, A. Cagan, J. Wang, 'One-step' simplified electrochemical sensing of TATP based on its acid treatment, Analyst 132 (2007) 560–565. https://doi.org/10.1039/B701356F.

[161] T.R.L.C. Paixão, M. Bertotti, Fabrication of disposable voltammetric electronic tongues by using Prussian Blue films electrodeposited onto CD-R gold surfaces and recognition of milk adulteration, Sensors Actuators B Chem. 137 (2009) 266–273. https://doi.org/10.1016/j.snb.2008.10.045.

[162] R.A.B. Silva, R.H.O. Montes, E.M. Richter, R.A.A. Munoz, Rapid and selective determination of hydrogen peroxide residues in milk by batch injection analysis with amperometric detection, Food Chem. 133 (2012) 200–204. https://doi.org/10.1016/j.foodchem.2012.01.003.

[163] M.A. Komkova, E.E. Karyakina, F. Marken, A.A. Karyakin, Hydrogen Peroxide Detection in Wet Air with a Prussian Blue Based Solid Salt Bridged Three Electrode System, Anal. Chem. 85 (2013) 2574–2577. https://doi.org/10.1021/ac303761h.

[164] D.P. Rocha, R.M. Cardoso, T.F. Tormin, W.R. de Araujo, R.A.A. Munoz, E.M. Richter, L. Angnes, Batch-injection Analysis Better than ever: New Materials for Improved Electrochemical Detection and On-site Applications, Electroanalysis 30 (2018) 1386–1399. https://doi.org/10.1002/elan.201800042.

[165] M.S.M. Quintino, L. Angnes, Batch Injection Analysis: An Almost Unexplored Powerful Tool, Electroanalysis 16 (2004) 513–523. https://doi.org/10.1002/elan.200302878.

[166] E. Nossol, A.J.G. Zarbin, A Simple and Innovative Route to Prepare a Novel Carbon Nanotube/Prussian Blue Electrode and its Utilization as a Highly Sensitive H 2 O 2 Amperometric Sensor, Adv. Funct. Mater. 19 (2009) 3980–3986. https://doi.org/10.1002/adfm.200901478.

[167] D.P. Rocha, M.N.T. Silva, R.M. Cardoso, S.V.F. Castro, T.F. Tormin, E.M. Richter, E. Nossol, R.A.A. Munoz, Carbon nanotube/reduced graphene oxide thin-film nanocomposite formed at liquid-liquid interface: Characterization and potential electroanalytical applications, Sensors Actuators B Chem. 269 (2018) 293–303. https://doi.org/10.1016/j.snb.2018.04.147.

[168] S.C. Silva, R.M. Cardoso, E.M. Richter, R.A.A. Munoz, E. Nossol, Reduced graphene oxide/multi-walled carbon nanotubes/prussian blue nanocomposites for amperometric detection of strong oxidants, Mater. Chem. Phys. 250 (2020) 123011. https://doi.org/10.1016/j.matchemphys.2020.123011.

[169] M. Ishizaki, E. Ohshida, H. Tanno, T. Kawamoto, H. Tanaka, K. Hara, H. Kominami, M. Kurihara, H2O2-sensing abilities of mixed-metal (Fe-Ni) Prussian blue analogs in a wide pH range, Inorganica Chim. Acta 502 (2020) 119314. https://doi.org/10.1016/j.ica.2019.119314.

[170] M.A. Komkova, A. Pasquarelli, E.A. Andreev, A.A. Galushin, A.A. Karyakin, Prussian Blue modified boron-doped diamond interfaces for advanced H2O2 electrochemical sensors, Electrochim. Acta 339 (2020) 135924. https://doi.org/10.1016/j.electacta.2020.135924.

[171] A.H. Keihan, R. Ramezani Karimi, S. Sajjadi, Wide dynamic range and ultrasensitive detection of hydrogen peroxide based on beneficial role of gold nanoparticles on the electrochemical properties of prussian blue, J. Electroanal. Chem. 862 (2020) 114001. https://doi.org/10.1016/j.jelechem.2020.114001.

[172] B.M. Pires, F.E. Galdino, J.A. Bonacin, Electrocatalytic reduction of oxygen by metal coordination polymers produced from pentacyanidoferrate(II) complex, Inorganica Chim. Acta 466 (2017) 166–173. https://doi.org/10.1016/j.ica.2017.06.003.

[173] Y. Zhang, X. Sun, L. Zhu, H. Shen, N. Jia, Electrochemical sensing based on graphene oxide/Prussian blue hybrid film modified electrode, Electrochim. Acta 56 (2011) 1239–1245. https://doi.org/10.1016/j.electacta.2010.11.011.

[174] Y. Jiang, X. Zhang, C. Shan, S. Hua, Q. Zhang, X. Bai, L. Dan, L. Niu, Functionalization of graphene with electrodeposited Prussian blue towards amperometric sensing application, Talanta 85 (2011) 76–81. https://doi.org/10.1016/j.talanta.2011.03.028.

[175] L. Cao, Y. Liu, B. Zhang, L. Lu, In situ Controllable Growth of Prussian Blue Nanocubes on Reduced Graphene Oxide: Facile Synthesis and Their Application as Enhanced Nanoelectrocatalyst for H 2 O 2 Reduction, ACS Appl. Mater. Interfaces 2 (2010) 2339–2346. https://doi.org/10.1021/am100372m.

[176] Y.-L. Hu, J.-H. Yuan, W. Chen, K. Wang, X.-H. Xia, Photochemical synthesis of Prussian blue film from an acidic ferricyanide solution and application, Electrochem. Commun. 7 (2005) 1252–1256. https://doi.org/10.1016/j.elecom.2005.09.002.

[177] M.P. O'Halloran, M. Pravda, G.G. Guilbault, Prussian Blue bulk modified screen-printed electrodes for H2O2 detection and for biosensors, Talanta 55 (2001) 605–611. https://doi.org/10.1016/S0039-9140(01)00469-6.

[178] R.A.B. Silva, R.H.O. Montes, E.M. Richter, R.A.A. Munoz, Rapid and selective determination of hydrogen peroxide residues in milk by batch injection analysis with amperometric detection, Food Chem. 133 (2012) 200–204. https://doi.org/10.1016/j.foodchem.2012.01.003.

[179] S.K. Selvamani, K. Rajan, M. Samykano, R.R. Kumar, K. Kadirgama, R. V Mohan, Investigation of tensile properties of PLA–brass composite using FDM, Prog. Addit. Manuf. (2022). https://doi.org/10.1007/s40964-021-00255-6.

[180] T.D. Ngo, A. Kashani, G. Imbalzano, K.T.Q. Nguyen, D. Hui, Additive manufacturing (3D printing): A review of materials, methods, applications and challenges, Compos. Part B Eng. 143 (2018) 172–196. https://doi.org/10.1016/J.COMPOSITESB.2018.02.012.

[181] S.J. Kalita, Rapid prototyping in biomedical engineering: structural intricacies of biological materials, in: Biointegration Med. Implant Mater., Elsevier, 2010: pp. 349–397. https://doi.org/10.1533/9781845699802.3.349.

[182] G.D. O'Neil, S. Ahmed, K. Halloran, J.N. Janusz, A. Rodríguez, I.M. Terrero Rodríguez, Single-step fabrication of electrochemical flow cells utilizing multi-material 3D printing, Electrochem. Commun. 99 (2019) 56–60. https://doi.org/10.1016/j.elecom.2018.12.006.

[183] E. Vaněčková, M. Bouša, F. Vivaldi, M. Gál, J. Rathouský, V. Kolivoška, T. Sebechlebská, UV/VIS spectroelectrochemistry with 3D printed electrodes, J. Electroanal. Chem. 857 (2020) 113760. https://doi.org/10.1016/j.jelechem.2019.113760.

[184] E. Vaněčková, M. Bouša, Š. Nováková Lachmanová, J. Rathouský, M. Gál, T. Sebechlebská, V. Kolivoška, 3D printed polylactic acid/carbon black electrodes with nearly ideal electrochemical behaviour, J. Electroanal. Chem. 857 (2020) 113745. https://doi.org/10.1016/j.jelechem.2019.113745.

[185] E. Vaněčková, M. Bouša, V. Shestivska, J. Kubišta, P. Moreno-García, P. Broekmann, M. Rahaman, M. Zlámal, J. Heyda, M. Bernauer, T. Sebechlebská, V. Kolivoška, Electrochemical Reduction of Carbon Dioxide on 3D Printed Electrodes, ChemElectroChem 8 (2021) 2137–2149. https://doi.org/10.1002/celc.202100261.

[186] J. Giorgini Escobar, E. Vaněčková, Š. Nováková Lachmanová, F. Vivaldi, J. Heyda, J. Kubišta, V. Shestivska, P. Španěl, K. Schwarzová-Pecková, J. Rathouský, T. Sebechlebská, V. Kolivoška, The development of a fully integrated 3D printed electrochemical platform and its application to investigate the chemical reaction between carbon dioxide and hydrazine, Electrochim. Acta 360 (2020) 136984. https://doi.org/10.1016/j.electacta.2020.136984.

[187] Conductive PLA – ProtoPlant, makers of Proto-pasta, (n.d.).

[188] D.P. Rocha, A.L. Squissato, S.M. da Silva, E.M. Richter, R.A.A. Munoz, Improved electrochemical detection of metals in biological samples using 3D-printed electrode: Chemical/electrochemical treatment exposes carbon-black conductive sites, Electrochim. Acta 335 (2020) 135688. https://doi.org/10.1016/j.electacta.2020.135688.

[189] R.S. Shergill, A. Farlow, F. Perez, B.A. Patel, 3D-printed electrochemical pestle and mortar for identification of falsified pharmaceutical tablets, Microchim. Acta 189 (2022) 100. https://doi.org/10.1007/s00604-022-05202-y.

[190] R. Singh Shergill, F. Perez, A. Abdalla, B. Anil Patel, Comparing electrochemical pre-treated 3D printed native and mechanically polished electrode surfaces for analytical sensing, J. Electroanal. Chem. 905 (2022) 115994. https://doi.org/10.1016/j.jelechem.2021.115994.

[191] E.G. Gordeev, A.S. Galushko, V.P. Ananikov, Improvement of quality of 3D printed objects by elimination of microscopic structural defects in fused deposition modeling, PLoS One 13 (2018) e0198370. https://doi.org/10.1371/journal.pone.0198370.

[192] A. Abdalla, H.H. Hamzah, O. Keattch, D. Covill, B.A. Patel, Augmentation of conductive pathways in carbon black/PLA 3D-printed electrodes achieved through varying printing parameters, Electrochim. Acta 354 (2020) 136618. https://doi.org/10.1016/j.electacta.2020.136618.

[193] H.H. Bin Hamzah, O. Keattch, D. Covill, B.A. Patel, The effects of printing orientation on the electrochemical behaviour of 3D printed acrylonitrile butadiene styrene (ABS)/carbon black electrodes, Sci. Rep. 8 (2018) 1–8. https://doi.org/10.1038/s41598-018-27188-5.

[194] B. Zhu, L. Yu, S. Beikzadeh, S. Zhang, P. Zhang, L. Wang, J. Travas-Sejdic, Disposable and portable gold nanoparticles modified - laser-scribed graphene sensing strips for electrochemical, non-enzymatic detection of glucose, Electrochim. Acta 378 (2021) 138132. https://doi.org/10.1016/j.electacta.2021.138132.

[195] Z. Chang, B. Zhu, J. Liu, X. Zhu, M. Xu, J. Travas-Sejdic, Electrochemical aptasensor for 17β-estradiol using disposable laser scribed graphene electrodes, Biosens. Bioelectron. 185 (2021) 113247. https://doi.org/10.1016/j.bios.2021.113247.

[196] D.P. dos Santos, Statistical Analysis of Surface-Enhanced Raman Scattering Enhancement Distributions, J. Phys. Chem. C 124 (2020) 6811–6821. https://doi.org/10.1021/acs.jpcc.9b11574.

[197] C.B.P. Ram Benny Dessau, R: The R Project for Statistical Computing, 170 (2008).

[198] GitHub - rwehrens/alsace: ALS for Automatic Chemical Exploration of mixtures, (n.d.).

[199] F.C. Sánchez, J. Toft, B. van den Bogaert, D.L. Massart, Orthogonal Projection Approach Applied to Peak Purity Assessment, Anal. Chem. 68 (1996) 79–85. https://doi.org/10.1021/ac950496g.

[200] I. Tirado-Garcia, D. Garcia-Gonzalez, S. Garzon-Hernandez, A. Rusinek, G. Robles, J.M. Martinez-Tarifa, A. Arias, Conductive 3D printed PLA composites: On the interplay of mechanical, electrical and thermal behaviours, Compos. Struct. 265 (2021) 113744. https://doi.org/10.1016/j.compstruct.2021.113744.

[201] H. Dou, Y. Cheng, W. Ye, D. Zhang, J. Li, Z. Miao, S. Rudykh, Effect of Process Parameters on Tensile Mechanical Properties of 3D Printing Continuous Carbon

Fiber-Reinforced PLA Composites, Materials (Basel). 13 (2020) 3850. https://doi.org/10.3390/ma13173850.

[202] Y. Tao, F. Kong, Z. Li, J. Zhang, X. Zhao, Q. Yin, D. Xing, P. Li, A review on voids of 3D printed parts by fused filament fabrication, J. Mater. Res. Technol. 15 (2021) 4860–4879. https://doi.org/10.1016/j.jmrt.2021.10.108.

[203] V. Kovan, T. Tezel, E.S. Topal, H.E. Camurlu, Printing parameters effects on surface characteristics of 3D printed PLA materials, Mach. Technol. Mater. 12 (2018) 266–269.

[204] Kovan V, Tezel T, Camurlu HE, Topal ES, Effect of Printing Parameters on Mechanical Properties of 3D Printed Pla/Carbon Fibre Composites, Int. Sci. J. "Materials Sci. Non-Equilibrium Phase Transform. IV (2018) 126–128.

[205] M. Vaezi, C.K. Chua, Effects of layer thickness and binder saturation level parameters on 3D printing process, Int. J. Adv. Manuf. Technol. 53 (2011) 275–284. https://doi.org/10.1007/s00170-010-2821-1.

[206] M. Pawlyta, J.-N. Rouzaud, S. Duber, Raman microspectroscopy characterization of carbon blacks: Spectral analysis and structural information, Carbon N. Y. 84 (2015) 479–490. https://doi.org/10.1016/j.carbon.2014.12.030.

[207] A. Sadezky, H. Muckenhuber, H. Grothe, R. Niessner, U. Pöschl, Raman microspectroscopy of soot and related carbonaceous materials: Spectral analysis and structural information, Carbon N. Y. 43 (2005) 1731–1742. https://doi.org/10.1016/j.carbon.2005.02.018.

CURRICULAR SUMMARY

Complete articles published:

Cardoso, R. M., Kalinke, C., **Rocha, R. G.**, Dos Santos, P. L., Rocha, D. P., Oliveira, P. R., Janegitz, B.; Bonacin, J. A.; Richter, E. M. Munoz, R. A. Additive-manufactured (3D-printed) electrochemical sensors: A critical review. Analytica Chimica Acta, 1118, 73-91,2020. **Cover Feature**

da Silva, F. D., **Rocha, R. G.,** Rocha, D. P., Silva, M. N., Nossol, E., Muñoz, R. A., Dornellas, R. M. In situ electrochemical exfoliation of embedded graphite to superficial graphene sheets for electroanalytical purposes. Electrochimica Acta, 354, 136762, 2020.

Castro, S. V. F.; Lima, A. P.; **Rocha, R. G**.; Cardoso, R. M.; Montes, R. H. O.; Santana, M. H.; Richter. E. M.; Munoz, R. A. A. Simultaneous determination of lead and antimony in gunshot residue using a 3D-printed platform working as sampler and sensor. Analytica Chimica Acta, 1130,126-136, 2020.

Cardoso, R. M., Rocha, D. P., **Rocha, R. G.,** Stefano, J. S., Silva, R. A., Richter, E. M., Munoz, R. A. 3D-printing pen versus desktop 3D-printers: Fabrication of carbon black/polylactic acid electrodes for single-drop detection of 2,4,6-trinitrotoluene. Analytica Chimica Acta, 1132, 10-19, 2020.

Rocha, R. G.; Cardoso, R. M.; Zambiazi, P. J.; Castro, S. V. F.; Ferraz, T. V. B.; Aparecido, G.O.; Bonacin, J. A.; Munoz, R. A. A.; Richter, E. M. Production of 3D-printed disposable electrochemical sensors for glucose detection using a conductive filament modified with nickel microparticles. Analytica Chimica Acta,1132, 1-9,2020.

Rocha, R. G.; Stefano, J. S. Cardoso, R. M.; Zambiazi, P. J.; Bonacin, J. A.; Richter, E. M.; Munoz, R. A. A. Electrochemical synthesis of Prussian blue from iron impurities in 3D-printed graphene electrodes: Amperometric sensing platform for hydrogen peroxide. Talanta, 219, 121289, 2020.

Silva, W. P., **Rocha, R. G.**, Felisbino, J. K., Sousa, R. M., Munoz, R. A., Richter, E. M. Electrochemical Determination of the Steroid Tibolone and Its Metabolites in Saliva Samples. ChemElectroChem, 7(21), 4469-4476, 2020.

Ribeiro, M. M., **Rocha, R. G.**, Munoz, R. A., Richter, E. M. A Batch Injection Analysis System with Square-wave Voltammetric Detection for Fast and Simultaneous Determination of Zinc and Ascorbic Acid. Electroanalysis, 33(1), 90-96, 2021.

Rocha, R. G., Silva, I. C., Arantes, L. C., Stefano, J. S., Lima, C. D., Melo, L. M., Richter, E. M. Simple and rapid electrochemical detection of 1-benzylpiperazine on carbon screen-printed electrode. Microchemical Journal, 167, 106282, 2021

João, A. F., **Rocha, R. G.**, Matias, T. A., Richter, E. M., Petruci, J. F. S., Muñoz, R. A. A. 3D-printing in forensic electrochemistry: Atropine determination in beverages using an additively manufactured graphene-polylactic acid electrode. Microchemical Journal, 167, 106324, 2021.

Castro, S. V., **Rocha, R. G.**, João, A. F., Richter, E. M., Munoz, R. A. A. Promising Applications of Additive-Manufactured (3Dprinted) Electrochemical Sensors for Forensic Chemistry. Brazilian Journal of Analytical Chemistry, 9(34), 79-105, 2021.

Rocha, D. P., **Rocha, R. G.**, Castro, S. V., Trindade, M. A., Munoz, R. A., Richter, E. M., Angnes, L. Posttreatment of 3D-printed surfaces for electrochemical applications: A critical review on proposed protocols. Electrochemical Science Advances, e2100136, 2021.

Silva, W. P., **Rocha, R. G.**, Arantes, L. C., Lima, C. D., Melo, L. M., Munoz, R. A. A., Richter, E. M. Development of a simple and rapid screening method for the detection of 1-(3-chlorophenyl) piperazine in forensic samples. Talanta, 233, 122597, 2021.

Pereira, J. F., **Rocha, R. G.**, Castro, S. V., Joao, A. F., Borges, P. H., Rocha, D. P.,Munoz, R. A. Reactive oxygen plasma treatment of 3D-printed carbon electrodes towards high-performance electrochemical sensors. Sensors and Actuators B: Chemical, 347, 130651, 2021.

Rocha, R. G., Ribeiro, J. S., Santana, M. H., Richter, E. M., Muñoz, R. A. A. 3D-printing for forensic chemistry: voltammetric determination of cocaine on additively manufactured graphene–polylactic acid electrodes. Analytical Methods, 13(15), 1788-1794, 2021. **Cover Feature**

dos Santos Novais, A., Arantes, L. C., Almeida, E. S., **Rocha, R. G.**, Lima, C. D., de Almeida Melo, L. M., da Silva, R. A. B. Fast on-site screening of 3, 4-

methylenedioxyethylamphetamine (MDEA) in forensic samples using carbon screen-printed electrode and square wave voltammetry. Electrochimica Acta, 403, 139599, 2022.

Stefano, J. S., e Silva, L. R. G., **Rocha, R. G.**, Brazaca, L. C., Richter, E. M., Muñoz, R. A. A., Janegitz, B. C. New conductive filament ready-to-use for 3D-printing electrochemical (bio) sensors: towards the detection of SARS-CoV-2. Analytica Chimica Acta, 1191, 339372, 2022.

Stefano, J. S., Kalinke, C., **Rocha, R. G.,** Rocha, D. P., da Silva, V. A. O. P., Bonacin, J. A., Muñoz, R. A. A. Electrochemical (Bio) Sensors Enabled by Fused Deposition Modeling-Based 3D Printing: A Guide to Selecting Designs, Printing Parameters, and Post-Treatment Protocols. 2022. **Cover Feature**

Matias, T. A., de Faria, L. V., **Rocha, R. G.**, Silva, M. N., Nossol, E., Richter, E. M., Muñoz, R. A. Prussian blue-modified laser induced graphene platforms for detection of hydrogen peroxide. Microchimica Acta, 189(5), 1-9, 2022.

Di-Oliveira, M., **Rocha, R. G.**, de Faria, L. V., Richter, E. M., & Munoz, R. A. Carbon-Black Integrated Polylactic Acid Electrochemical Sensor for Chloramphenicol Determination in Milk and Water Samples. Journal of The Electrochemical Society, 169(4), 047517, 2022.

Matias, T. A., **Rocha, R. G.**, Faria, L. V., Richter, E. M., Munoz, R. A. Infrared Laser-Induced Graphene Sensor for Tyrosine Detection. ChemElectroChem, 9(14), e202200339, 2022. **Cover Feature**

Carvalho, M. S., **Rocha, R. G.**, de Faria, L. V., Richter, E. M., Dantas, L. M., da Silva, I. S. Muñoz, R. A. Additively manufactured electrodes for the electrochemical detection of hydroxychloroquine. Talanta, 250, 123727, 2022.

Costa, W. R., **Rocha, R. G.**, de Faria, L. V., Matias, T. A., Ramos, D. L., Dias, A. G., Muñoz, R. A. Affordable equipment to fabricate laser-induced graphene electrodes for portable electrochemical sensing. Microchimica Acta, 189(5), 1-9, 2022.

de Faria, L. V., **Rocha, R. G.**, Arantes, L. C., Ramos, D. L., Lima, C. D., Richter, E. M., Muñoz, R. A. Cyclic square-wave voltammetric discrimination of the amphetamine-type stimulants MDA and MDMA in real-world forensic samples by 3Dprinted carbon electrodes. Electrochimica Acta, 141002, 2022.

João, A. F., de Faria, L. V., Ramos, D. L., **Rocha, R. G.**, Richter, E. M., Muñoz, R. A. (2022). 3D-printed carbon black/polylactic acid electrochemical sensor combined with batch injection analysis: A cost-effective and portable tool for naproxen sensing. Microchemical Journal, 180, 107565, 2022.

Rocha, R. G.; de Faria, L. V.; Ramos, D. L. O.; Germscheidt, R. L.; dos Santos, D. P.; Bonacin, J. A.; Munoz, R. A. A.; Richter, E. M. Printing parameters affect the electrochemical performance of 3D-printed carbon electrodes obtained by fused deposition modeling. Journal of Electroanalytical Chemistry,925,116910,2022.

Siqueira, G. P. de Faria, L. V.; **Rocha, R. G.**, Matias, T. A.; Richter, E. M., Muñoz, R. A. A., da Silva, I. S., Dantas, L. M. F. Nanoporous gold microelectrode arrays using

microchips: A highly sensitive and cost-effective platform for electroanalytical applications. 925, 116880, 2022.

Camargo, J. R., Fernandes-Junior, W.S., Azzi, D. C., **Rocha, R. G.**, Faria, L. V., Richter, E. M., Munoz, R. A. A., Janegitz, B. C. Development of New Simple Compositions of Silver Inks for the Preparation of Pseudo-Reference Electrodes. Biosensors. 12(9), 761, 2022

Silva, M. N. T. **Rocha, R. G.**, Richter, E. M.; Munoz, R. A. A., Nossol, E. Nickel Oxy-Hydroxy/Multi-Wall Carbon Nanotubes Film Coupled with a 3D-Printed Device as a Nonenzymatic Glucose Sensor. Biosensors. 13(6), 646, 2023.

Rocha, R. G., de Faria, L. V., Silva, V. F., Muñoz, R. A. A., Richter, E. M., Carbon Black Integrated Polylactic Acid Electrodes Obtained by Fused Deposition Modeling: A Powerful Tool for Sensing of Sulfanilamide Residues in Honey Samples. J. Agric. Food. Chem.71(6), 3060-3067, 2023

Di-Oliveira, M., Araújo, D. A. G., Ramos, D. L. O., de Faria, L. V., **Rocha, R. G.**, Richter, E. M., Paixão, T. R. L. C., Munoz, R. A. A., Sequential cyclic-square-wave voltammetric determination of sulfanilamide and ciprofloxacin in environment water samples using a 3D-printed electrochemical device. Electrochimica Acta, 481, 143945, 2024.

Patents application

Castro, S. V. F., Montes, R. H. O., Richter, E. M., Pereira, J. F. S., Cardoso, R. M., **Rocha, R. G.**, Muñoz, Rodrigo A. A. Sensor eletroquímico para análise de resíduos de disparo de arma de fogo. 2021, Brasil. Patente: Privilégio de Inovação. Número do registro: BR10202101437, Instituição de registro: INPI - Instituto Nacional da Propriedade Industrial. 21/07/2021.

Stefano, J. S., Guterres, L. R., Janegitz, B. C., **Rocha, R. G.**, Richter, E. M., Muñoz, R. A. A. Compósitos, filamentos condutores para impressão 3D, aplicação dos filamentos na eletroanalítica e processo de produção. 2021, Brasil. Patente: Privilégio de inovação. Número do registro: BR10202101552. Instituição de registro: INPI - Instituto Nacional da Propriedade Industrial. 06/08/2021